



UNIVERSITY OF PÉCS
POLLACK MIHÁLY FACULTY OF ENGINEERING AND INFORMATICS
BREUER MARCELL DOCTORAL SCHOOL

INVESTIGATION OF STRUCTURES BY SIMULATION TECHNIQUES

Design, technology, reconstruction

PhD DISSERTATION

Candidate:
Attila FÜLÖP MSc.

Supervisor:
Miklós IVÁNYI, Dr., DSc.
Professor Emeritus

2011

Contents

Contents	3
Foreword.....	5
1. Monte-Carlo simulation method in the design of structures	7
1.1. Summary of the Monte-Carlo method	7
1.1.1. Introduction.....	7
1.1.2. Monte-Carlo method in simulation.....	8
1.2. Design of structural elements applying Monte-Carlo method.....	9
1.2.1. Safety of a truss-girder bar subjected to tension.....	9
1.2.2. Safety of a column in a frame.....	12
1.2.3. Safety of a rectangular hollow section exposed to multi-component loads according to Eurocode 3.....	14
1.2.4. Shear resistance of a bolted beam to beam connection	18
1.2.5. Determination of the safety of the tee joint of a welded I-section according to Eurocode.....	21
1.3. Examination of the lateral buckling of welded I-section under bending	25
1.4. Parametrical examination a column in a simple frame	28
1.5. Conclusions.....	31
References I.....	32
2. Simulations of producing and design of structures	33
2.1. Simulation of the formation procedure of the bars	33
2.1.1. The formation procedure of the bars.....	33
2.1.2. Numerical modelling of the formation process	35
2.1.3. Results of the numerical analysis.....	40
2.1.4. Verifying the calculated result.....	43
2.2. Results of the numerical analysis of compressed bars.....	47
2.3. Results of the numerical analysis of space-truss segment	56
2.4. The full-scale tests on the space-truss specimen.....	61
2.4.1. Load case 1: Eccentrically loaded roof in linear elastic range	62
2.4.2. Load case 2: Concentrically loaded roof in "elastic" range.....	64
2.4.3. Load case 3: Failure load of the concentrically loaded roof.....	66
2.5. Individual experiments on the bars	70

2.6. Conclusions	72
References II.	74
3. Refurbishment of ancient masonry structures	76
3.1. Introduction	76
3.2. Numerical simulation of the lateral confinement.....	79
3.2.1. The collapse of the Civic Tower of Pavia.....	79
3.2.2. Experimental tests.....	81
3.2.3. Experimental results	84
3.2.4. Computer modelling of the experimental test series	87
3.3. Parametrical analysis series applying lateral confinement.....	99
3.3.1. Introduction.....	99
3.3.2. Parametrical test set-up.....	99
3.3.3. Computed results	102
3.3.4. Some conclusions about the reinforcing by lateral confinement.....	108
References III.	109

Foreword

This PhD dissertation represents my extensive work, what I performed in the last years. During this time I worked on several fields of structural and architectural engineering in the viewpoint of design, technology and reconstruction of structures. This work required several help and support from different places.

The first chapter was supported by TEREKO "Innovation in Teaching Reliability Concepts using Simulation" Leonardo da Vinci programme, European Commission, Project No. CZ/98/1/82502/PI/I.1.1.a/FPI.

The second chapter was supported by OTKA research project (No.: T 029640), "Nagyméretű rúdszerkezetek állapotváltozásának vizsgálata a fizikai és geometriai nemlinearitás figyelembe vételével – Research of the deformation behaviour of great-scale bar structures considering the physical and geometrical non-linearity", 1999-2002.

The third chapter was supported by TEMPUS JEP 9524 "Using Steel in Refurbishment as an Environmentally Friendly Activity", 1996-1998.

I express my gratitude to all, who offered me the possibility to accomplish this work.

Above all I would like to thank to my supervisor Prof. Miklós IVÁNYI Dr., DSc. – University of Pécs, Pollack Mihály Faculty of Engineering and Informatics, Pécs, Hungary – for all of his entire support during my work. Furthermore I express my gratitude to Dr. Anikó CSÉBFALVI, PhD and the Pollack Mihály Faculty of Engineering and Informatics.

I express my gratitude to senior research assistant Miklós KÁLLÓ and senior research assistant László KALTENBACH for their important and useful help at the experiments on the TOP–SYSTEM space truss and the work of the staff members of the Structural Laboratory of the Department of Structural Engineering, Budapest University of Technology and Economics, Hungary is highly appreciated. Furthermore I express my gratitude to Prof. László DUNAI, Dr. DSc., head of the Department of Structural Engineering, Budapest University of Technology and Economics for his help.

I express my gratitude to László LEBŐ DUNAFERR Acélszerkezeti Kft. – Steel Structures Ltd., Dunaújváros, Hungary, for the useful help for the modelling of the special formation method at producing the bars of the TOP–SYSTEM space truss.

I express my gratitude to Zsolt MOSONYI, FEA Engineer, Gumitech Kft. WOCO group, Budapest, Hungary for his very useful help and the possibility of working on ABAQUS finite element program; to Zsolt H. TÓTH, FEA Business Unit Manager,

Varinex Informatics, Budapest, Hungary, as the Hungarian agency of MSC. Software Corp. for ensuring the licence of the MSC Patran program.

I express my gratitude also to László SZOBONYA PhD, MTA SZTAKI, Hungarian Academy of Sciences, Budapest, Hungary for the very useful help with the 3D laser scanner during the numerical model verification.

I express my gratitude to Dr. Jenő BALOGH, PhD, Civil Engineering Technology Faculty, Metropolitan State College of Denver, Colorado, USA, for the useful help during the numerical modelling by Axis FEM program, and also to Gábor BOKOR, InterCAD Kft., Budapest, Hungary, for the licence of the AxisVM10 special version for PhD doctoral calculations.

I wish to acknowledge my appreciation for the support to my work at the University of Naples, during the examination and numerical simulation of the reinforcing method applying lateral confinement to Prof. Federico M. MAZZOLANI, DSc., Prof. Alberto MANDARA, PhD, Prof. Gianfranco De MATTEIS, PhD and also to the staff of the Department of Structural Analysis and Design, University of Naples, Naples, Italy.

Finally I express my gratitude to my wife and to my family for their unconditional support during these years.

Pécs, 2011 August

PhD Candidate:
Attila FÜLÖP MSc.

1. Monte-Carlo simulation method in the design of structures

1.1. Summary of the Monte-Carlo method

1.1.1. Introduction

Nowadays the computer simulation techniques are going to be playing important role in everyday practice. From the viewpoint of design practice, the current procedures for reliability assessment of structural components and systems contained in specifications do not fully utilize the potential of available computer technology. Monte Carlo Simulation (MCS) may play a significant role in the evaluation of data available from different sources including experiments, the experience and estimates furnished by the designer, the user, and others involved. Simulation, using MCS, is a very powerful and convenient tool for the analysis of load effect combinations, for determining resistance, for evaluating the probability of failure of structures and structural components, and for assessing serviceability criteria [5], [6], [7].

The MCS method directly determines the probability of failure corresponding to any combination of variable loads effects S , and the random variable resistance R . A personal computer creates tens of thousands of dots representing the possible interactions of resistance R and load effect S . To obtain the probability of failure, the number of dots in the Failure region, which appears to the right of the Failure Boundary line, is divided by the total number of dots (Figure 1.1). These results are then compared to the acceptable level of probability of failure.

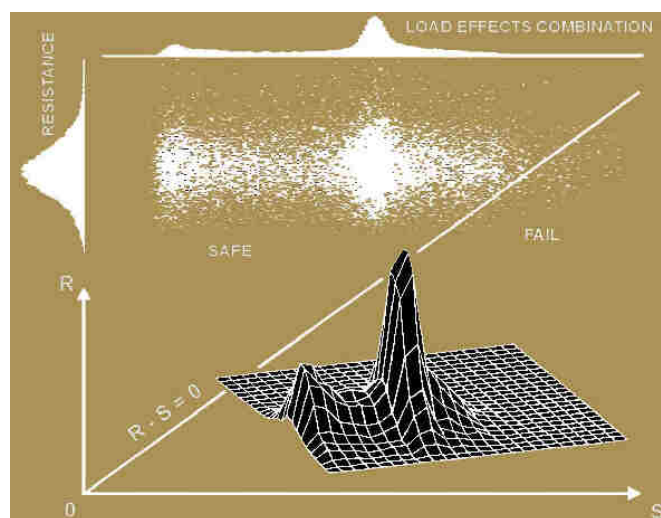


Figure 1.1 Determination of reliability using the simulation technique [5]

1.1.2. Monte-Carlo method in simulation

Professor Pavel Marek was the coordinator of a Leonardo da Vinci Project, called Tereco – Teaching Reliability Concepts using Simulation Technique. In the frame of this project, where the candidate and the supervisor were partners, a textbook is developed, which applies a reliability assessment method called “SBRA” (“Simulation-Based Reliability Assessment”) [7].

Monte Carlo simulation is used that book for analyzing various problems and situations common in structural design. It is helpful to visualize a Monte Carlo analysis as a series of experiments, which are performed by a computer rather than in a laboratory. Each experiment is performed many times and the results are summarized in terms of their statistics. The fundamental step in this analysis is the simulation of random variations in the experiments through the generation of a set of random numbers [5].

The following quotations may serve to define Monte Carlo simulation.

Kleinen J.P.C.[3]: “Monte Carlo simulation method implies experimentation. Instead of experimenting with the real world object we experiment by means of the model of that object. The object of a simulation study is a system. The experimentation involves the sampling of values of stochastic variables uses random numbers. Because random numbers are used, this type of simulation is denoted as Monte Carlo Simulation.”

Design based on the simulation-based reliability assessment concept completely different from Allowable Stress Design and Partial Factor Design concepts. A simple introduction to the potential of the Monte Carlo method should encourage the user of existing specifications to pay attention to a concept that uses the power of today’s available computer technology. If designers find this concept efficient, easy to understand, time-saving, applicable in everyday work, and friendly for reliability assessment, they will be ready to consider tools like Latin Hypercube and other advanced simulation-based methods for application in special cases.

Only a little more than twenty years ago, the textbooks dealing with Monte Carlo simulation contained “generators of random numbers” in the form of tables of random numbers and some of the discussed examples were based on as few as ten to twenty simulation steps. Due to the computer revolution, today tens of thousands of random numbers can be generated and thousands of simulation steps can be performed in seconds, using a desktop PC.

Due to the random nature of the generator and of the Monte Carlo method, some small variations of the results are expected to be observed. These inaccuracies, however, may be considered to be negligible in the reliability assessment of structures when compared to many common and frequent inaccuracies and errors resulting from incomplete load estimates and evaluation of load combinations, from selection and simplification of the transformation models, from the quality of construction, and from actual service conditions.

Totally five computer programs are included with the text of TEREKO book to help the reader in exploring the power of the proposed simulation-based reliability assessment procedure. All five programs are based on the simple random sampling Monte Carlo simulation. In the case of this computer programs, the Borland Pascal 7.0 built-in random number generator was used. In the following chapter two of the five programs were used: M-StarTM and the AntHillTM.

The program M-StarTM allows solution of equations (algebraic, logarithmic, exponential and trigonometric) containing up to 30 random variables expressed by bounded histograms. The proposed method and the computer program are applicable for problems related to the determination of resistance, combination of load effects, probability of failure, accumulation of damage and assessment of serviceability. The proposed procedure is also applicable to selected second order analysis problem such as column buckling.

Problems involving two- and multi-component variables can be analyzed using the AntHillTM program. Using the "anthill" method, various reliability assessment problems are studied. Selected special problems such as principal stresses resulting from multi-component structural response to several loadings from different sources can be solved.

1.2. Design of structural elements applying Monte-Carlo method

In the following I present some example for typical engineering problems applying the Monte-Carlo method and the above mentioned technique

1.2.1. Safety of a truss-girder bar subjected to tension [7][12]

Assignment:

Assess the safety of the bar 5-6 of the simply supported truss-girder shown in Figure 1.2. The loading consists of a combination of dead loads (DL), long-lasting loads

(LL) and short-lasting loads (SL). All loads are mutually statistically independent. The bar is safe if the probability of failure P_f is lower than the assumed target probability $P_d = 0.00007$ ($P_f < P_d$)

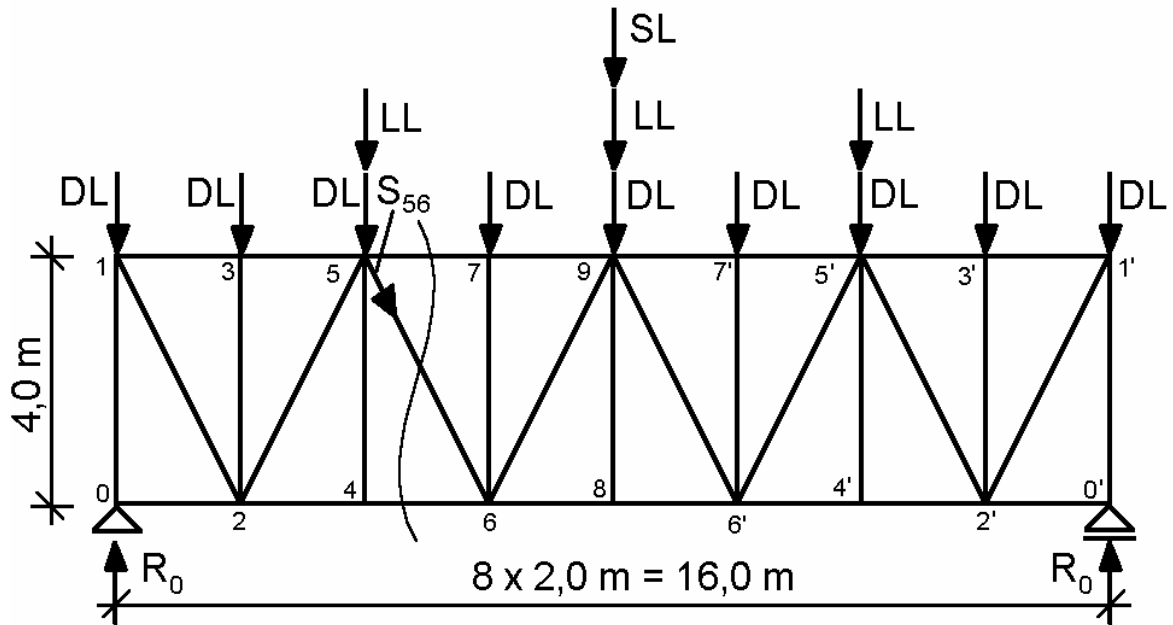


Figure 1.2 Geometry of the truss-girder

Input and variables:

The bar being investigated is a 50×50×4 mm square hollow section. The nominal value of the cross-section area is $A_{nom} = 5.67 \text{ cm}^2$. The loads considered are shown in Table 1.1.

Table 1.1 Loadings and variations

Load	Extreme Value	Variable	Histogram
Dead load	DL = 60 kN	DLvar	DEAD2.his
Short-lasting	SL = 60 kN	SLvar	SHORT1.his
Long-lasting	LL = 40 kN	LLvar	LONG1.his

Loading variation is described by histograms DLvar, LLvar and SLvar as indicated. The variation of the cross sectional area of bar is expressed by Avar, (histogram Area-S.his). The variable yield stress of the bar f_y is defined by the product of the basic value $f_{y,nom} = 235 \text{ N/mm}^2$ and a factor represented by the histogram Fy235A.his.

Combination of the load effects and determination of the resistance of the bar

The tension in bar 5-6 (S_{56}) can be calculated from the vertical force equilibrium. The support reaction can be determined as:

$$R_0 = (9 \times DL + SL + 3 \times LL) / 2 \quad /1.1/$$

thus the vertical force equilibrium on the left hand side of the truss-girder is:

$$\Sigma F_{\text{vertical}} = R_0 - 3 \times DL - LL - S_{56} \times 4 / 20^{0.5} = 0 \quad /1.2/$$

$$S_{56} = 20^{0.5} / 4 \times (1.5 \times 60 \times DL_{\text{var}} + 0.5 \times 60 \times SL_{\text{var}} + 0.5 \times 40 \times LL_{\text{var}}) \text{ [kN]} \quad /1.3/$$

The tension resistance of the square hollow section is:

$$R_{56} = A \times f_y = 5.67 \times A_{\text{var}} \times 23.5 \times f_{y\text{var}} \text{ [kN]} \quad /1.4/$$

Thus, the safety of the bar can be written as follows:

$$SF = R_{56} - S_{56} \quad /1.5/$$

Failure occurs if $SF < 0$.

Application of the simulation technique:

The safety function (Eqn. 1.5) is evaluated using the AntHill. The Anthill output is shown in Figure 1.3.

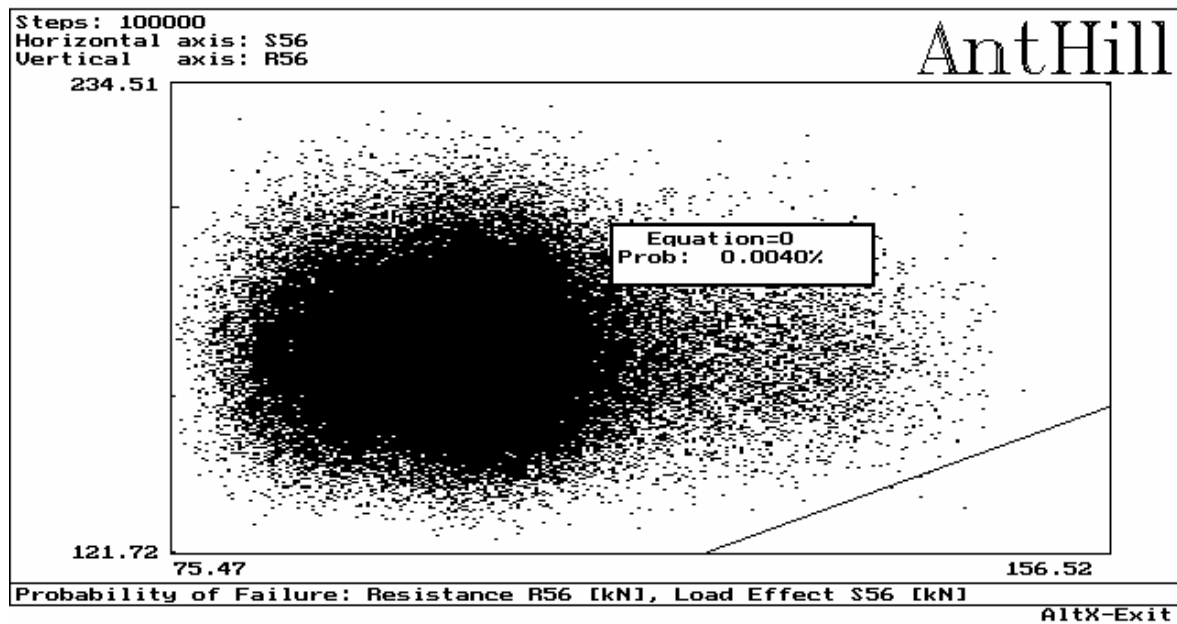


Figure 1.3 The safety of failure of the tensioned bar of the truss-girder
(AntHill™ program output).

Results and conclusions:

The square hollow bar subject to tension is safe, because the probability of failure $P_f = 0.00004$ is less than the assumed target probability $P_f = 0.00004 < P_d = 0.00007$.

1.2.2. Safety of a column in a frame [7] [12]

Assignment:

Assess the safety against flexure of the column in the frame shown in Figure 1.4. In this example an elastic 1st order analysis is performed, and stresses due to axial force are not considered. On the investigated frame, the forces are a combination of dead load, long-lasting load and short-lasting load. All loads are mutually statistically independent. The column is safe if the probability of failure P_f is lower than the assumed target probability $P_d = 0.00007$ ($P_f < P_d$)

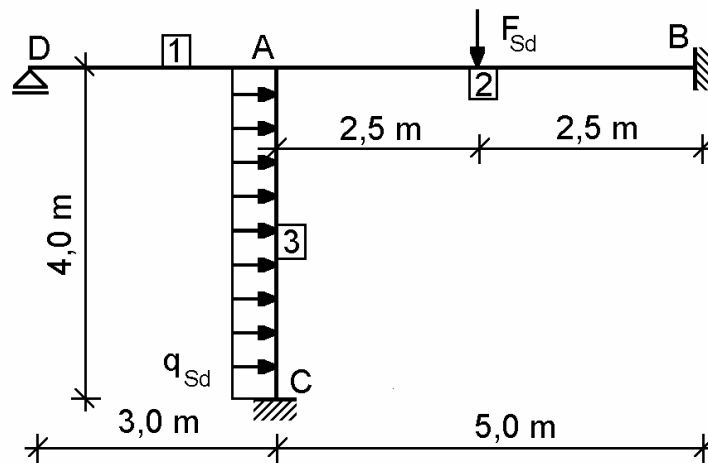


Figure. 1.4 The geometry of the frame

Input and variables:

The beams are HEB 100 sections with moment of inertia $I_{y,nom} = 449.5 \text{ cm}^4$ and the column is an HEB 120 section with a moment of inertia of $I_{y,nom} = 864.4 \text{ cm}^4$. The elastic modulus of the column cross-section is $W_{y,nom} = 144.1 \text{ cm}^3$. The external loads and geometrical data are given in Table 1.2 and 1.3.

Table 1.2 Loadings and variations

Distributed loads (q_{Sd})			
Load	Extreme Value	Variable	Histogram
Dead load 1	DL1 = 11 kN/m	DLvar1	DEAD2.his
Short-lasting 1	SL1 = 9 kN/m	SLvar1	SHORT1.his
Long-lasting 1	LL1 = 5.5 kN/m	LLvar1	LONG1.his
Concentrated loads (FSd)			
Load	Extreme Value	Variable	Histogram
Dead load 2	DL2 = 3.5 kN	DLvar2	DEAD2.his
Short-lasting 2	SL2 = 2.2 kN	SLvar2	SHORT1.his
Long-lasting 2	LL2 = 1.7 kN	LLvar2	LONG1.his

Table 1.3 Geometrical data and variation

Geometrical data	Nominal Value	Variable	Histogram
$I_{y,1}$	449.5 cm ⁴	lvar1	N1-05.his
$I_{y,2}$	449.5 cm ⁴	lvar2	N1-05.his
$I_{y,3}$	864.4 cm ⁴	lvar3	N1-05.his
$W_{y,3}$	144.1 cm ³	Wvar3	N1-05.his
l_1	3 m	lvar	N1-01.his
l_2	5 m	lvar	N1-01.his
l_3	4 m	lvar	N1-01.his

Load variation is described by the histograms of DLvar, LLvar and SLvar. The variations of the geometric properties of the sections are expressed by the variation of the moments of inertia, the sectional modulus of column, and the member lengths. The variations of member lengths are described by the same histogram. The variable yield stress of the column f_y is defined by the product of the basic value $f_{y,nom} = 235 \text{ N/mm}^2$ and a factor represented by the histogram Fy235A.his.

Determination of the load effect and the resistance of the column

The maximum bending moment in the column will occur at support C as shown on Figure 1.4. The bending moment at C can be calculated using the displacement method, since only one displacement the rotation θ_A of connection A is unknown. The rotation of connection A is calculated according to Iványi [2]. The moment equilibrium equation of connection A will be used to determine the rotation:

$$\Sigma M_A = (3 \times k_1 + 4 \times k_2 + 4 \times k_3) \times \theta_A + q_{sd} \times l_3^2 / 12 - F_{sd} \times l_2 / 8 = 0 \quad /1.6/$$

where

$k_1 = EI_1 / l_1$, $k_2 = EI_2 / l_2$ and $k_3 = EI_3 / l_3$, $l_1 = 3.0 \text{ m}$, $l_2 = 5.0 \text{ m}$ and $l_3 = 4.0 \text{ m}$ and E is the Young's modulus $E = 210000 \text{ N/mm}^2$.

The external loads are assumed as:

$$q_{sd} = 11 \times DLvar + 9 \times SLvar + 5.5 \times LLvar \quad [\text{kN/m}] \quad /1.7/$$

$$F_{sd} = 3.5 \times DLvar + 2.2 \times SLvar + 1.7 \times LLvar \quad [\text{kN}] \quad /1.8/$$

Thus the rotation of connection A is:

$$\theta_A = (F_{sd} \times l_2 / 8 - q_{sd} \times l_3^2 / 12) / (3 \times k_1 + 4 \times k_2 + 4 \times k_3) \quad [\text{radian}] \quad /1.9/$$

The maximum bending of column $M_{C.Sd}$ is then calculated as:

$$M_{C.Sd} = q_{Sd} \times l_3^2 / 12 + 2 \times k_3 \times \theta_A \quad [\text{kNm}] \quad /1.10/$$

The moment resistance of the column cross-section can be written as:

$$M_{Rd} = W_{el} \times f_y = 144.1 \times W_{var} \times 23.5 \times f_{yvar} / 100 \quad [\text{kNm}] \quad /1.11/$$

The safety of the column to resist flexure can be written as follows:

$$SF = M_{Rd} - M_{C.Sd}. \quad /1.12/$$

Failure occurs if $SF < 0$.

Application of the simulation technique:

The safety of HEB 120 column against flexural failure, expressed by equation /1.12/, is analysed by using the M-Star program. The M-Star output is shown in Figure 1.5.

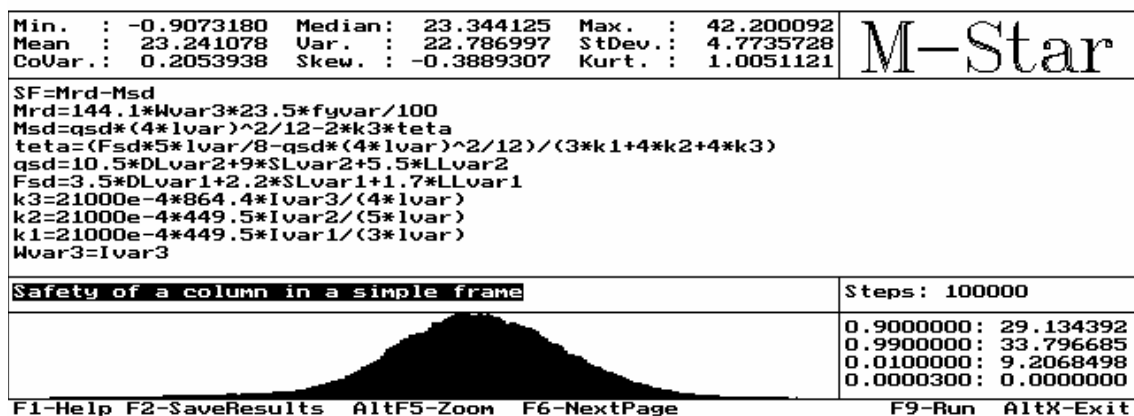


Figure 1.5 The safety of column to resist flexure (M-Star™ program output).

Results and Conclusions:

The HEB 120 column is safe against flexure, because the probability of failure $P_f = 0.00003$ is less than the assumed target probability $P_f = 0.00003 < P_d = 0.00007$.

1.2.3. Safety of a rectangular hollow section exposed to multi-component loads according to Eurocode 3 [7] [12]

Assignment:

The following example examines a rectangular hollow section subjected to a multi-component load. The rectangular hollow section is subjected to a combination of dead

load, long-lasting load and short-lasting load. All loads are mutually statistically independent. The resultants of these loads are the internal forces: simultaneous axial load and biaxial bending moment. The resistances will be calculated according to Eurocode 3 design rules [10].

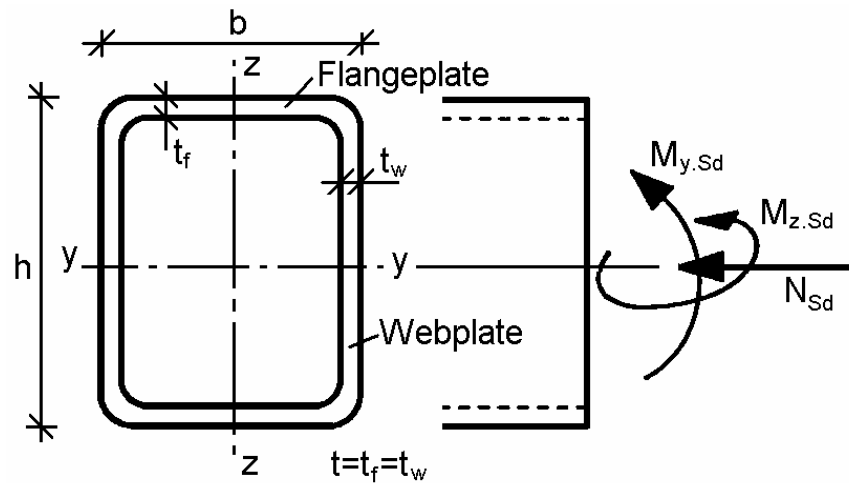


Figure 1.6 The loaded rectangular hollow section

Input and variables:

The cross section of rectangular hollow 220 × 140 × 5 mm section is shown in Figure 1.6. The cross sectional properties and the external loads are given in Table 1.4 and Table 1.5.

Table 1.4 Geometric data and variation

Section Property	Nominal Value	Variable	Histogram
A	34.1 cm ²	Avar	Area-S.his
W _{el.y}	208 cm ³	Wyvar	N105.his
W _{el.z}	164 cm ³	Wzvar	N105.his

Table 1.5 Loadings and variations

Normal Force (N _{Sd})				
Load	Nominal value	Extreme Value	Variable	Histogram
Dead load1	DL1 = 220 kN	1.35 × 220 = 297 kN	DLvar1	DEAD2.his
Long-lasting1	LL1 = 45 kN	1.5 × 45 = 67.5 kN	LLvar1	LONG1.his
Short-lasting1	SL1 = 5 kN	1.5 × 5 = 7.5 kN	SLvar1	SHORT1.his

Bending Moment about y-axis ($M_{y.Sd}$)				
Load	Nominal value	Extreme Value	Variable	Histogram
Dead load2	DL2 = 8 kNm	$1.35 \times 8 = 10.8$ kNm	DLvar2	DEAD2.his
Long-lasting2	LL2 = 3 kNm	$1.5 \times 3 = 4.5$ kNm	LLvar2	LONG1.his
Short-lasting2	SL2 = 2 kNm	$1.5 \times 2 = 3$ kNm	SLvar2	SHORT1.his
Bending Moment about z-axis ($M_{z.Sd}$)				
Load	Nominal value	Extreme Value	Variable	Histogram
Dead load3	DL3 = 3 kNm	$1.35 \times 3 = 4.05$ kNm	DLvar3	DEAD2.his
Long-lasting3	LL3 = 1.5 kNm	$1.5 \times 1.5 = 2.25$ kNm	LLvar3	LONG1.his
Short-lasting3	SL3 = 0.5 kNm	$1.5 \times 0.5 = 0.75$ kNm	SLvar3	SHORT1.his

The load variation is described by histograms DLvar, LLvar and SLvar. The variations of the geometric properties of the rectangular hollow section are expressed by the variation of the gross area and the elastic section moduli. The variable yield stress f_y is defined by the product of the basic value $f_{y,nom} = 235 \text{ N/mm}^2$ and a factor represented by the histogram Fy235A.his. The distribution of normal stresses due to the interaction of normal force and biaxial bending is illustrated in Figure 1.7.

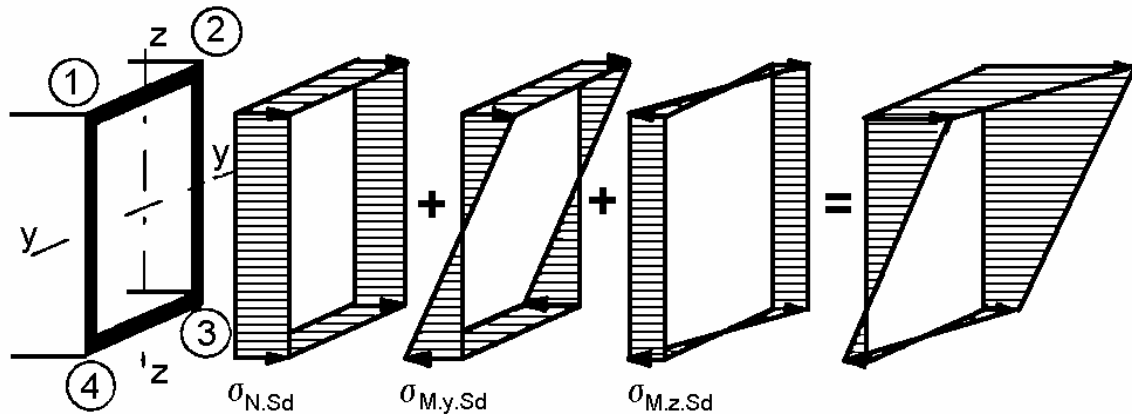


Figure 1.7 Distribution of normal stress

Interaction of axial load and biaxial bending moment according to Eurocode 3

The interaction formula of axial load and biaxial bending moment in the case of class 3 cross-sections according to Eurocode 3 [10] is:

$$\frac{N_{Sd}}{A f_y / \gamma_{M0}} + \frac{M_{y.Sd}}{W_{el.y} f_y / \gamma_{M0}} + \frac{M_{z.Sd}}{W_{el.z} f_y / \gamma_{M0}} \leq 1 \quad /1.13/$$

$$N_{Sd} = 1.35 \times 220 + 1.5 \times 45 + 0.6 \times 1.5 \times 5 = 369 \text{ kN} \quad /1.14/$$

$$M_{y.Sd} = 1.35 \times 8 + 1.5 \times 3 + 0.6 \times 1.5 \times 2 = 17.1 \text{ kNm} \quad /1.15/$$

$$M_{z.Sd} = 1.35 \times 3 + 1.5 \times 1.5 + 0.6 \times 1.5 \times 0.5 = 6.75 \text{ kNm} \quad /1.16/$$

The safety of the section can be defined as:

$$SF_{EC} = 1 - \left(\frac{N_{Sd}}{A f_y / \gamma_{M0}} + \frac{M_{y.Sd}}{W_{el.y} f_y / \gamma_{M0}} + \frac{M_{z.Sd}}{W_{el.z} f_y / \gamma_{M0}} \right) \quad /1.17/$$

$$SF_{EC} = 1 - \left(\frac{369}{34.1 \cdot 23.5 / 1.1} + \frac{1710}{208 \cdot 23.5 / 1.1} + \frac{675}{164 \cdot 23.5 / 1.1} \right) = -0.084 < 0, \text{ therefore the}$$

rectangular hollow section is unsafe.

Application of the simulation technique:

The safety of the section can be defined:

$$SF = 1 - \left(\frac{N_{Sd}}{A f_y / \gamma_{M0}} + \frac{M_{y.Sd}}{W_{el.y} f_y / \gamma_{M0}} + \frac{M_{z.Sd}}{W_{el.z} f_y / \gamma_{M0}} \right) \quad /1.18/$$

where

$$N_{Sd} = 1.35 \times 220 \times DLvar1 + 1.5 \times 45 \times LLvar1 + 1.5 \times 5 \times SLvar1 \text{ (kN)} \quad /1.19/$$

$$M_{y.Sd} = 1.35 \times 8 \times DLvar2 + 1.5 \times 3 \times LLvar2 + 1.5 \times 2 \times SLvar2 \text{ (kNm)} \quad /1.20/$$

$$M_{z.Sd} = 1.35 \times 3 \times DLvar3 + 1.5 \times 1.5 \times LLvar3 + 1.5 \times 0.5 \times SLvar3 \text{ (kNm)} \quad /1.21/$$

Failure occurs if $SF < 0$.

This safety function of rectangular hollow section is analyzed using the M-Star program.

The M-star output is shown in Figure 1.8.

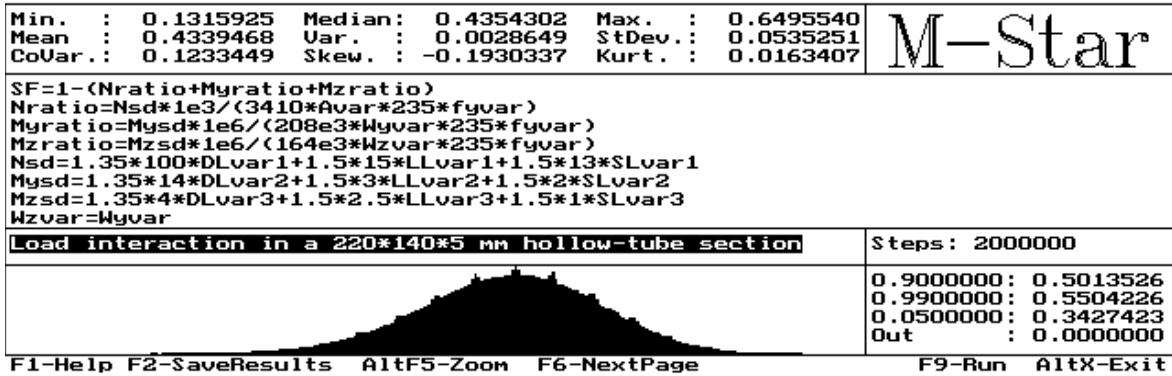


*Fig. 1.8 Three-component response of rectangular hollow section
(M-Star™ program output).*

Results and conclusions:

The 220 × 140 × 5 mm rectangular hollow section is safe according to SBRA technique, because the probability of failure $P_f = 0.00000$ is less than the assumed target probability $P_f = 0.00000 < P_d = 0.00007$. The rectangular hollow section is unsafe according to Eurocode 3, because for the safety function

$$SF_{EC} = 1 - \left(\frac{369}{34.1 \cdot 23.5 / 1.1} + \frac{1710}{208 \cdot 23.5 / 1.1} + \frac{675}{164 \cdot 23.5 / 1.1} \right) = -0.084 < 0.$$

This results shows that the semi-probabilistic based Eurocode contains safety reserve, what could be used applying the fully probabilistic calculation methods.

1.2.4. Shear resistance of a bolted beam to beam connection [7] [12]

Assignment:

Determine the shear resistance of the bolted beam to beam connection shown in Figure 1.9, corresponding to the probability $P = 0.01$. Investigate both bolt shear and bearing limit states. Assess the safety of a bolted splice connection under tension.

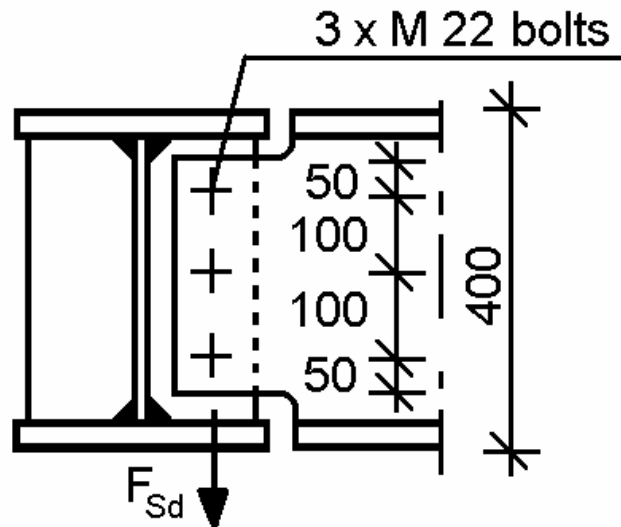


Figure 1.9 The geometry of the bolted beam to beam connection

Input and variables:

The beam to beam connection is comprised of 3 bolts, each with a diameter $d = 22 \text{ mm}$ and of grade 52. The geometrical data and variations are shown in Table 1.6. The variable ultimate shear stress τ_u defined by the product of the basic value $\tau_{u,nom} = 275 \text{ N/mm}^2$ and a factor represented by the histogram Fu355A.his. The variable ultimate bearing stress σ_u defined by the product of the basic value $\sigma_{u,nom} = 490 \text{ N/mm}^2$ and a factor represented by the histogram Fu355A.his.

Table 1.6 Geometrical data and variation

Geometrical data	Nominal Value	Variable	Histogram
d	22 mm	dvar	N1-05.his
t	12 mm	tvar	N1-10.his

Determination of the resistance of the connection

The resistance can be expressed either by the shear resistance or by the bearing resistance of the bolts. It is assumed that the resistance of the plates is higher than the resistance of bolts.

First, calculate the shear resistance of the bolts, which in this example is expressed as:

$$F_{v,Rd} = d_2 \times \pi / 4 \times \tau_u \tag{1.22/}$$

Then, determine the bearing resistance of the bolts. The external force causes normal stresses in the web plates and in the shaft of the bolts. The bearing resistance per bolt is expressed in this example as:

$$F_{b,Rd} = d \times t_{\min} \times \sigma_u \quad /1.23/$$

Application of simulation technique:

The resistances defined by equations /1.22/ and /1.23/, are calculated using the M-Star program. The results are shown in Figure 1.10 and Figure 1.11.

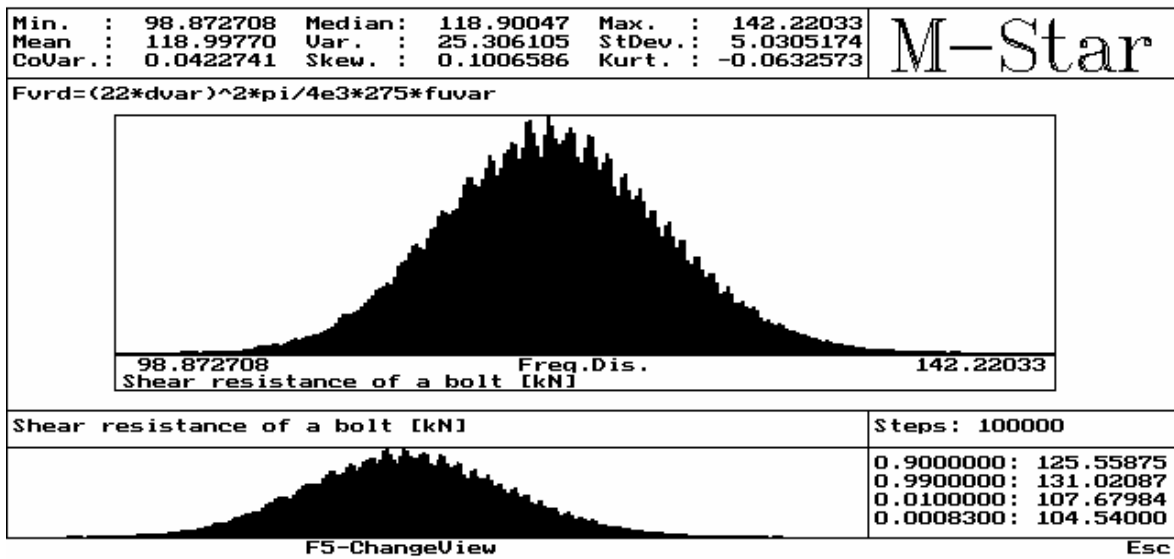


Figure 1.10 The shear resistance of one bolt (M-Star™ program output).

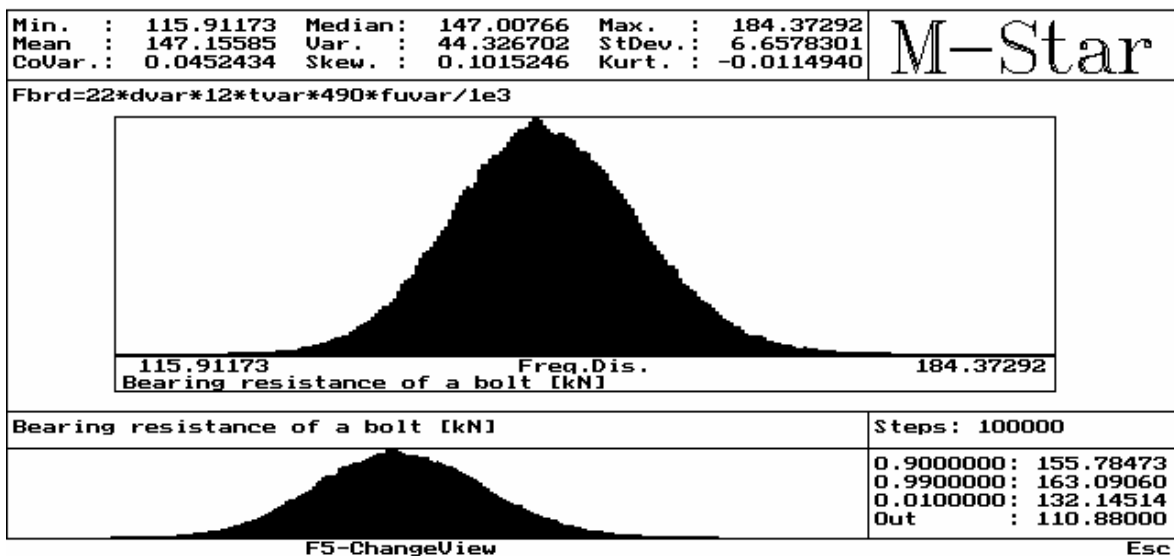


Figure 1.11 The bearing resistance of one bolt (M-Star™ program output).

Results and conclusions:

The shear and bearing resistances corresponding to the probability $P = 0.01$ are shown in Table 1.7. These resistances correspond to one bolt; therefore the resistance of the overall connection can be determined by multiplying the results by three. In this example, the shear resistance of the bolts is smaller than the bearing resistance; therefore the shear resistance of the bolts governs the design.

Table 1.7 The calculated resistances corresponding to probability $P = 0.01$

Type of resistance	Resistance
shear resistance	$F_{v,Rd} = 107.68 \text{ kN}$
bearing resistance	$F_{b,Rd} = 132.15 \text{ kN}$

1.2.5. Determination of the safety of the tee joint of a welded I-section according to Eurocode [7] [12]

Assignment:

Assess the safety of the welded tee joint between the web and the flange of an I-section according to Eurocode 3 [9]. The geometry of the connection is shown in Figure 1.12. This connection is at mid-span of a simply supported beam. The beam and the connection are subjected to a combination of dead load, long-lasting load and short-lasting load. All loads are mutually statistically independent. The tee joint is subjected to a bending moment and shear forces. The tee joint is safe if the probability of failure P_f is lower than the assumed target probability $P_d = 0.00007$ ($P_f < P_d$)

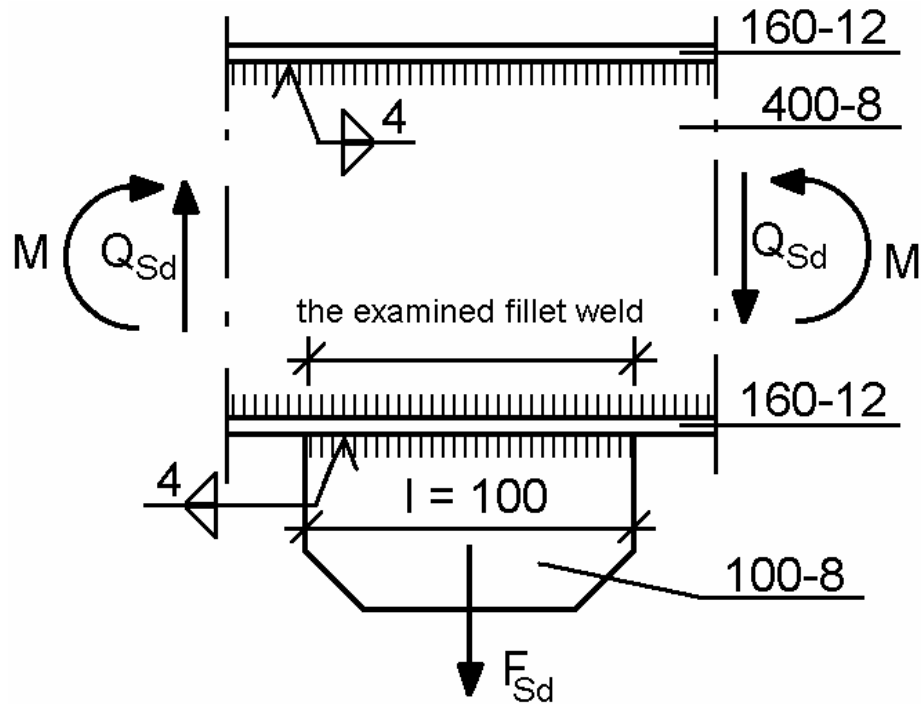


Figure 1.12 The geometry of the welded connection

Input and variables:

The cross section is a welded symmetrical I-section with a 400×8 mm web and a 160×12 mm flanges. The throat thickness of the fillet weld is $a = 4$ mm. The external loads and geometry are given in Table 1.8 and Table 1.9.

Table 1.8 Loadings and variations

Internal force (Q_{Sd})				
Load	Nominal Value	Extreme Value	Variable	Histogram
Dead load1	DL1 = 110 kN	$1.35 \times 110 = 148.5$ kN	DLvar1	DEAD2.his
Long-lasting1	LL1 = 80 kN	$1.5 \times 80 = 120$ kN	LLvar1	LONG1.his
Short-lasting1	SL1 = 65 kN	$1.5 \times 65 = 97.5$ kN	SLvar1	SHORT1.his
Externally Applied Force (F_{Sd})				
Load	Nominal Value	Extreme Value	Variable	Histogram
Dead load2	DL2 = 65 kN	$1.35 \times 65 = 87.75$ kN	DLvar2	DEAD2.his
Long-lasting2	LL2 = 50 kN	$1.5 \times 55 = 82.5$ kN	LLvar2	LONG1.his
Short-lasting2	SL2 = 40 kN	$1.5 \times 45 = 67.5$ kN	SLvar2	SHORT1.his

Table 1.9 Geometrical data and variation

Geometrical data	Nominal Value	Variable	Histogram
h	400 mm	hvar	N1-01.his
b	160 mm	bvar	N1-01.his
t _w	8 mm	twvar	N1-10.his
t _f	12 mm	tfvar	N1-10.his
a	4 mm	awvar	N1-10.his
l	100 mm	lvar	N1-05.his

The load variation is described by the histograms DLvar, LLvar and SLvar. The variation of the width and thickness of the plates express the variations of the geometric properties of the cross section. The throat thickness and the weld length are also considered as variables and are expressed by the histogram of awvar and lvar. The variable ultimate stress of the weld material f_u is defined by the product of the basic value $f_{u,nom} = 360 \text{ N/mm}^2$ and a factor represented by the histogram Fu235A.his.

Bearing capacity and load of the tee joint according to Eurocode 3

The failure of tee joint connection occurs by the fracture of the weld in the ultimate limit state. It is assumed that the resistances of the lower welded connection and the external plate are higher than the applied force.

In this example the safety of the internal fillet weld is calculated. The externally applied force F_{Sd} causes shear perpendicular to the length of the weld. From this shear, normal stresses perpendicular to the throat (σ_{\perp}) and shear stresses in the plane of the throat perpendicular to the axis of the weld (τ_{\perp}) occur. The internal shear force Q_{Sd} causes shear stresses in the plane of the throat parallel to the axis of the weld (τ_{\parallel}), which is calculated by Zhuravski's formula according to Timoshenko [11]. Normal stresses parallel to the axis of the weld (σ_{\parallel}) arise from the bending of the beam, but the effect of this stress component is negligible. The resistance of the fillet weld will be sufficient if the following condition is satisfied:

$$(\sigma_{\perp}^2 + 3 \times (\tau_{\perp}^2 + \tau_{\parallel}^2))^{0.5} \leq f_u / (\beta_w \times \gamma_{Mw}) \quad /1.24/$$

where:

$$\sigma_{\perp} = \tau_{\perp} = F_{Sd} / (2^{0.5} \times 1 \times a \times 2) \quad /1.25/$$

$$\beta_w = 0.8 \text{ and } \gamma_{Mw} = 1.25$$

the shear stress τ_{II} at the weld can be calculated using Zhuravski's formula:

$$\tau_{II} = Q_{Sd} \times S_y' / (I_y \times 2 \times a) \quad /1.26/$$

in which Q_{Sd} is the external load,

$$\begin{aligned} S_y' &= 395520 \text{ mm}^3 && \text{is the first moment of area of the upper flange} \\ I_y &= 2.057 \times 10^8 \text{ mm}^4 && \text{is the moment of inertia about the strong axis.} \end{aligned}$$

The applied loads are:

$$Q_{Sd} = 1.35 \times 110 + 1.5 \times 80 + 0.6 \times 1.5 \times 65 = 327 \text{ kN} \quad /1.27/$$

$$F_{Sd} = 1.35 \times 65 + 1.5 \times 50 + 0.6 \times 1.5 \times 40 = 198.75 \text{ kN} \quad /1.28/$$

The safety function can be expressed as:

$$SF_{EC} = \sigma_{Rd,EC3} - \sigma_{red,Sd,EC3} = 36 - 37.68 = -1.68 \text{ kN / cm}^2 < 0, \text{ i.e. the fillet weld is unsafe.} \quad /1.29/$$

where:

$$\sigma_{red,Sd,EC3} = (\sigma_{\perp}^2 + 3 \times (\tau_{\perp}^2 + \tau_{II}^2))^{0.5} = (17.57^2 + 3 \times (17.57^2 + 7.86^2))^{0.5} = 37.68 \text{ kN / cm}^2 \quad /1.30/$$

$$\sigma_{Rd,EC3} = f_u / (\beta_w \times \gamma_{Mw}) = 36 / (0.8 \times 1.25) = 36 \text{ kN / cm}^2 \quad /1.31/$$

Application of the simulation technique:

The applied loads are:

$$Q_{Sd} = 1.35 \times 110 \times DLvar1 + 1.5 \times 80 \times LLvar1 + 1.5 \times 65 \times SLvar1 \quad (\text{kN}) \quad /1.32/$$

$$F_{Sd} = 1.35 \times 65 \times DLvar2 + 1.5 \times 50 \times LLvar2 + 1.5 \times 40 \times SLvar2 \quad (\text{kN}) \quad /1.33/$$

The safety function can be expressed as:

$$SF = \sigma_{Rd} - \sigma_{red,Sd} \quad /1.34/$$

where:

$$\sigma_{red,Sd} = (\sigma_{\perp}^2 + 3 \times (\tau_{\perp}^2 + \tau_{II}^2))^{0.5} \quad /1.35/$$

$$\sigma_{Rd} = f_u / (\beta_w \times \gamma_{Mw}) \quad /1.36/$$

Failure occurs if $SF < 0$.

The safety of the welded connection is calculated by evaluating the safety function expressed by equation /1.36/. This analysis is performed using the M-Star program and the M-star output is shown in Figure 1.13.

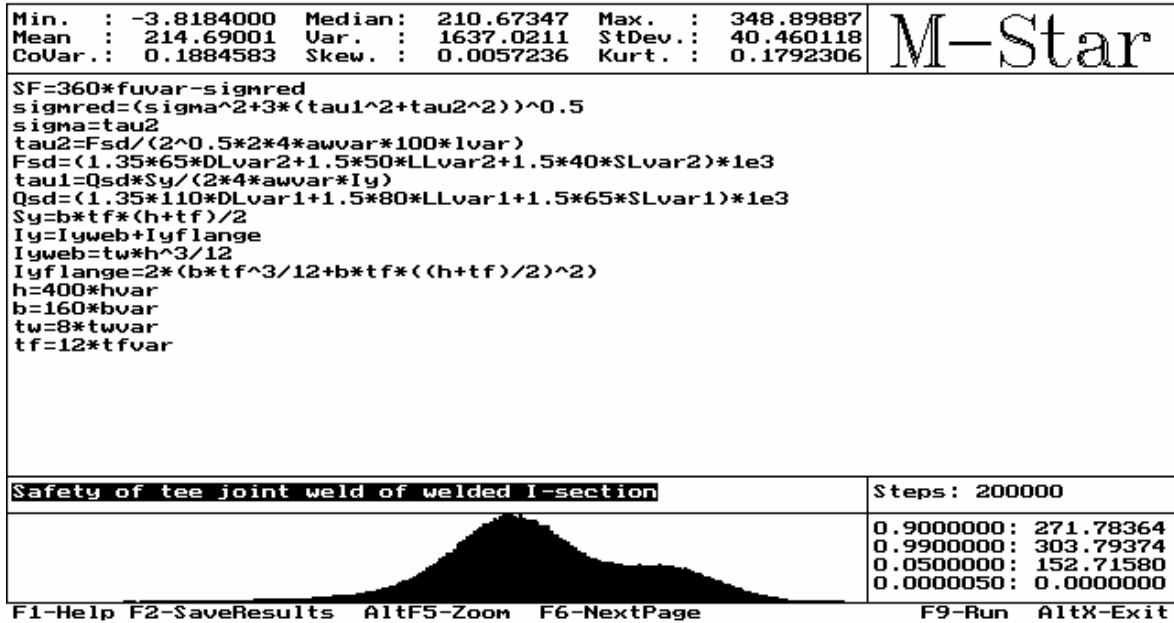


Figure 1.13 The safety of the welded tee joint (M-Star™ program output).

Results and conclusions:

The fillet weld is safe according to the SBRA technique, because the probability of failure $P_f = 0.000\ 005$ is less than the assumed target probability $P_f = 0.000\ 005 < P_d = 0.000\ 070$. The fillet weld is unsafe according to Eurocode 3, because for the safety function, $SF_{EC} = \sigma_{Rd,EC3} - \sigma_{red,Sd,EC3} = 36 - 37.68 = -1.68\text{ kN} / \text{cm}^2 < 0$.

1.3. Examination of the lateral buckling of welded I-section under bending [8]

This examination deals with the lateral buckling behaviour of a welded I-section (Figure 1.14.) simple supported beam. The function between the reduction factor for flexural torsional buckling (ϕ) and the non-dimensional slenderness ($\bar{\lambda}$) is simulated [1].

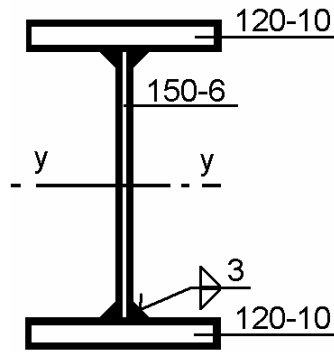


Figure 1.14. Cross section of welded beam

The examination was done on the basis of an ideal model. The beam is under uniform bending moment (Figure 1.15), and the critical bending moment, which causes the lateral buckling of beam can be determined [2]:

$$M_{cr} = \frac{\pi}{L} \sqrt{EI_z \left(GI_t + EI_\omega \frac{\pi^2}{L^2} \right)} \quad /1.37/$$

where:

$I_z = 288 \text{ cm}^4$ is the moment of inertia about z-axes, $I_t = 9 \text{ cm}^4$ is Saint Venant torsion constant, $I_\omega = 18432 \text{ cm}^6$ is the warping constant, L is the beam span, Young's Modulus $E = 21000 \text{ kN/cm}^2$ and the shear modulus $G = 8077 \text{ kN/cm}^2$.

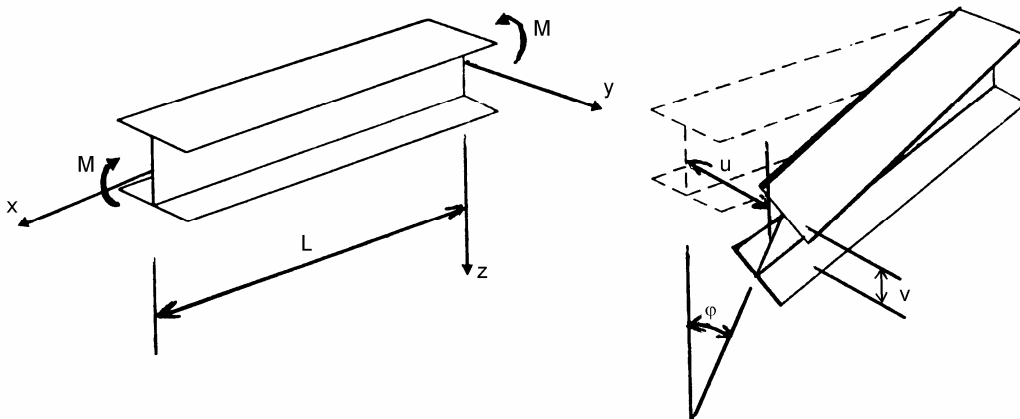


Figure 1.15. The behaviour of simple supported beam

The computer simulation was done by M-StarTM program. The assumed distribution of the geometrical data (the widths and thicknesses of plates and the length of beam) are Gaussian probability density function, with deviation $\pm 5\%$. The variation of yield stress f_y ,

is represented by histogram Fy255A.his and $f_{y,nom} = 235 \text{ N/mm}^2$. This histogram is based on experiments and described in M-StarTM program.

During the computer simulation the length of the beam was changed, and the corresponding critical bending moment were calculated 100 000 times in each case, and the results were evaluated statistically. Then from the critical moment (M_{cr}) and the moment resistance (M_{Rd}) of beam the non-dimensional slenderness and reduction factors can be determined as follows:

non-dimensional slenderness is $\bar{\lambda} = \sqrt{\frac{M_{Rd}}{M_{cr}}}$, and the reduction factor is $\phi = \frac{M_{cr}}{M_{Rd}}$.

The experimental lateral buckling curves for welded and rolled I-sections, the lateral buckling curves of Hungarian Design Code (MSZ 15024) and Eurocode are in Figure 1.16. The simulated lateral buckling curve is the Monte Carlo simulation curve on the Figure 1.16.

The AntHillTM program was used to evaluate directly the simulated lateral buckling curve, which is on the Figure 1.16.

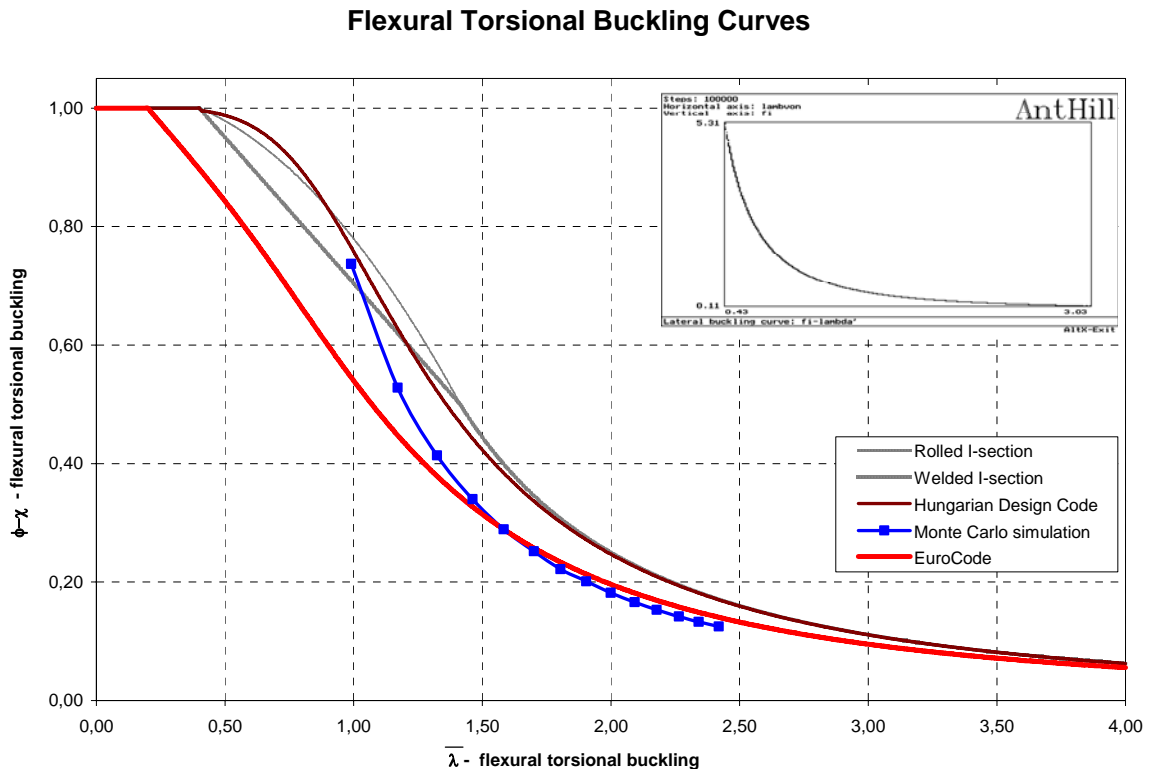


Figure 1.16. Lateral buckling curves of simple span beam

The simulation and the Eurocode curve are in good coincidence.

1.4. Parametrical examination a column in a simple frame [8]

Examine the buckling curve of a compressed column of a simple frame shown in Figure 1.17. In this example 2nd order elastic analysis is applied, and so axial force effects are taken into account by stability functions.

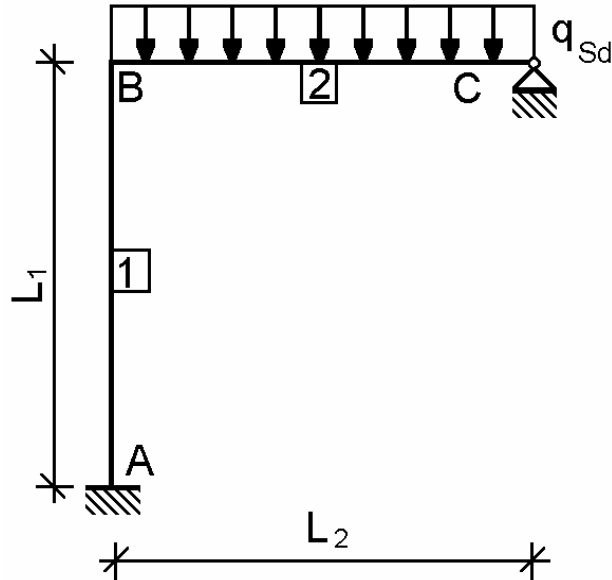


Figure 1.17 The geometry of simple frame

The beam is HEB 160 section with moment of inertia $I_{y,nom} = 2492 \text{ cm}^4$ and the column is HEB 140 with moment of inertia $I_{y,nom} = 1509 \text{ cm}^4$. The elastic sectional modulus of column is $W_{y,nom} = 215.6 \text{ cm}^3$.

The maximum bending moment on column will be at the upper end of column. The maximum bending can be calculated by the displacement method and applying stability functions since only one displacement is unknown: the rotation of connection B, θ_B . The rotation of connection B is calculated according to Iványi [2]. The moment equilibrium equation of connection B will be used to determine the rotation:

$$\Sigma M_B = (s_1 \times k_1 + 3 \times k_2) \times \theta_B - q_{Sd} \times l_2^2 / 8 = 0 \quad /1.38/$$

where:

$$k_1 = EI_1 / l_1, \quad k_2 = EI_2 / l_2 \quad \text{and } E \text{ is the Young's modulus } E = 210000 \text{ N/mm}^2.$$

The s_1 stability function can be calculated using the method of Livesley [4].

The normal force in the column is $P = 5 / 8 \times q_{Sd} \times l_2$ and the Euler critical buckling load is

$$P_E = \pi^2 \times E \times I_y / l_1^2 = \pi^2 \times k_1 / l_1.$$

The ratio between the axial force and the Euler load:

$$\rho_1 = P / P_E = 5 / 8 \times q_{sd} \times l_2 \times l_1 / (\pi^2 \times k_1) \quad /1.39/$$

The s_1 stability function now can be calculated:

$$s_1 = \frac{0,25\pi^2 \rho_1 + \Phi_1 - \Phi_1^2}{1 - \Phi_1} \quad /1.40/$$

where

$$\Phi_1 = \frac{64 - 60\rho_1 + 5\rho_1^2}{(16 - \rho_1)(4 - \rho_1)} - \sum_{n=1}^{n=7} \frac{a_n \rho_1^n}{2^{3n}} \quad /1.41/$$

in which $a_1 = 1.5797362$, $a_2 = 0.15858587$, $a_3 = 0.02748899$, $a_4 = 0.00547540$, $a_5 = 0.00115281$, $a_6 = 0.00024908$ and $a_7 = 0.00005452$.

The rotation of connection B is expressed from Eq. /6/:

$$\theta_B = q_{sd} \times l_2^2 / 8 / (s_1 \times k_1 + 3 \times k_2) \quad [\text{radian}] \quad /1.42/$$

The maximum bending moment on the column M_{sd} now can be calculated:

$$M_{sd} = s_1 \times k_1 \times \theta_B \quad [\text{kNm}] \quad /1.43/$$

The moment resistance of the column section is:

$$M_{Rd} = W_{el} \times f_y = 215.6 \times W_{var} \times 23.5 \times f_{yvar} / 100 \quad [\text{kNm}] \quad /1.44/$$

The critical distributed load on the beam can be determined, because in that case:

$$M_{Rd} = M_{sd}. \quad /1.45/$$

The computer simulation was done by M-StarTM program. The assumed distribution of the geometrical data (the moment of inertia and lengths of beam and column) are Gaussian probability density function, with deviation $\pm 5\%$. The variation of yield stress f_y , is represented by histogram Fy255A.his and $f_{y,nom} = 235 \text{ N/mm}^2$. This histogram based on experiments and described in M-StarTM program.

During the computer simulation the lengths of column and beam were changed, and the corresponding critical intensity of distributed load was calculated by iterations 100 000 times in each case, and the results were evaluated statistically.

The evaluated cases are in Table 1.10 and the results are on Figure 1.18.

The calculated buckling surface has the critical intensities of distributed load of column. The critical surface of beam should be also calculated and the intersection of the two surfaces would give the 3D curve of the critical intensities of distributed load of total frame.

Table 1.10 The critical intensity of distributed load of the column

Length of column [m]	Length of beam [m]	$q_{cr,column}$ [kN/m]
2	4	45.2
2	6	17.5
4	3	135.0
4	4	63.3
4	6	22.7
4	8	11.3
4	10	6.7
6	3	193.0
6	4	84.2
6	6	28.4
6	8	13.6
6	10	7.8
8	4	115.3
8	6	34.8

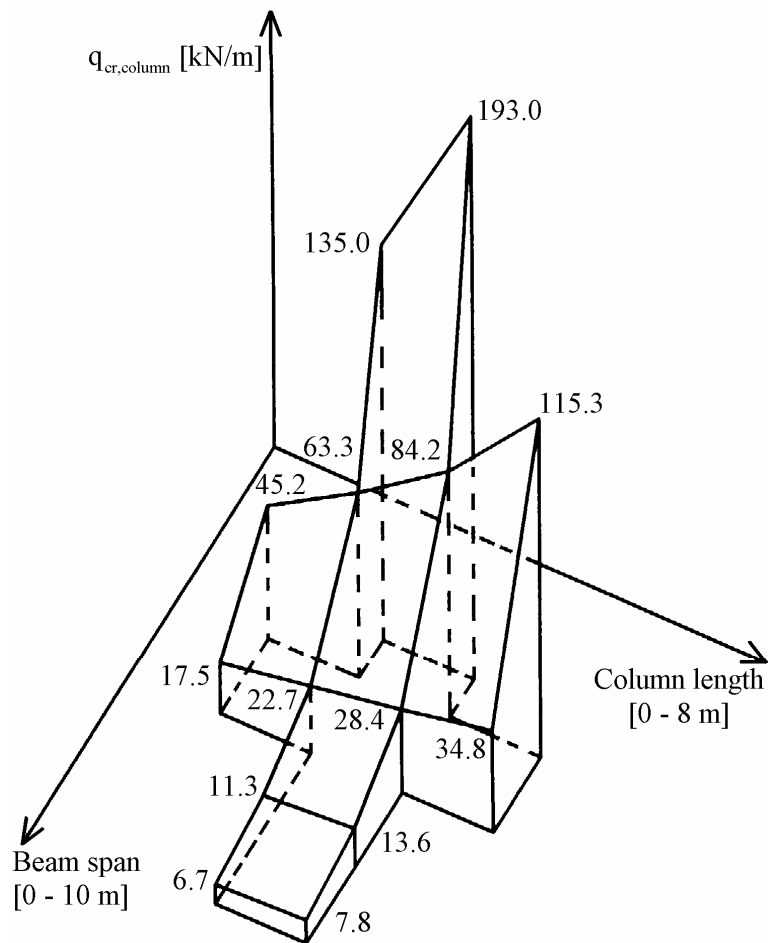


Figure 1.18 The buckling surface of column

1.5. Conclusions

In this chapter I presented design processes based on full-probabilistic methods applying on typical examples from the field of structural design. The design parameters are presented as random variables, which are expressed by bounded histograms, and I evaluated the design conditions by the help of Monte Carlo simulation technique. Comparative calculations were made on semi – probabilistic methods of design codes, and I demonstrated the benefits of full – probabilistic methods. Applying numerical simulations and stability functions I generated the load bearing surface of a column in a simple frame.

New results of this chapter: Simulation applying Monte-Carlo method

a) buckling curves

I applied Monte-Carlo method for modelling the lateral buckling behaviour of a welded I-sectioned simple supported beam. The examination was done on the basis of an ideal model. The beam is under uniform bending moment. The assumed distribution of the geometrical data (the widths and thickness of plates and the length of beam) are Gaussian probability density function. During the computer simulation the length of column was changed, and the corresponding critical bending moment were calculated. Thus I produced the buckling curve of that welded I-sectioned beam.

b) structural elements

I applied Monte-Carlo method for calculating the safety of different structural elements. The calculated problems were typical structural exercises such as: safety of a truss-girder bar subjected to tension, safety of a rectangular hollow section exposed to multi-component loads, safety of a column in a frame, safety of the tee joint of a welded I-section, shear resistance of a bolted beam to beam connection.

During this calculation I showed the potential of the Monte-Carlo method in the engineering practice, and pointed out the possible advantage against the design codes.

c) buckling behaviour of a steel frame

I applied Monte-Carlo method in a parametrical examination at a single beam-column frame. During the calculations the lengths of column and beam were changed and the corresponding critical buckling intensity of distributed load of the column was calculated.

Elastic and 2nd order analysis was applied, thus the axial force effects are taken into account by stability functions.

As the result of the calculations the buckling surface of column was produced with the critical intensities of distributed load.

References I.

- [1] Edlund, Bo L.O. and Leopoldson, Ulf L. C. (1975), *Computer simulation of the scatter in steel member strength* Computers&Structures, Vol. 5, pp. 209-224.
- [2] Iványi, M. (1995), *Stability Theory (Stabilitástan)* Budapest University Press, Budapest.
- [3] Kleinen, J.P.C. (1975), *Statistical Techniques in Simulation* 1st edition, Marcel Dekker, New York, N.Y.
- [4] Livesley, R.K. and Chandler, D.B. (1956), *Stability Functions for Structural Frameworks* Manchester University Press, Manchester.
- [5] Marek, P., Guštar, M. and Anagnos, T. (1995), *Simulation-Based Reliability Assessment for Structural Engineers* CRC Press, Inc., Boca Raton, Florida.
- [6] Marek, P., Guštar, M. and Bathon, L. (1998), *Tragwerksbemessung. Von deterministischen zu probabilistischen Verfahren* (in German), Academia, Praha.
- [7] Marek, P., Brozzetti, J. and Gustar, M. editors: *Probabilistic Assessment of Structures using Monte Carlo Simulation*, TeReCo Product, ITAM CAS CR, Prague, 2001 June
- [8] Fülöp A., Iványi M. *Computer Simulation of the Buckling Curves for Steel Structures using Monte-Carlo Method* In: Li Hyung Lee, Ginzstler János, editors, Proceedings of the 3rd Korean-Hungarian Symposium on “New Methods in structural engineering”, (organizer: Hungarian Academy of Engineering), Budapest, Hungary, 2001. June 22., Seoul, KAIST, 2002
- [9] ENV 1993-1-1 : *Design of steel structures Part 1-1: General rules and rules for buildings, Annex M [normative]: Alternative method for fillet welds*, 1992
- [10] ENV 1993-1-1: *Design of steel structures Part 1-1: General rules and rules for buildings, Section 5.4: Resistance of cross-sections*, 1992
- [11] Timoshenko, S.: *Theory of Elasticity*, McGraw-Hill Book Company, Inc., 1951
- [12] Dr. Iványi Miklós – Fülöp Attila, szerkesztők: *Acélszerkezetek szimulációs vizsgálatai megbízhatósági eljárással - Examination of Steel Structures using Simulation-based Reliability Assessment (SBRA-method)*, Műegyetemi Kiadó, Budapest, 2001, ISBN 963 420 680 8, p.286

2. Simulations of producing and design of structures

The computer FEM analyses are widely used in structural analyses by engineers. The different programs, based on FEM, finite strip or other mechanical methods, give the possibility for adequate analyses of structures on computer models. Modifying the input parameters lots of analyses can be done without structural damage. Furthermore computer programs are useful in evaluating structural laboratory tests. New calculating methods and procedures can be evaluated on the results of these modelling.

The evolution of computer hardware and software gives the possibility to use more complex programs and models.

In my work the computer modelling runs in two levels, modelling the whole structures and modelling the structural elements themselves. AxisVM finite element programs were used modelling the space-truss segment. The numerical analyses of structural bars were performed by ABAQUS version 6.3-2 finite element program using for pre- and post-processing the MSC Patran 2000 r2 program.

2.1. Simulation of the formation procedure of the bars

2.1.1. The formation procedure of the bars

The joint set-up of the Hungarian TOP-SYSTEM space-truss system, which was developed by DUNAFERR Iron Work Company, requires special end shape of the bars. The sides of the rectangular hollow members are formed with the help of excessive plastic deformations to the flattened shape. The deformation of the plate elements of the members and the development of the plate buckling state are analyzed. The special "flattening" process is described. Using an appropriate finite element model and analysis, the "flattening" process is modelled, and the results of the finite element analysis are compared to the results of the manufacturing process.

The special procedure for the formation of the edges involves a four stage process to ensure the sufficient shape of bars, which is connected to a gusset plate with bolts. This procedure is applied at DUNAFERR. The procedure is done in a hydraulic ram applying different tools for the different stages. I've looked and measured the tools at DUNAFERR. The hydraulic ram is displacement controlled during the stages of manufacturing.

The hollow section bars are cut to the final length. The first stage of the manufacturing is the splitting. The hollow members pushed onto a prod and cut by the ram, Figure 2.1.

The photos on the following 3 figures show just the steel tools without the cold-formed rectangular hollow sections. This cut is the place of the connection to the joint plate.

The second stage is the pressing. The split members are pulled over onto a gusset plate in the pressing tool. The cross section is pressed in the vertical direction pressing the half deformed shape of the member. Then the members are pulled out, rotated upside down and pushed back to the tool pressing the opposite half of the final shape of the bar ends, Figure 2.2.

The third stage of the formation procedure is the punching the holes for bolts into the members. The punching is made in hydraulic ram with a new tool. There are shaped supporting and guiding plates in the punching tool, and the holes can be ready easily, see Figure 2.3. The deformation process is ready. The final stage is welding of reinforcing plates into the flattened ends of the member ensuring the sufficient load bearing capacity of the bolted connections.

The investigated space-truss has uniform bars for diagonals and plate bars, thus these tools and the hydraulic ram are adequate for mass production. Before the computer modelling it was important to study the production process, getting all information from the manufacturer.

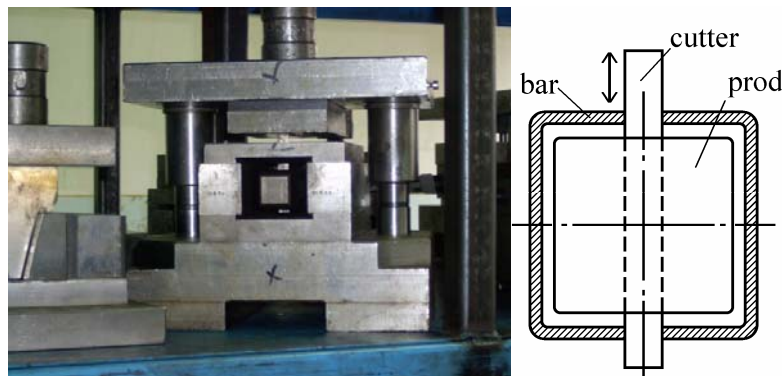


Figure 2.1 First stage: splitting.

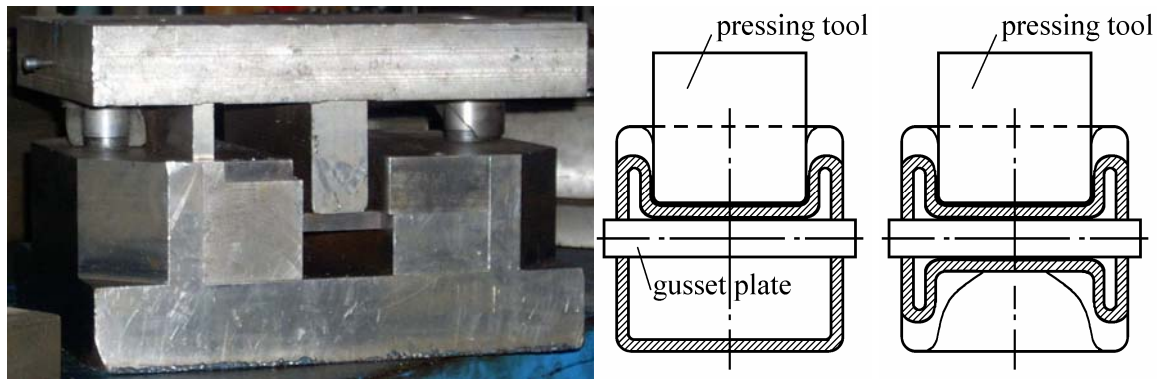


Figure 2.2 Second stage: pressing.

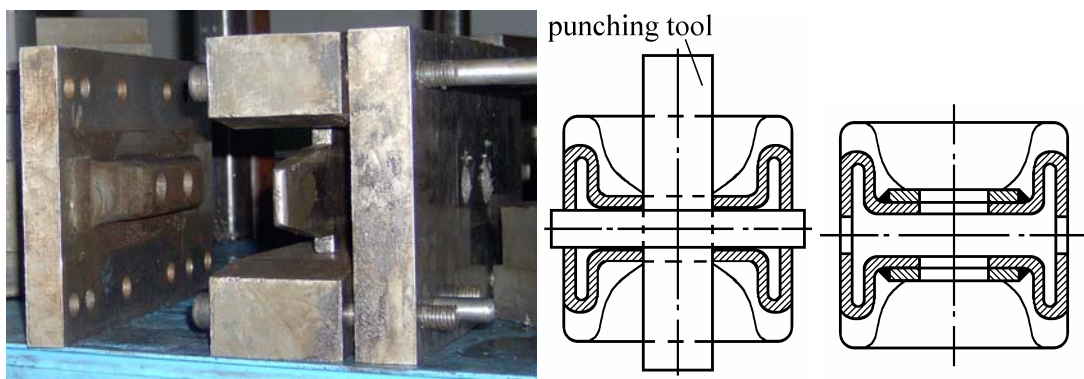


Figure 2.3 Third stage: punching; and the reinforced cross-section.

2.1.2. Numerical modelling of the formation process

The final goal of the numerical modelling is to simulate the behaviour of space-truss bars under different load cases, and find that case, which is in the real space-truss. The first step is to model the bar with the special flattened ends. I had to model the formation process to obtain the real model of flattened bar ends.

In order to simulate the formation process, numerical model is created. Just the second stage, pressing is analysed by ABAQUS finite element program, the pre- and post-processing are made by MSC Patran 2000 r2 program.

The bars are $60 \times 60 \times 2$ mm hollow tube sections; the theoretical length is 1200 mm. The formation takes effect just at the end of the bars. Therefore it is decided to model only a part of the bar, near the flattened end instead of the whole member. The length of the modelled part is sufficient if any effect caused by the flattening process is remaining within the model.

Furthermore it is decided to model only the quarter of the hollow cross section and the half of the pressing tool due to the symmetry of the members and the formation process. Using appropriate symmetry conditions in the x-z and y-z planes along the model edges simulated the continuity, Figure 2.4.

For modelling the bar members a 4-node thick shell element is used (element type S4R of the ABAQUS program library). The geometry of $60 \times 60 \times 2$ mm cold-formed rectangular hollow section is in the section catalogue. The length of the model bar is 200 mm.

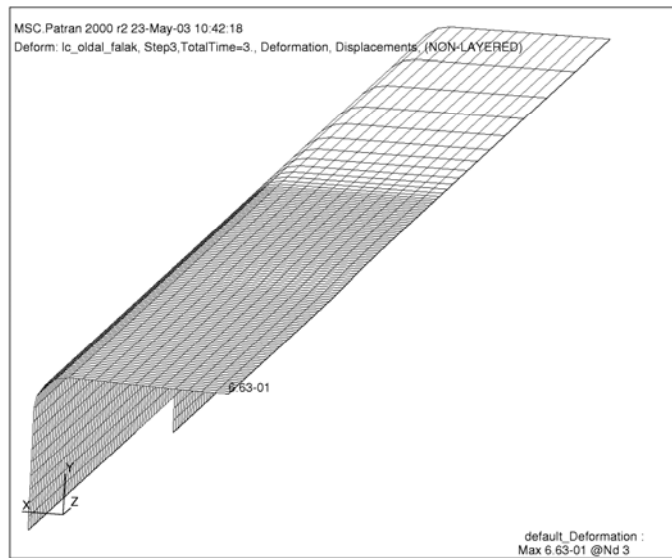


Figure 2.4 The FEM model of the quartered hollow section

The geometry of the pressing tool is given by the DUNAFERR Iron Work Company. For modelling the pressing tool a 4-node rigid body element is used (element type R3D4 of the ABAQUS program library) (see Figure 2.5).

The gusset plate of pressing was modelled by an L-shaped rigid surface as a contact surface. This surface supports the web plate of member and allows deforming the flange plate of member to the required shape. The lower edge of web plate has y-y symmetry; the edge of the flange plate of the model has x-x symmetry. The non-deformed end of the member is fully supported. Furthermore a vertical, rigid surface is applied along the web plate of the model supporting the horizontal deflection. Between the rigid bodies and the steel member the steel-steel friction is considered.

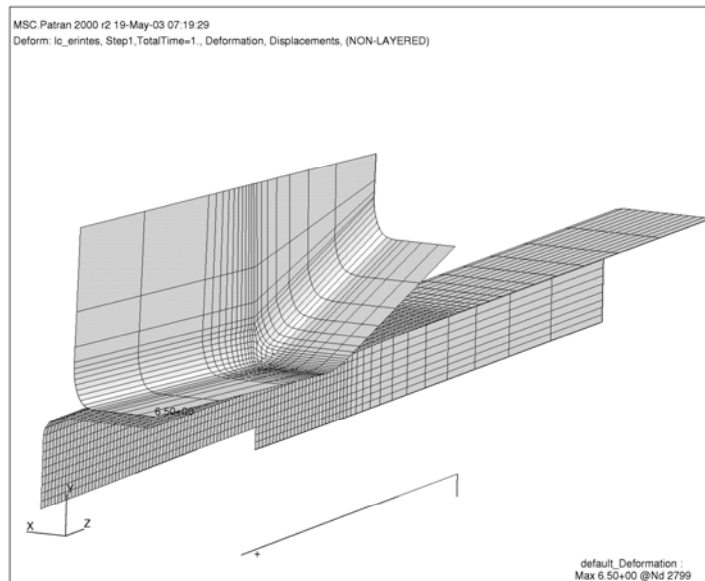


Figure 2.5 The FEM model of the pressing tool and the gusset plate

The steel material is supposed to be elastoplastic with isotropic hardening. The Young's modulus $E = 210\,000\text{ N/mm}^2$, Cauchy stresses $f_y = 405\text{ N/mm}^2$, $f_u = 470\text{ N/mm}^2$, $\epsilon_p = 0,2\%$. The material properties come from tension experiments of the basic material. This material is defined according to the ABAQUS program library applying *ELASTIC and *PLASTIC keywords and the adequate parameters. The yield surface follows the Von-Mises criterion. Stabilized nonlinear static analysis was applied with frontal linear equation solution, described in ABAQUS program library. In order to handle the contact conditions, an appropriate algorithm was used by ABAQUS.

Five-step procedure was used in the simulation of the flattening process. The loading was displacement controlled. At the first runs of the analysis numerical singularity problems occurred at the contact surface elements between the pressing tool and the member. I tried to press the member by the rigid body directly as done in the real pressing process. At that moment as the pressing tool touched the member lots of non-stressed nodes contacted each other in the contact surface simultaneously. The forces and stresses were very small and changed their sign rapidly. The ABAQUS solving process did not found the equilibrium state, and the analysis was terminated by the numerical singularity problems. To avoid this problem I modified the beginning of the process, which does not affect the final state of the deformed member, but eliminated the numerical singularity.

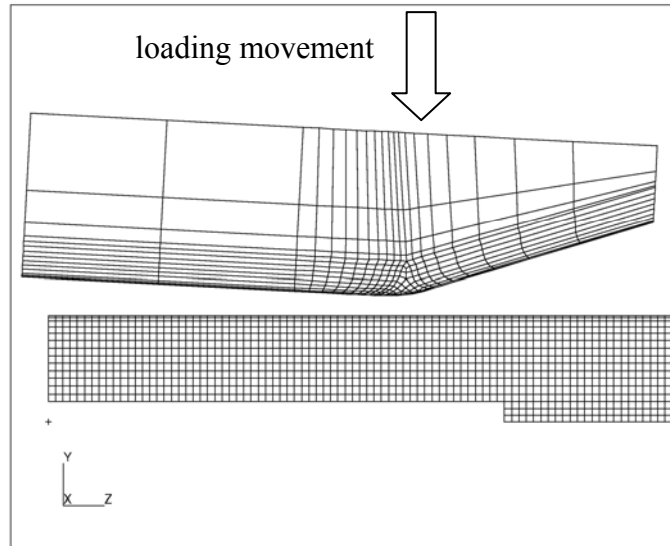


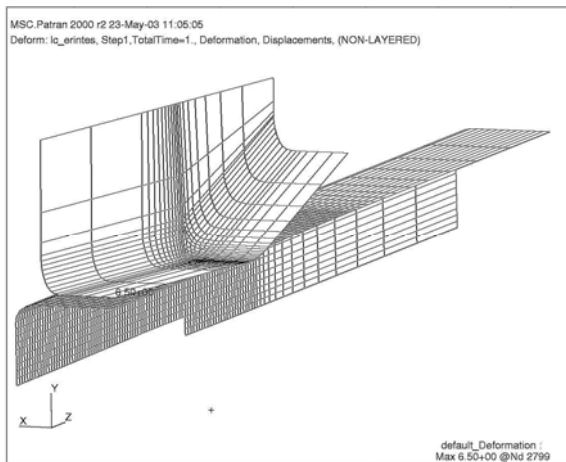
Figure 2.6 The starting rotated position of pressing tool

The pressing load is applied through the movement of the rigid body (Figure 2.6). Every procedure step has calculating time 1, which means the total time at the end of the simulation is 5 (for example the pressing phase is between total time 3 and 4). The integer value of total time means the end state of the sufficient step; the real value means an intermediate state of the actual step. At the beginning the pressing tool is rotated by 3° around x-axis, Figure 2.6.

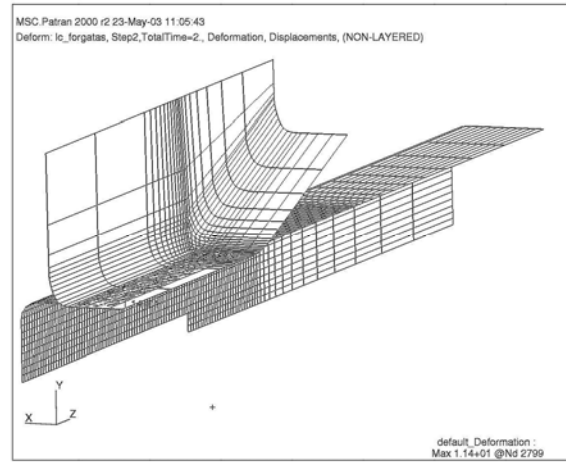
In the first step (Step 1) of the procedure the pressing tool is moved into the member by 0.5 mm (the wall-thickness is 2 mm). The gusset plate and the vertical rigid supporting plate in this step do not contact to the member. Thus the tool and the member are touched in a tight strip instead of the whole contact surface and the ABAQUS solves the equilibrium state.

During the second step (Step 2) the pressing tool is rotated back to the horizontal position by 3° again around the x-axis. In this step during the rotation numbers of the contacted elements are increased permanently without numerical problem. At the beginning of the third step (Step 3) the pressing tool is in horizontal position and contacted with the hollow member in the whole lower surface. In this step the gusset plate and the vertical rigid supporting plate is moved to the member making them contact and support. The fourth step (Step 4) is the most important step; the effective pressing was done with large plastic deformations. The pressing load applies again through the vertical movement of the rigid tool. The first three steps needed 20-30 load increments each, but the fourth step needed 150 load increments, due to the large deformations and rotations. The final

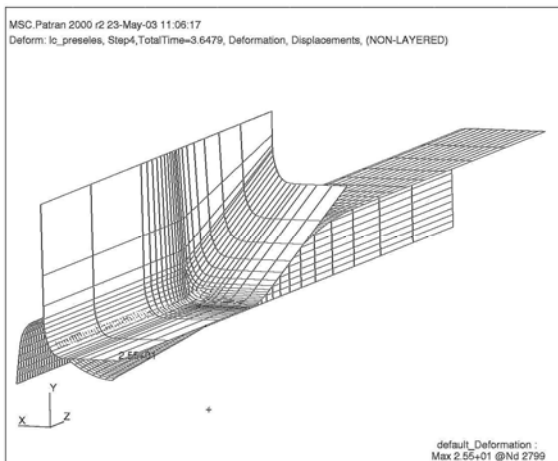
step (Step 5) is the unloading, when the pressing tool pulled back in 40 load increments into the starting position. The flowchart of the pressing is on Figure 2.7.



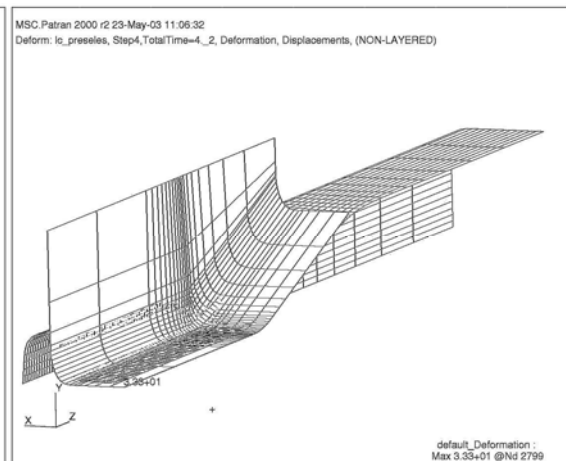
touching (total time: 1.0)



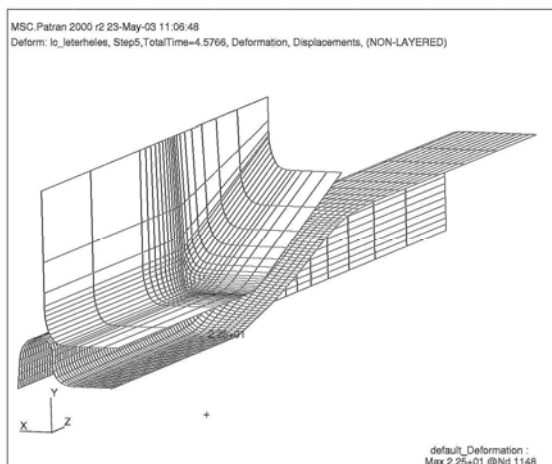
rotating back to horizontal position (total time: 2.0)



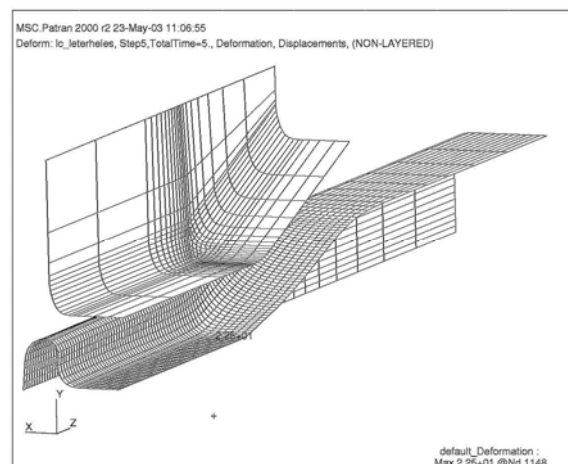
pressing (total time: 3.65)



pressing (total time: 4.0)



unloading (total time: 4.58)



unloading, final state (total time: 5.0)

Figure 2.7 The flowchart of the pressing procedure.

The hollow member follows the same states during the pressing procedure as it happens in the manufactory. During the real manufacturing this pressing procedure happens twice at both ends of the bars. Figure 2.8 shows the final shape of the member, which shows good coincidence with the real bars. This coincidence is investigated with a very new and interesting procedure. The comparison is described in chapter 2.1.4.

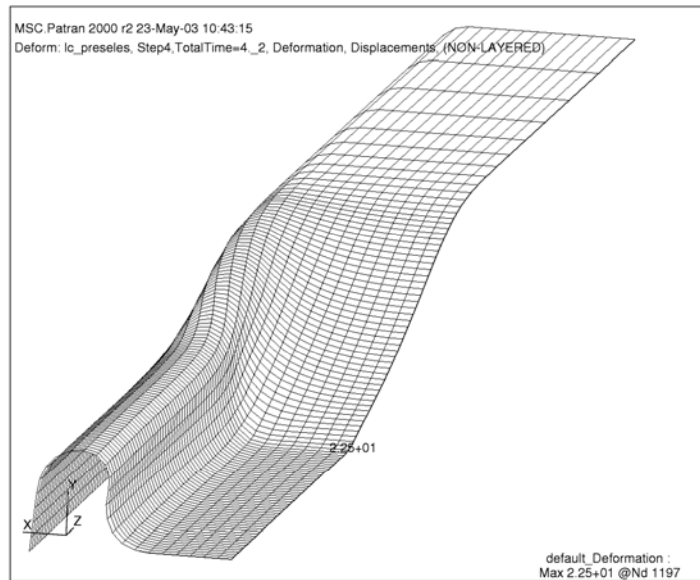


Figure 2.8 The result of the pressing stage

2.1.3. Results of the numerical analysis

The ABAQUS FEM program gives the possibility to monitor several mechanical data during the numerical analyses. These data could be for example different kind of stresses at the stress points of finite elements; elastic and plastic strains in the loaded members; deformations (displacements, rotations) of finite elements; the reaction forces at the supports and between the connected surfaces; etc. These data could be saved at every finite element in every load step. My FEM model is quite fine, due to the big deformations. Therefore big amount of data could be arisen, if I save all of the possible resulted data. Due to the memory capacity limit of the computer, I saved the monitored data just every fifth or tenth load increments and of course at the end of every load step.

The Figure 2.9 shows the reaction force [kN] – displacement [mm] curve of the pressing tool. The curve starts at 6.5 mm displacement, because the starting position of pressing tool was 6.5 mm over the bar. The first part of the curve is linear, that means the bar has linear elastic deformations. When the flange plate of the bar starting contacted to the gusset plate

the slope of the curve is increased, because the shaping requires more and more plastic deformation and more load. The end part of the curve is tangential to the vertical axis. At 28.5 mm deflection the rigid pressing tool reached the rigid gusset plate theoretically. In reality there is a two mm thick steel plate between them. Therefore from 26.5 to 28.5 mm (wall thickness = 2 mm) the reaction force increasing to be infinite and wall thickness of the member decreasing to be zero. The maximal reaction force according to the analysis is approximately 50 kN. At the DUNAFERR the different tools, which are used to the manufacturing, are designed for a hydraulic ram with maximal capacity of 630 kN.

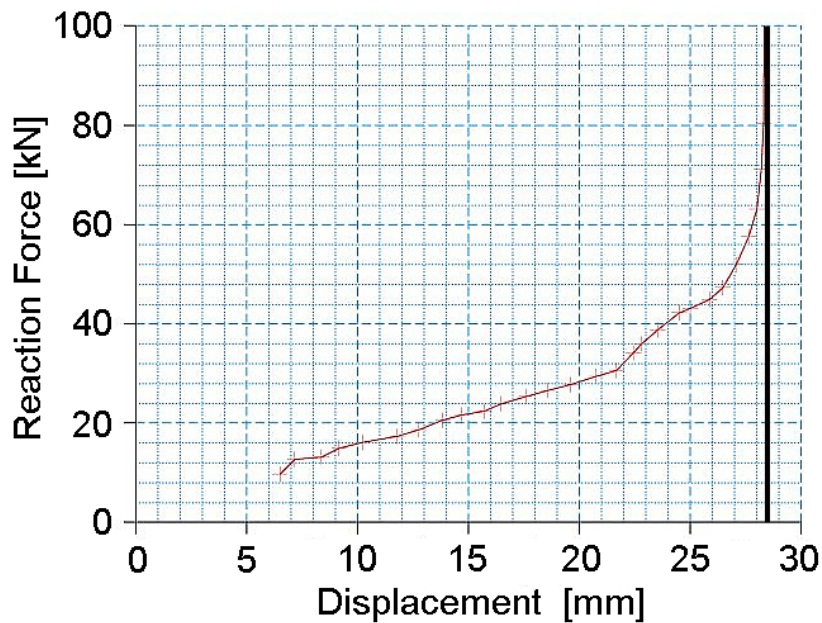


Figure 2.9: Reaction force [kN] – displacement [mm] curve of the pressing tool.

Stresses and strains were checked during the deformation process. Figure 2.10 and Figure 2.11 give some example results about the pressing procedure. On Figure 2.10 the Von-Mises stresses [N/mm²] and plastic strains are shown on the deformed shape of the member at the end of Step 4-pressing, where the formation procedure ends. The simultaneous stresses and plastic strains show very similar distribution on the deformed bar. From the figures it can be seen, that the assumption, modelling only a part of the member near the flattened end, was appropriate, because at the un-deformed end of the member there is no effect (stress or strain) of the deformation procedure. The maximum plastic strains (0.145) and stresses (517 N/mm²) are at the inner edge and the inner corner of the deformed shape.

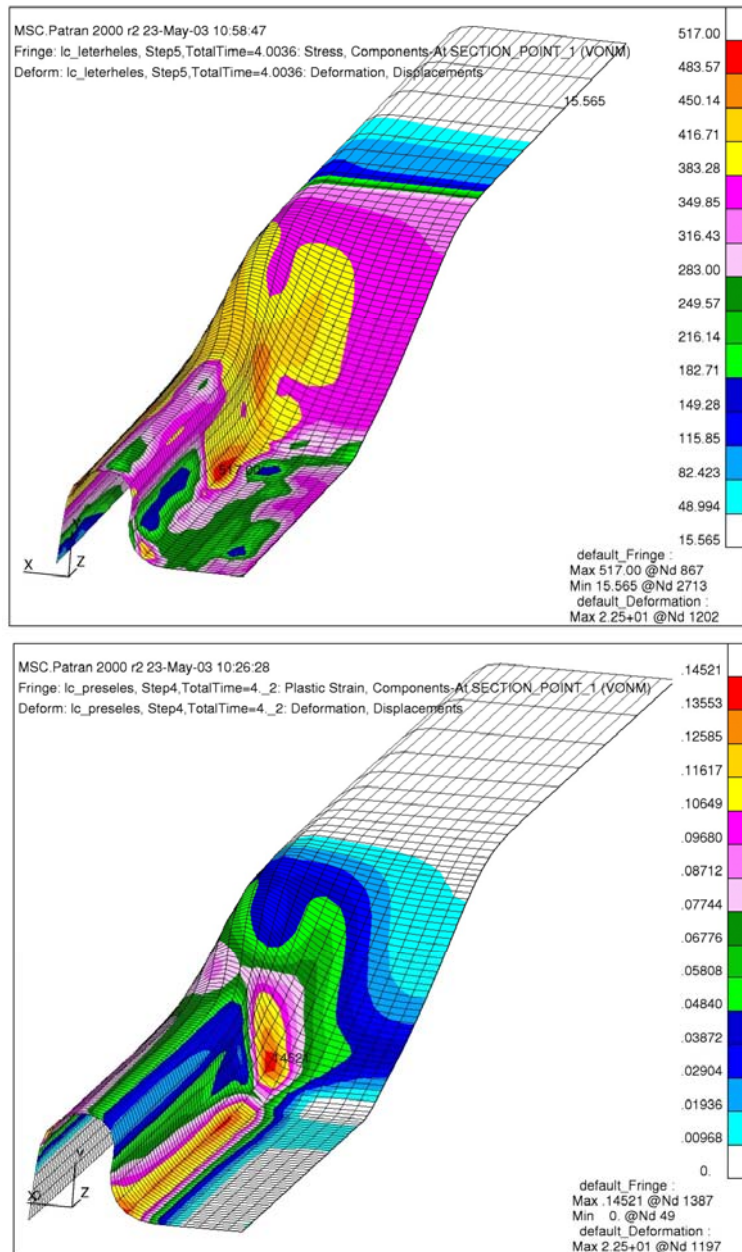


Figure 2.10 Von-Mises stresses $[N/mm^2]$ and plastic strains at the end of Step 4-pressing.

Figure 2.11 gives the Von-Mises stresses and strain components on the deformed shape of the member at the end of Step 5-unloading, where the pressing tool, the gusset plate and the vertical rigid surface are removed, so the member is unloaded. It is interesting to notice the remained stresses after the formation procedure.

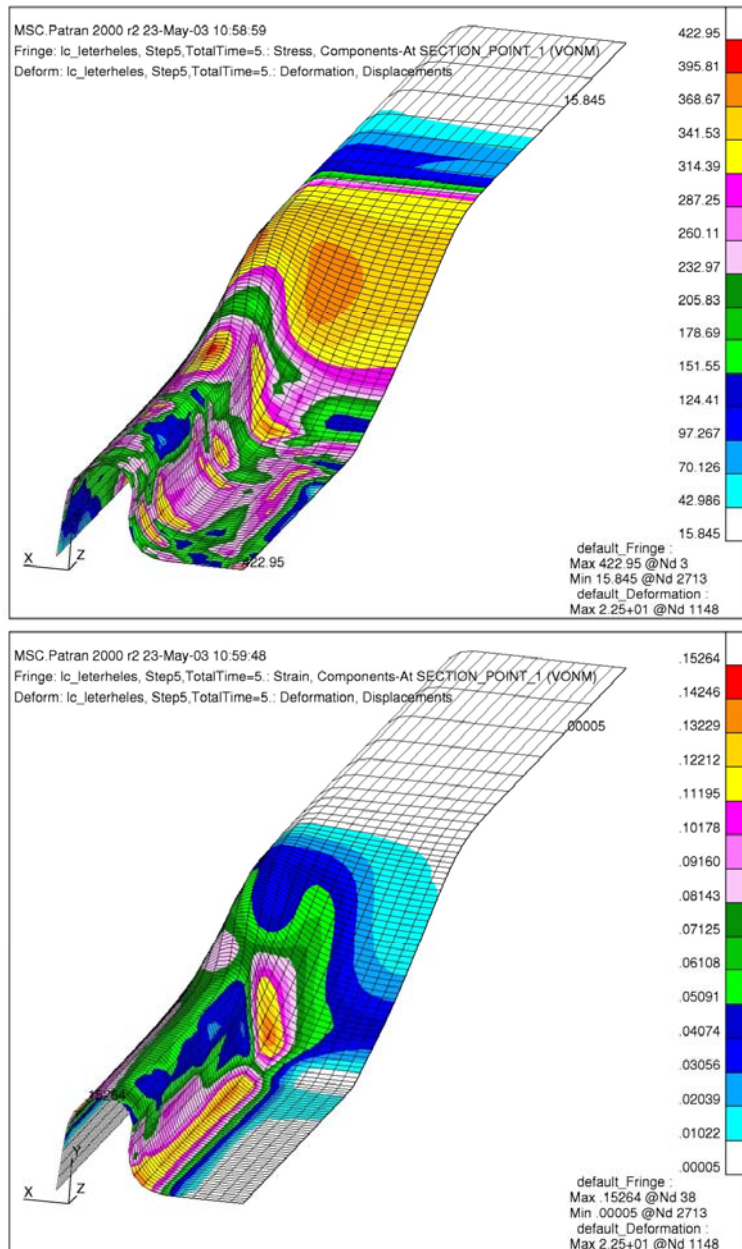


Figure 2.11: Von-Mises stresses [N/mm^2] and strain components at the end of Step 5-unloading.

2.1.4. Verifying the calculated result

During a numerical analysis it is an important question if the model good enough for our requirements. The suitability of the numerical model and the calculated results must be verified. A new method could be used for this verification: the 3D laser scanning procedure.

The MTA SZTAKI (Hungarian Academy of Sciences, Budapest) gave the possibility to examine the original and the buckled bars. The apparatus is a three-dimensional laser

scanner, which digitalizes any object within the range of movement. The parts of the apparatus are a laser generator, which is built on an armed mechanism, and an examining table, see Figure 2.12. The mechanism has seven movement degrees of freedom; therefore the laser can reach every points and surfaces within the examining space. The apparatus radiate a 65 mm width laser beam, Figure 2.13.



Figure 2.12 The arrangement of 3D laser scanner

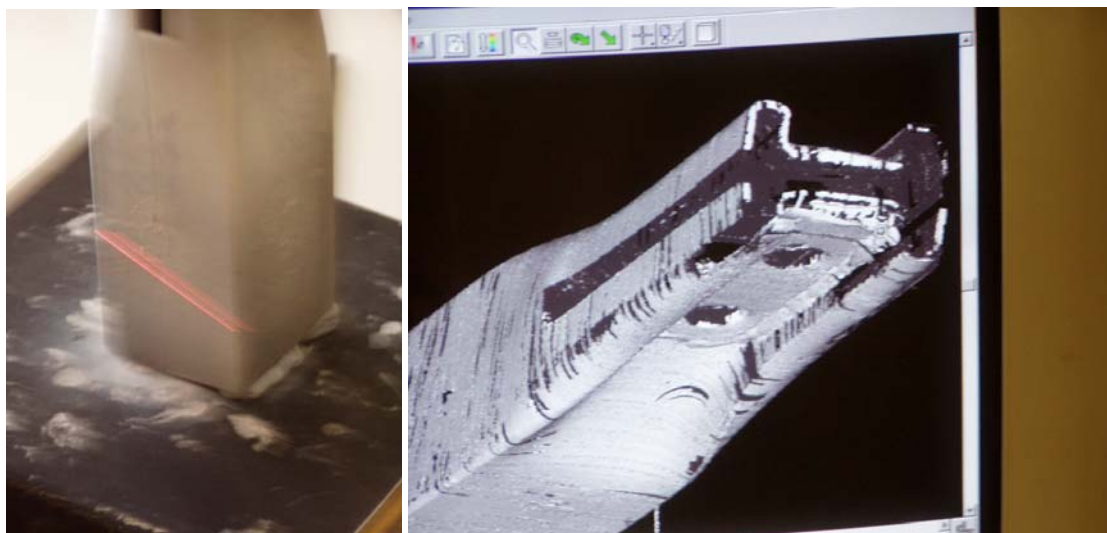


Figure 2.13 The laser beam and the control monitor

With this laser beam the surfaces of the examined object are scanned and the 3D coordinates of the surfaces' nodes are measured in a basic coordinate system. The sensitivity of the apparatus is 0,2 mm, which is enough for our examination.

The first step is to paint the examined objects with a special liquid, which reflect the laser beam from the surfaces. Then the operator scans the surfaces in more rounds and checks the scanned results live on the monitor of the apparatus. Thus the operator can check the missing surface parts. The final result of the scanning is a huge amount of data, which contains the three coordinates of millions of surface points. With the help of post-processing computer software the scanned 3D picture of the object can be shown and can be saved in different extension for further application.

The digitalized picture now can be compared to the result of the numerical calculation and can be verify the suitability of the numerical model. On the Figure 2.12 and Figure 2.13 the apparatus and the control monitor are shown under work. The comparison of the real bar, the numerical model and the scanned bar are shown on Figure 2.14. Of course this picture shows just a general overview about the comparison.

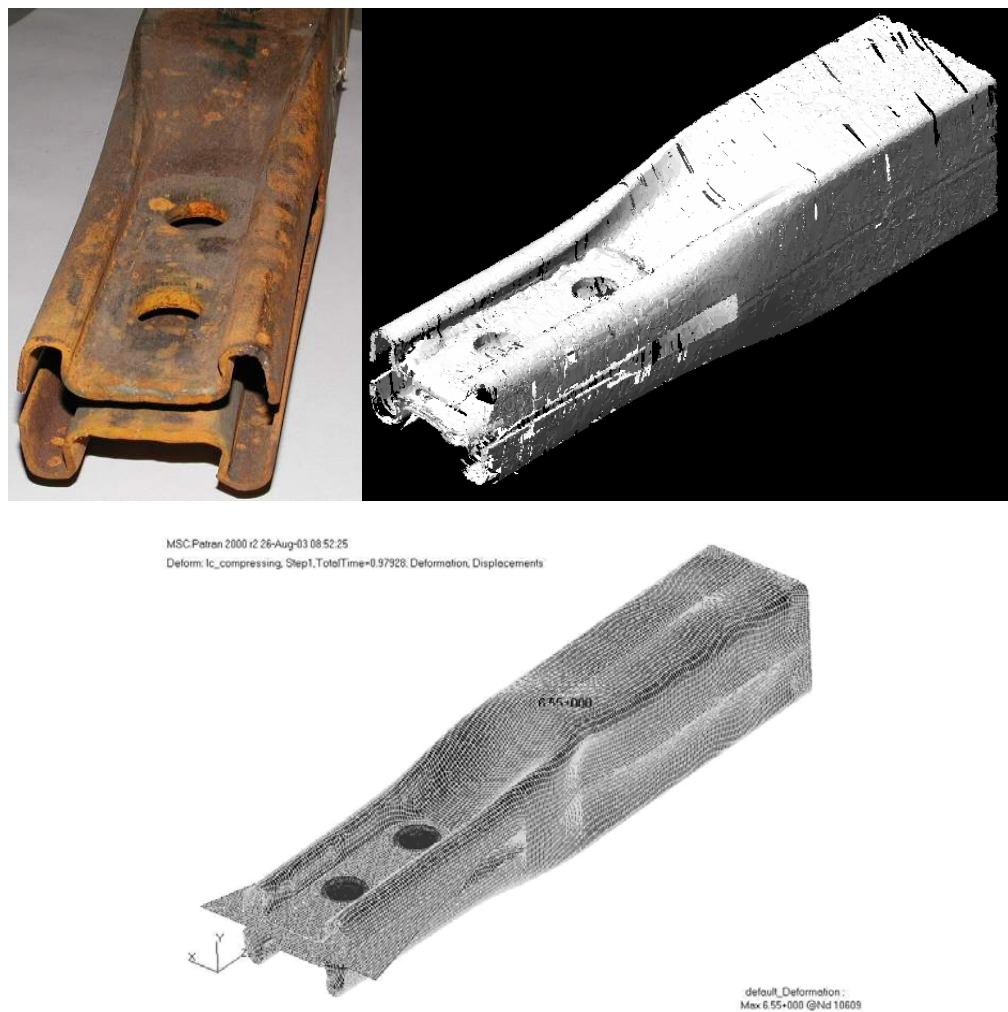


Figure 2.14 The real bar, the result of 3D laser beam scanning and the numerical model of the bar

The real comparison can be made if the numerical model and the digitalized object are copied onto each other. This comparison was made at WOCO Gumitech Co., Budapest. I had the possibility to use ABAQUS finite element program at Gumitech, and they gave help in the processing of digitalized data. The best solution could be to copy all the scanned nodes into the numerical finite element mesh. Because of the millions of scanned nodes and the limited computer memory capacity it was not possible to handle the whole model. Just a part of the scanned model was comparable to the FEM model. Figure 2.15 shows some model sections from the original hollow squared section, through the deformed section, till the end section of the bar.

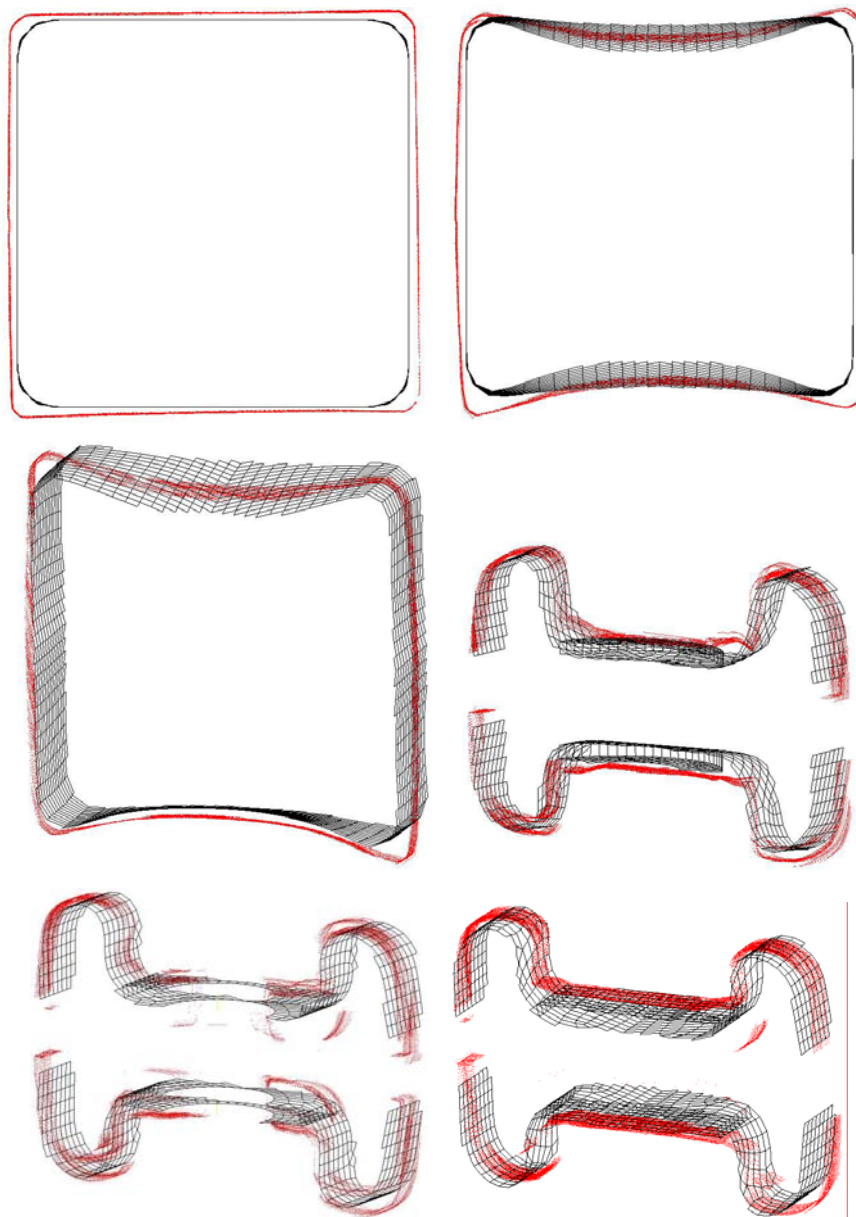


Figure 2.15 The comparison of FEM model and the result of 3D scanning

The mass of scanned nodes must be cleaned and thinned, because there were nodes in the model from the examining table, and due to the repeated scanning rounds lots of nodes were duplicated. The inner grey surface is the FEM model; the outer red points are the scanned nodes. The FEM model contains 4-node shell elements, what represent the midplane of the bar. The laser can see the real surfaces of the real bar. That is the difference between the two models, half-half plate thickness at both sides. It is interesting to see that the laser can ‘look into’ through the holes, and there are scanned nodes from the inner surfaces, too.

Until now mainly industrial designers used the 3D laser scanner at MTA SZTAKI, but I was the first civil engineer there, who used the scanner in structural engineering work.

2.2. Results of the numerical analysis of compressed bars

The numerical analyses of individually compressed diagonal bars are the second level of my work. These numerical analyses were performed by ABAQUS version 6.3-2 finite element program and for pre- and post-processing the MSC Patran 2000 r2 program was applied.

The shaping process of the bar ends, the numerical analysis of the formation process – where the quartered model of the bar is presented –, and the verification of the resulted FEM mesh is described above.

I applied the resulted shape of the quarter bar model of the “flattening” process. At the first calculations, I loaded the quartered model by a concentrated normal force. The ABAQUS run the load case, found the equilibrium state, but the behaviour of the quarter model was unreal. It took very large deformations, which could not occur in a real hollow squared cross-section.

The buckling shape of the compressed bar was not totally symmetrical in the experiment. Therefore I had to model the whole flattened cross-section instead of the quarter of the hollow section. Reflecting twice the quartered model I generated the whole section model and put the welded reinforcing plate at the flattened part completed the model. A thick gusset plate was applied and the compression load acted on it. The un-flattened end of the bar was fully supported; the gusset plate was guided providing the perfect compression loading. The bar contains 4-node shell elements, as was in flattening process (element type S4R of the ABAQUS program library [20]). The gusset plate is

modelled shell elements, too. The bolts were modelled by bar elements (element type B31) and special elements, multi point constant (element type MPC) applied to avoid the deformation of the holes of bolts [20].

The numerical model of the flattened bar was ready for loading. The first investigated load case was the concentrated normal load. Several attempts were calculated while the model worked as I expected. I got internal errors, failure of the bolts and the gusset plate because of initial stiffness problems, termination of calculation too early because of small external load, etc. The calculations were done at WOCO Gumitech Ltd., Budapest. They gave me extensive help, computer capacity and time for performing the calculations. It took lots of time the calibration and modification of the numerical model. I had the possibility to use Patran program for the pre- and post-processing the data of ABAQUS with a temporary login account. Thus I was able to evaluate the numerical results at home and just at the Gumitech.

The Figure 2.16 shows the resulted phases of compression process and the buckling shape of the bar. The numerical analyses were performed assuming perfectly centrally loaded bars. The bar was created by reflection and the applied load was concentrated, thus the deformation state remained symmetrical during the collapse.

The reaction force [kN] – displacement [mm] curve of the process obtained from numerical analysis is on Figure 2.17. The 'ABAQUS' curve shows the ABAQUS result of the compression process. This curve is modified by the distance according to the difference between the diameter of the whole and the diameter of the bolts. The maximum compression load is $F = 122.7$ kN. 16 bars were compressed in the individual experiments. The Figure 2.17 shows 12 load-displacement curves from the 16 experiments. The “V” mark in the curves shows the connection slipping during the experiments. The average load bearing capacity of the bars is $F_{av} = 112$ kN. The ABAQUS model follows the post buckling behaviour, too. The numerical model of the whole sectioned bar is applicable for parametric examinations with such load cases, which were not performed in the structural laboratory.

Applying the bar model different load cases are examined by ABAQUS to see the behaviour of these truss element and to find that load case, which caused the local buckling failure in the full-scale test.

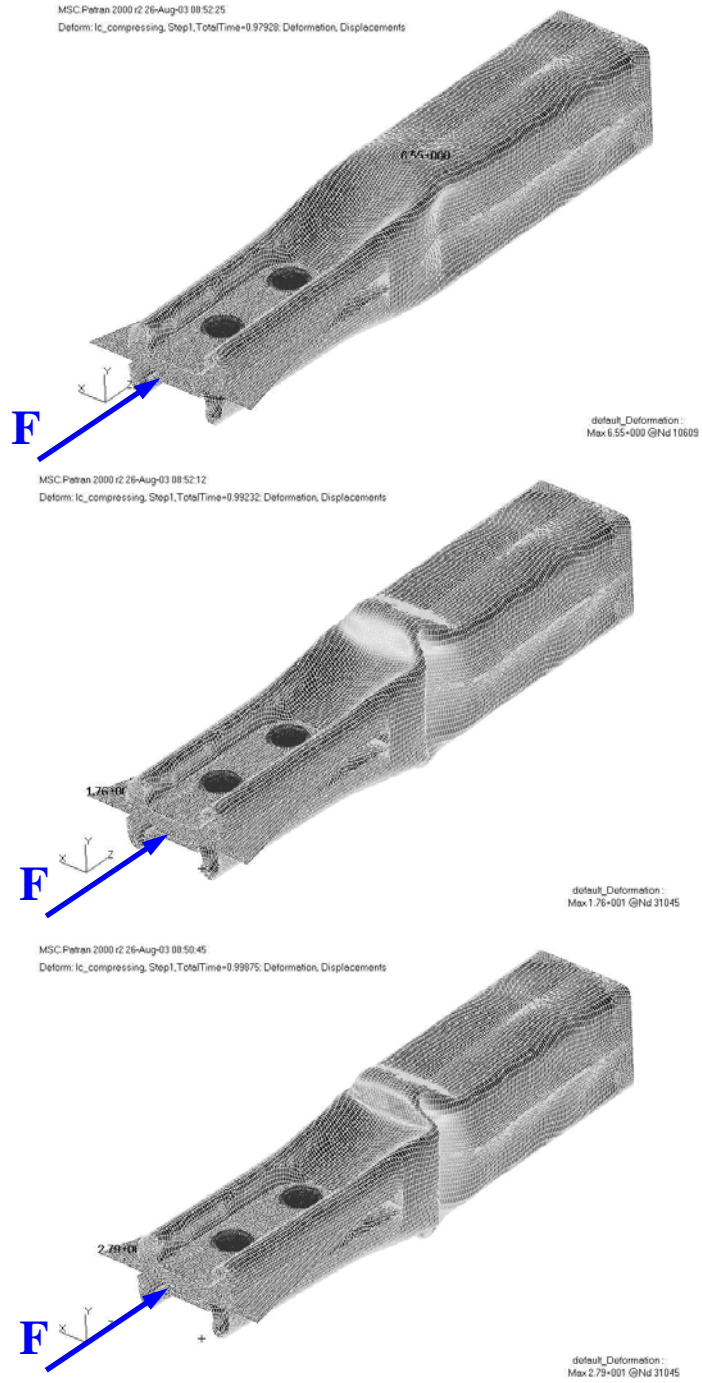


Figure 2.16 Result of the compression.

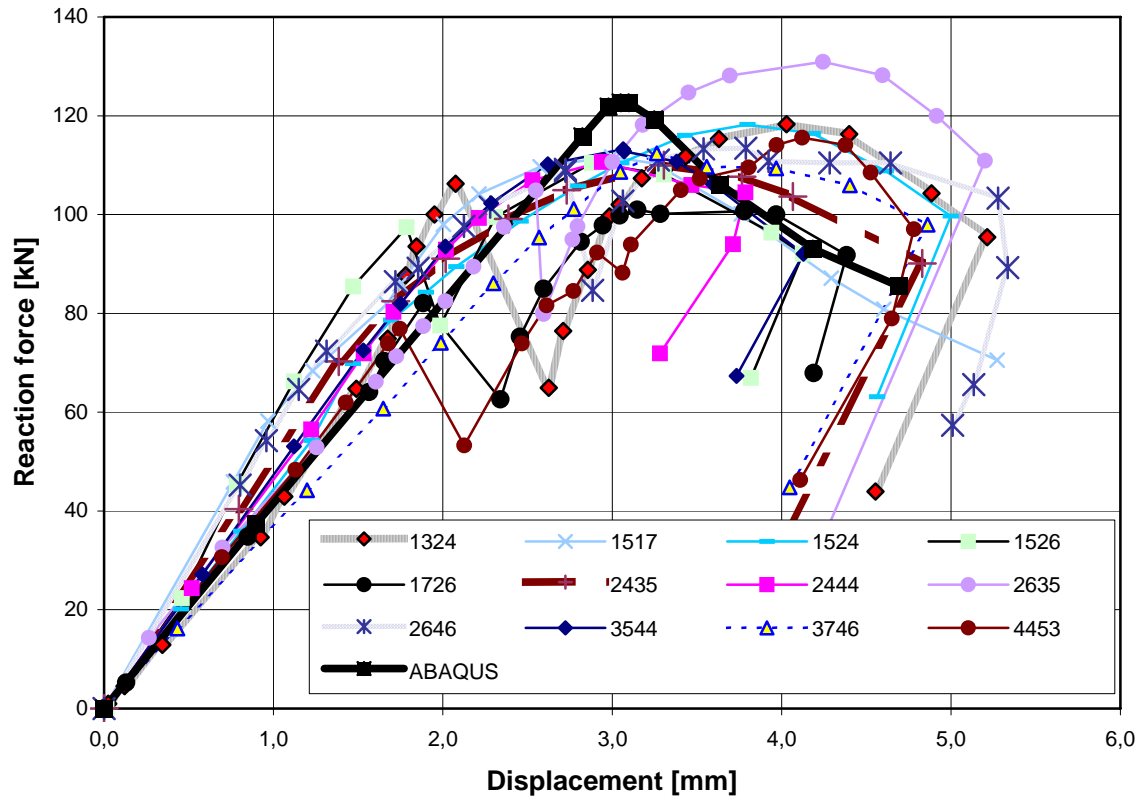


Figure 2.17: The reaction force [kN] displacement [mm] curve of the process.

Pure bending moment M_x . In the following load cases bending moments and normal forces are applied. A pair of concentrated loads models the bending moments on the bars. I applied a vertical joint plate at the end of the bar, which plate is welded to the gusset plate. The second load case after the pure compression is the pure bending moment around the horizontal x-axis M_x . The flowchart of the buckling failure is on the Figure 2.18. The applied loads were $F = 16$ kN, thus the bending moment was $M_x = 16$ kNcm. The moment bearing capacity of this bar is $M_{x,max} = 0.999 \times 16 = 15.89$ kNcm.

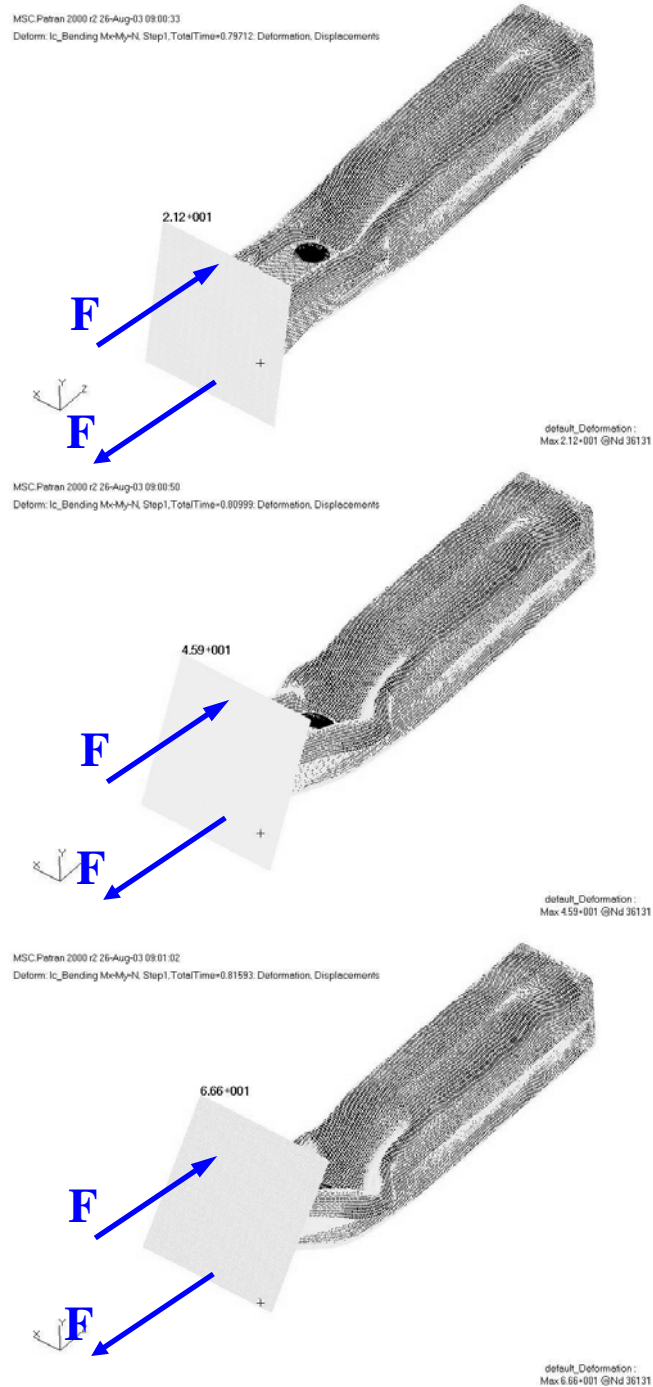


Figure 2.18 Numerical analysis of the bending moment M_x .

Pure bending moment M_y . The third calculated load case is pure bending moment around the vertical y -axis M_y . A pair of concentrated loads was applied at the endplate of the bar again and the flowchart of the buckling failure is on the Figure 2.19. The applied loads were $F = 30$ kN, thus the bending moment was $M_y = 30$ kNcm. The moment bearing

capacity of this bar is $M_{y,max} = 0.692 \times 30 = 20.76$ kNcm. The flattened section is stronger in this load case, the M_y moment capacity is higher than M_x .

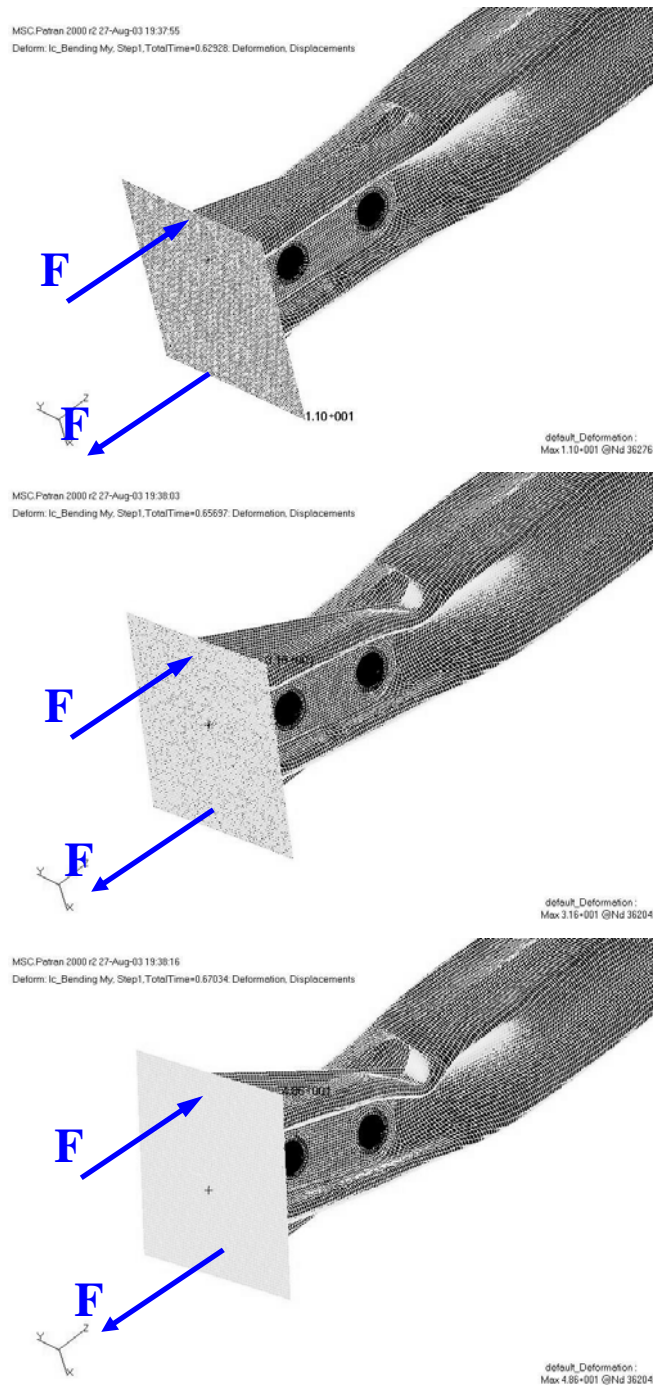


Figure 2.19 Numerical analysis of the bending moment M_y .

Normal force and two moments M_x and M_y . The next examined load case is a concentrated load was applied eccentrically in both x and y direction. This load causes normal force N and two bending moments M_x and M_y in the bar. The flowchart of the buckling failure is on the Figure 2.20. The applied load was $F = 50$ kN, thus the bending moments were $M_x = M_y = 25$ kNcm. The calculated load factor is 0.4, that means at the final state, at failure the bar has $N = 0.4 \times 50 = 20$ kN normal load and $M_x = M_y = 0.4 \times 25 = 10$ kNcm bending moments. The buckling occurred on the nearest leg of bar to the applied load. This load case corresponds to the normal force with large eccentricity.

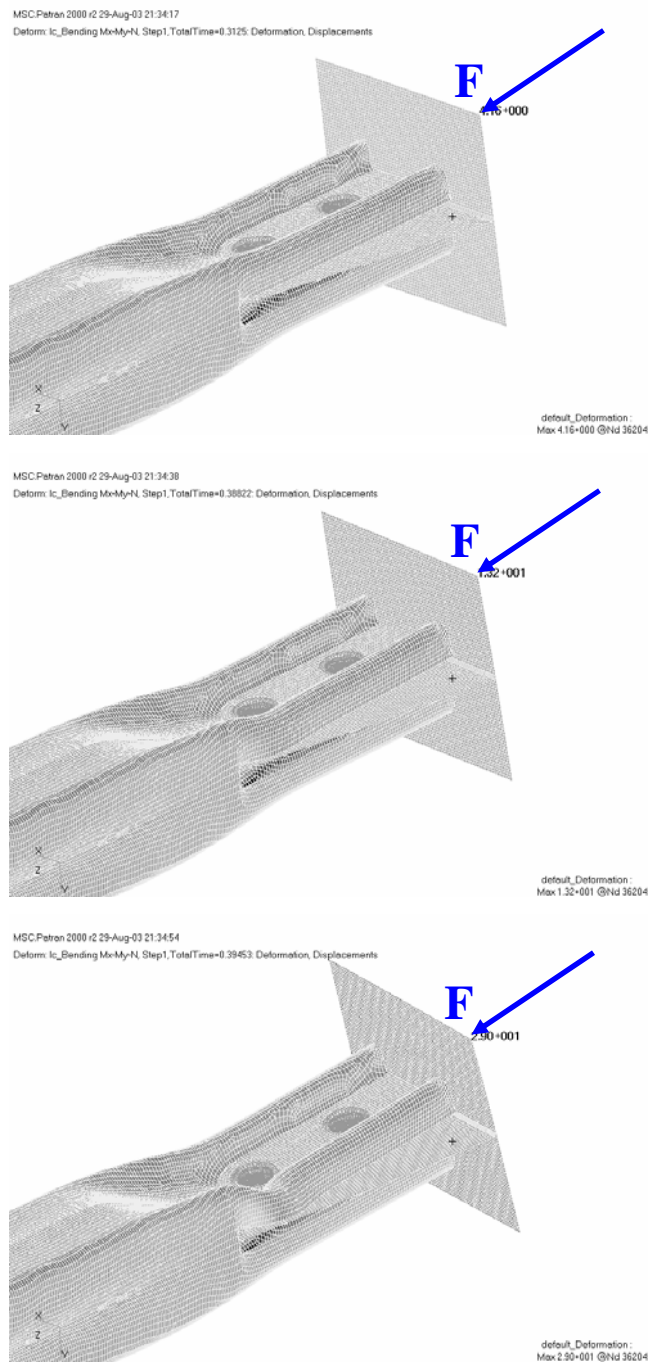


Figure 2.20: Numerical analysis of load with large eccentricity.

Pure torsional moment M_t . The next examined load case is not a typical load case in trusses. Pure torsional moment M_t around the bar axis 'z' was applied by 4 concentrated loads in the plane of endplate of the bar. The flowchart of the torsion failure is on the Figure 2.21. The intensity of loads is $F = 20$ kN. The limit torsional moment at the limit deformation is $M_t = 0.175 \times 4 \times 20 \times 5 = 70$ kNcm. Generally this type of load does not exist in a space truss during its normal life. But it is interesting to see how this rectangular hollow section works under torsional moment. The deformations remained in the elastic range and the flattened part of the bar rotated.

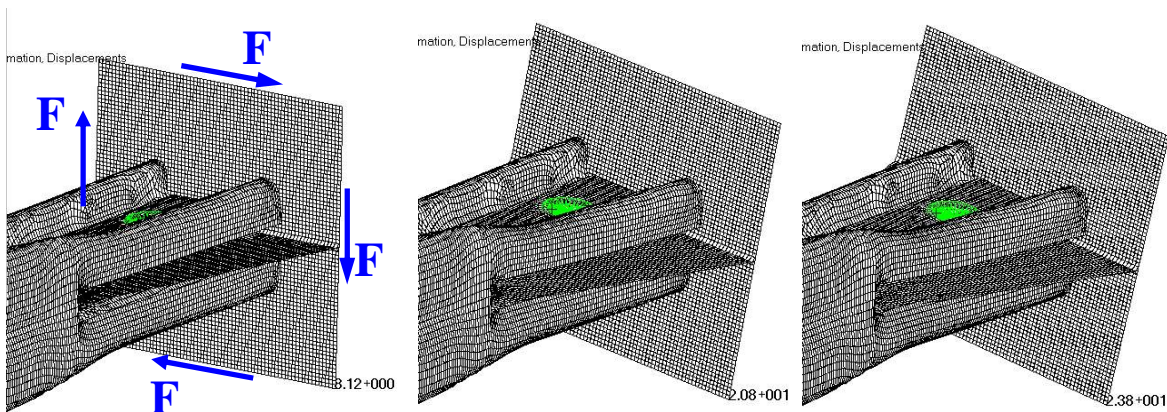


Figure 2.21: Numerical analysis of the torsional moment M_t .

Normal force with small eccentricity. The next analysis is performed applying compression force with small eccentricity. Small eccentricity it is the tenth of the width of the bar. The load case again combined load case a compression force with bending moment. The eccentricity applied in the direction of x-axis. The flowchart of the buckling failure is on the Figure 2.22. The applied load was $F = 108$ kN, thus the bending moment was $M_y = 65.8$ kNcm. The calculated load factor was 0.727, that means at the final state, the bar has $N = 0.727 \times 108 = 78.52$ kN normal load and $M_y = 0.727 \times 65.8 = 47.84$ kNcm bending moment.

The buckling is occurred next to the deformed end of the bar, as is in the full-scale space-truss specimen, see Figure 2.22. This load case prescribes the behaviour of the buckled diagonals. That means at real space-truss connections of the bars at the joints are not concentric. Bending moments arise at connections and the semi-rigid characteristic of bar connections can work with them. The buckled diagonals of the full-scale test and the digitalized model by the 3D scanner are on the Figure 2.23.

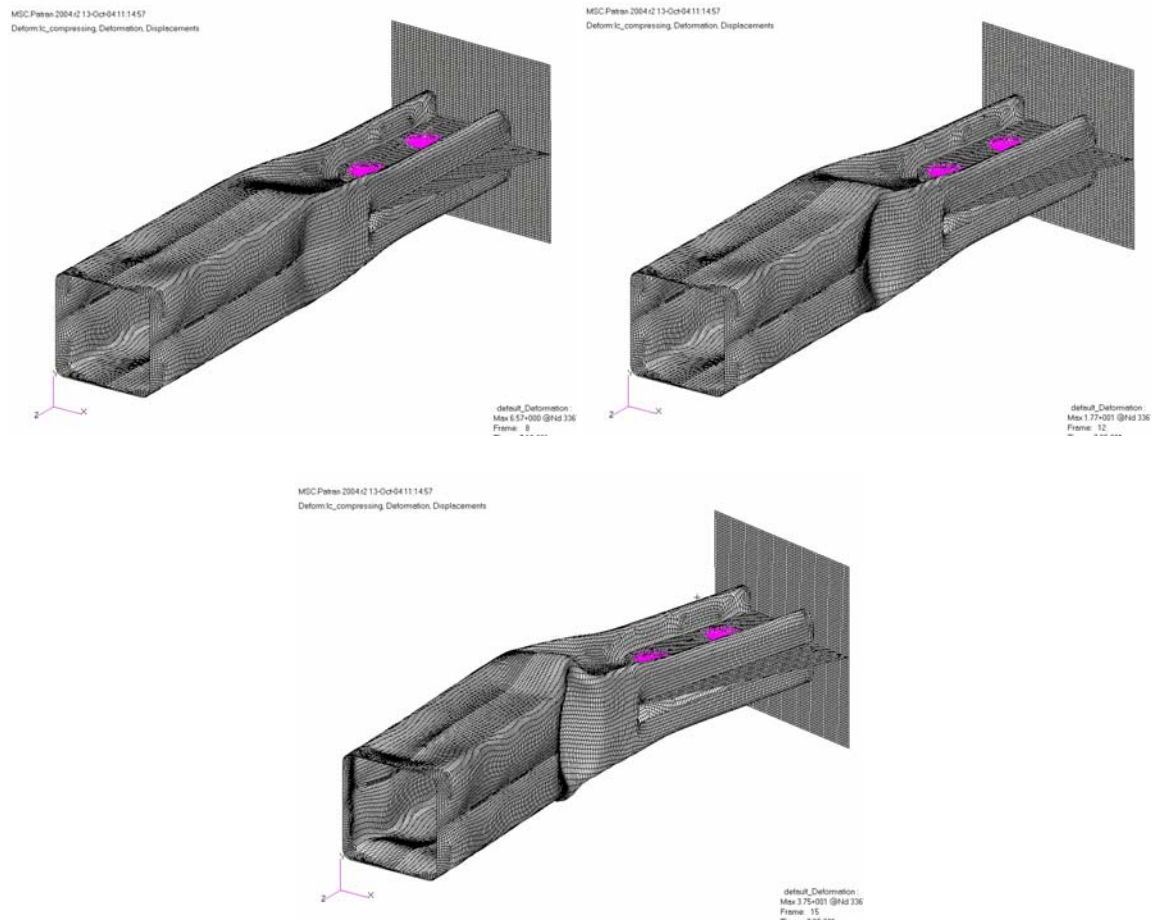


Figure 2.22 Numerical analysis of the compression with small eccentricity.

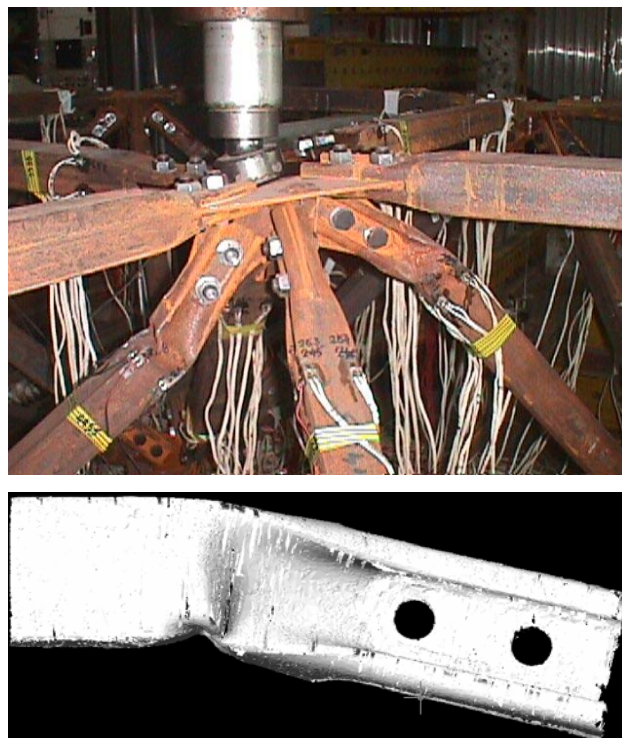


Figure 2.23 The results of the full-scale test and the 3D scanner

2.3. Results of the numerical analysis of space-truss segment

AxisVM finite element programs were used for the numerical analysis of the whole space-truss segment. Dr. Jenő Balogh gave me help in the calculation by the latest version of Axis program. He works in Denver, Colorado, USA in the development team of Axis program. He was able to try and apply such theories and calculation techniques, which are still not in the commercial versions of Axis.

The Figure 2.24 shows the geometry of the structure in the Axis. All 60×60×2 members were modelled as truss bars, with $A = 4.59 \text{ cm}^2$ and $L = 1.2 \text{ m}$.

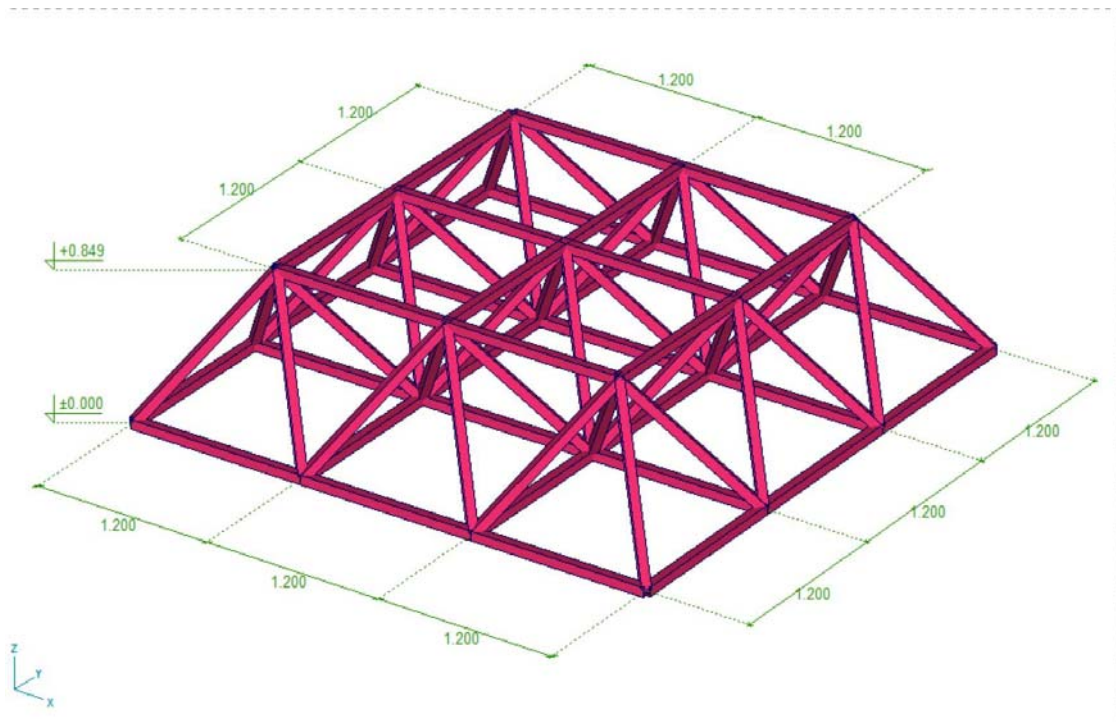


Figure 2.24 The geometry of the structure

The adopted material properties, the stress-strain diagrams were applied as follows. Initial modulus of elasticity: $E = 20\,000 \text{ kN/cm}^2$. This was the value that provided the best agreement to the measured global response of the structure in the elastic domain (also is the value used in US for steel). Different diagrams were applied for the members in compression and for the members in tension. The stress-strain curves are on Figure 2.25. The curves are:

Members in compression:		Members in tension:	
Strain	Stress [kN/cm ²]	Strain	Stress [kN/cm ²]
0	0	0	0
0,000937	18,74	0,001175	23,5
0,001525	21,79	0,012930	27,5
0,001976	24,03		
0,002325	23,73		
0,003680	19,98		

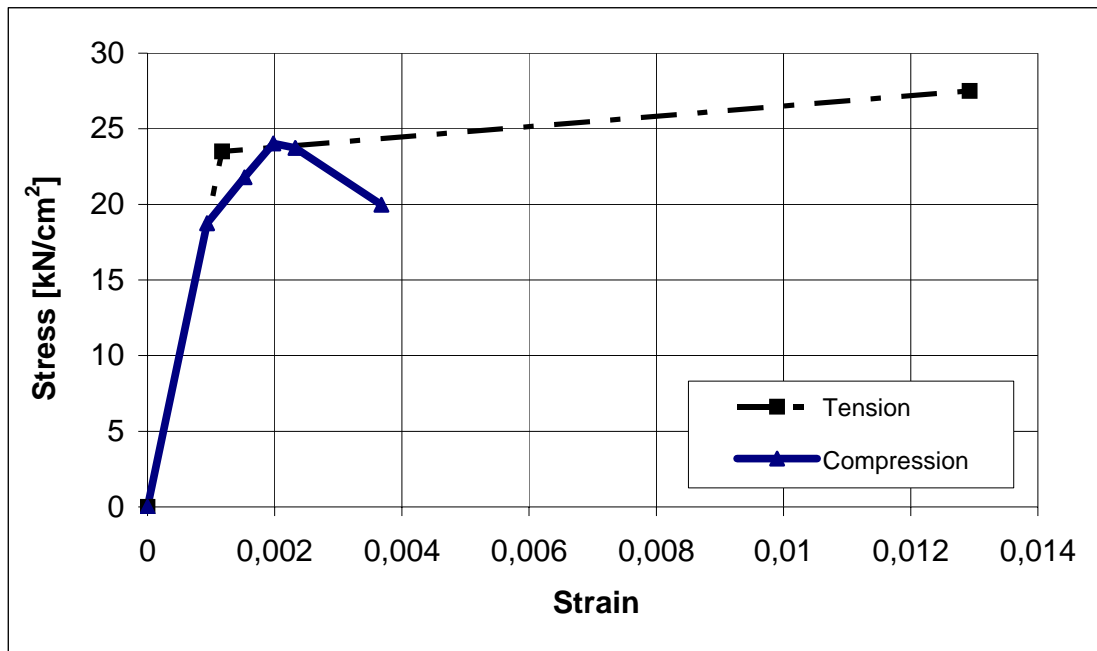


Figure 2.25 The stress-strain curves

In the model the top central node was loaded with a 100 kN reference load. All load parameters (Thp – see Figure 2.26) apply to this reference value.

To better control of the solution process a displacement control was applied to the Central Node, Direction – Z with a total of 200 increments that simulated loading and unloading (static) cycles as follows:

Total increment	Displacement / increment [m]
0	0
30	-1.200 E-02
40	-0.160 E-02
70	-1.350 E-02
80	-0.280 E-02
110	-1.500 E-02
120	-0.500 E-02
150	-1.575 E-02
160	-0.750 E-02
190	-1.660 E-02
200	-1.000 E-02

The loading scenario was conceived so the centre point deflection not to exceed approximately 12 mm within a loading cycle, to show the cumulative effect on the load-displacement characteristic of the cycles. Figure 2.26 shows the load factor – displacement

results of the loading scenario. The overall behaviour of the numerical model is very similar to the experimental results.

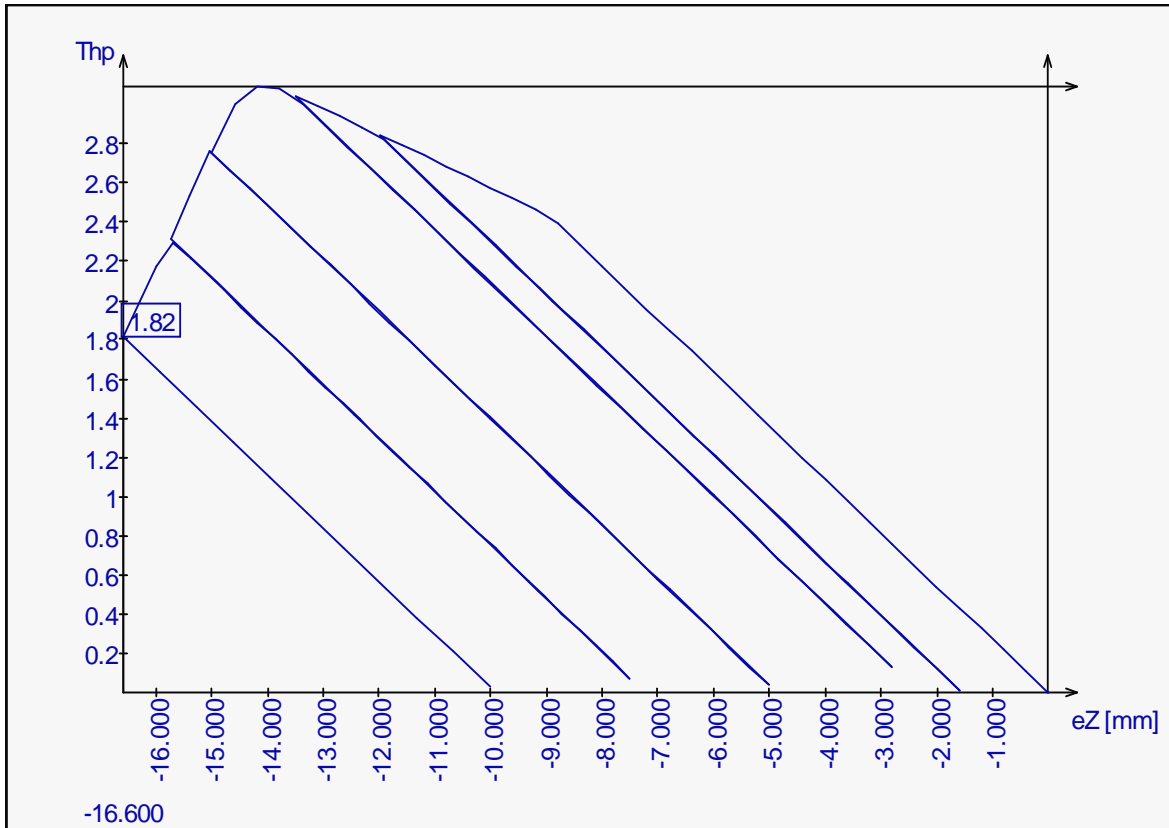


Figure 2.26 Load factor – Displacement diagram of the center node *

* Multiply the Load Paramater (Thp) by 100 kN (reference load) to obtain the corresponding load level.

The maximum load is $F = 308.7$ kN at $\delta = 14.2$ mm deflection and the final load is $F = 182$ kN at $\delta = 16.6$ mm. Every bar has constant cross-section in the model. The deformed end of the bar was taken into account by modifying the supporting behaviour of bars at the connections. The post-buckling range of the diagram above follows the experimental result very well.

As I mentioned before two AxisVM models were done. The second model was created with the commercial version of Axis VM 8 finite element program. In this model the changing of the cross-sections of bars was modelled with a smaller hollow squared section at the ends of the bars, see Figure 2.27. The smaller cross-section is $60 \times 15 \times 1.5$. Another possibility is applied in Axis; I can define plastic or semi-rigid hinges at the end of bars. First I create a bar model with changing cross-section at the ends, and find an appropriate model for the compressed bars. This model contains different cross-sections at the ends and in middle of the bar, and I defined plastic hinges at the end of the bar (see Figure 2.28).

This bar model has the same behaviour, as the individually compressed bars. This bar model was applied in the truss model. Not all of the bars were changed to the new bar, just those bars, which are near to the loaded top central joint and therefore has significant normal forces inside. The latest version of this truss model is on Figure 2.29. The load bearing capacity is $F = 231$ kN, which is approximately the same as in the experiment was.

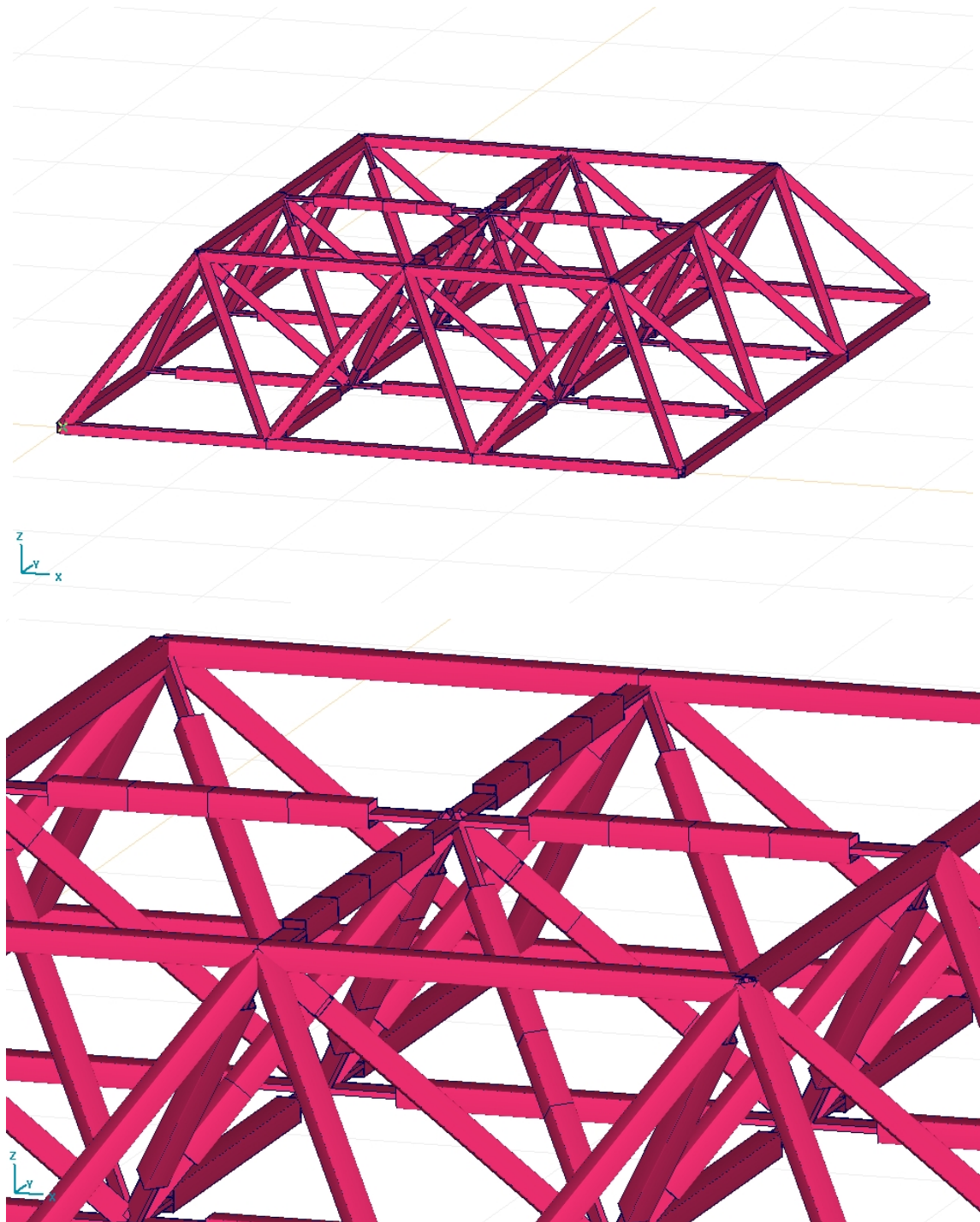


Figure 2.27 Truss model in Axis VM 8 version

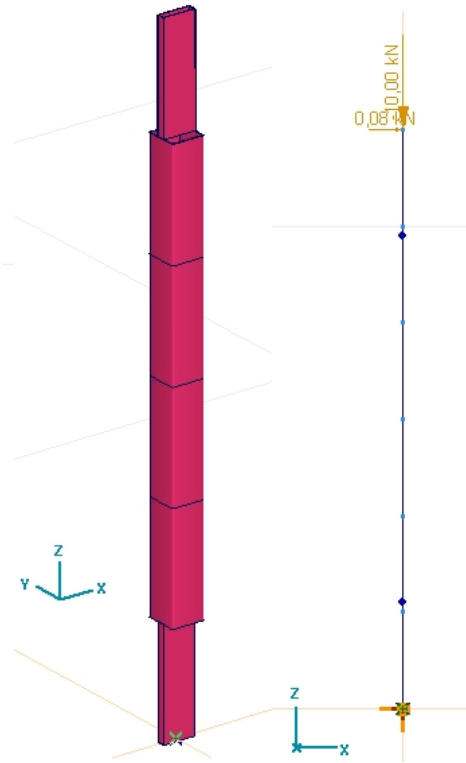


Figure 2.28 Bar model with plastic hinges in Axis VM 8 version

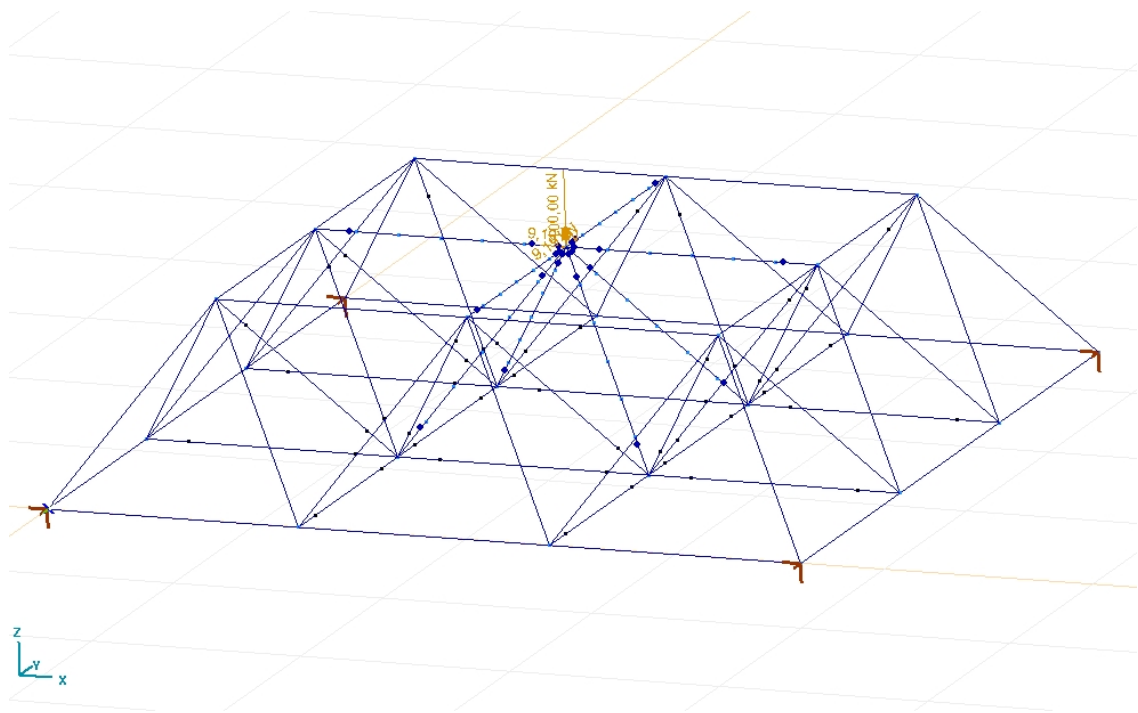


Figure 2.29 Truss model with plastic hinges in Axis VM 8 version

2.4. The full-scale tests on the space-truss specimen

An N-type segment of TOP-SYSTEM space-truss was examined in the Structural Laboratory of the BUTE Department of Structural Engineering. The N-type (normal, standard) system means that the upper and the lower layer grids are rectangular, and the bars are parallel with the supporting axes. The two parallel bar layers are connected by diagonal bars. The specimen has 3×3 lower layer grid and 2×2 upper layer grid, the theoretical length of the grid bars and diagonals is 1200 mm (Figure 2.30). The specimen contains 25 joints, 72 bars and the theoretical height of the specimen is 849 mm.

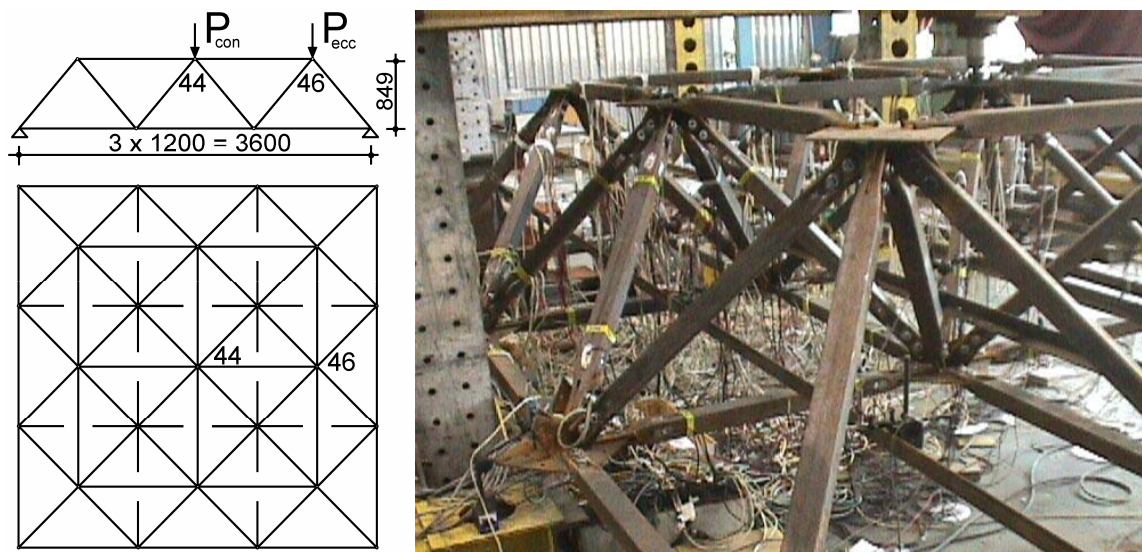


Figure 2.30 The examined space-truss roof-system segment

The bars are 60×60×2 mm cold-formed hollow squared sections, produced by DUNAFERR. The cold-formed hollow squared sections are split and pressed at both end and reinforced by welded plates to ensure the sufficient connection. At every joint eight bars are connected to the special welded joint plate by 2 × M16 high-strength pre-stressed bolts, which bolts were pre-stressed by acting torsional moment 250 Nm.

The roof specimen is simply supported at the four lower corners. The acting load is vertical concentrated joint load on the top joints. Hydraulic jack is applied for loading, which is fixed on the strong supporting frame over the specimen. At every joint, excluding the four supporting joints, inductive transducers measured the vertical deflections. It is very important to calibrate and verify transducers before the experiments. Strain gauges are applied for measuring the strains in the selected bars, and the normal forces in the bars are

calculated from the measured strains. Just the quarter of the bars have strain gauges. Four-four strain gauges are in the mainly tensioned members and eight-eight strain gauges are in the mainly compressed members at each end of the bars. Totally 352 strain gauges are applied during the experiments together with the 21 inductive transducers, which measured the deflection of the joints (Figure 2.31). The load is measured with two load cells, thus at every load steps 375 measurements are done and saved. Due to the capacity of the measuring computer the data processing took 4-5 minutes at the end of every load steps.



Figure 2.31: Inductive transducers and strain gauges in the experiments

Three experiments were done on the specimen. During the first experiment a vertical eccentric load was applied on the top layer joint 46 (P_{ecc} on Figure 2.30) in the linear elastic range. Then vertical concentrated load was applied in the second and third experiments on the top central joint 44 of the structure (P_{con} on Figure 2.30). First in the linear elastic range again until the maximum deflection ($\Delta = L/300$) of the serviceability limit state, finally the specimen was loaded until the collapse. The loading procedures were displacement controlled.

2.4.1. Load case 1: Eccentrically loaded roof in linear elastic range

During the first experiment an eccentric load was applied on the structure on the top layer joint 46 (P_{ecc} on Figure 2.30) in direction $-z$. The load steps during the experiments were 10 kN. The specimen loaded in the "elastic" range. At load level $P_{ecc} = 47$ kN, sudden noise was occurred due to a connection slipping and the load decreased to 42 kN, the deflection increased on the same time. The connection slipping occurred at one of the bolted connections due to the pre-stressing of the bolts. After reaching the maximum applied eccentric load $P_{ecc,max} = 77.01$ kN, the specimen was unloaded in 3 steps. The mark of the connection slipping could be found under the slipped bolts after disassembly of the

whole truss. The connection slipping behaviour was typical during all of the three experiments. The specimen has not got considerable residual deformation after unloading, except the deformation due to the slipping. Figure 2.32 shows the load-deflection curves of the top central joint (44) and the loaded joint (46). The connection slipping causes shift of the load-deflection curve. Black circles on the following diagrams sign the connection slipping. The unloading path is linear elastic and the remaining deflection, $\delta = 1.1$ mm is mainly the result of connection slipping.

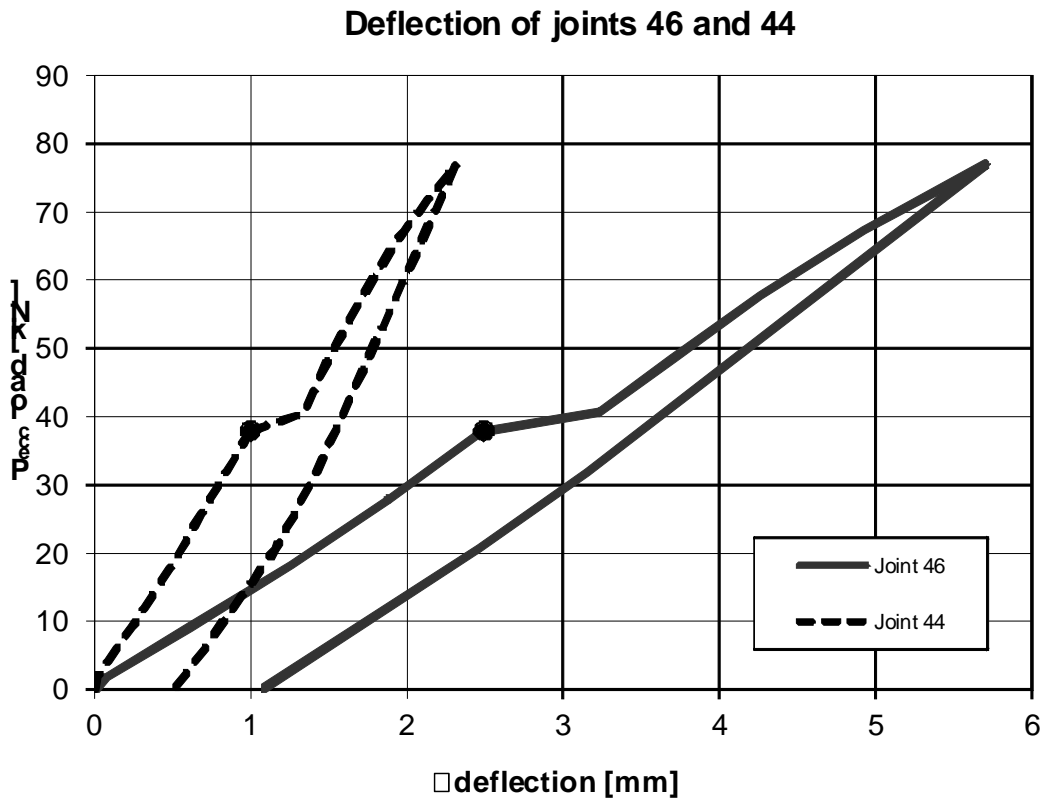


Figure 2.32 The load-deflection curves of the main joints at load case 1

Figure 2.33 shows the vertical deflections of the joints at the maximum eccentric load. The deflections were measured by inductive transducers. The thick line is the original truss without loading; the thin line shows the deflected truss, which was drawn onto the vertical deflections. The magnification of the deflections is 25:1. The steel-truss shows normal linear elastic behaviour under this load case.

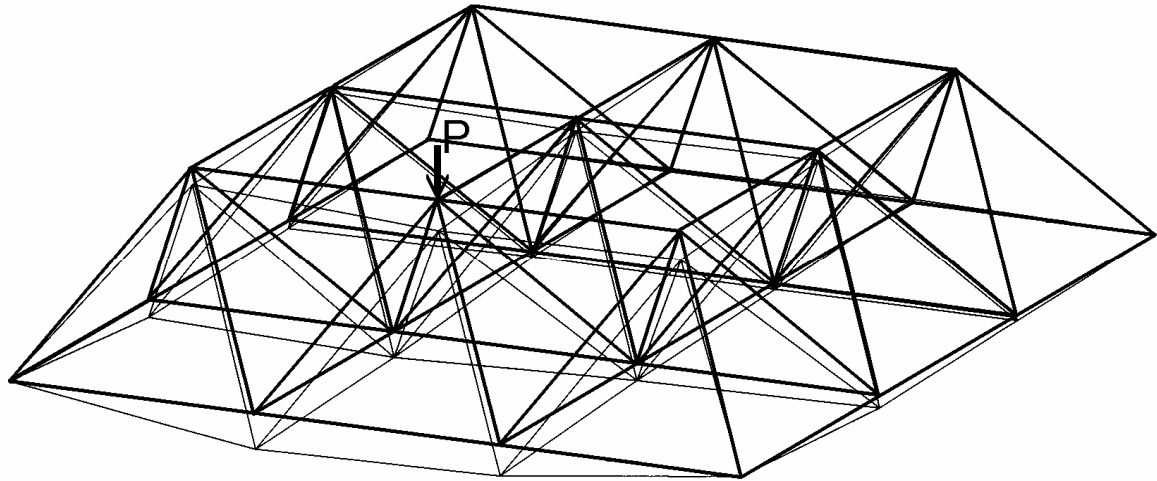


Figure 2.33 Deflections of joints at load case 1

2.4.2. Load case 2: Concentrically loaded roof in "elastic" range

The hydraulic jack loaded the top central joint (44) of the structure in direction $-z$ in the second experiment (P_{cen} on Figure 2.30). The load was applied until the maximum deflection of the serviceability limit state $\Delta_{max} = L/300 = 12$ mm. The load-deflection curve of the top central joint (44) is on Figure 2.34. The behaviour of the specimen is linear elastic. During the experiment connection slipping has occurred three times at $P_{cen,a} = 115$ kN, $P_{cen,b} = 188$ kN and $P_{cen,c} = 212$ kN, and further two in the last load steps at $P_{cen,d} = 232$ kN and $P_{cen,e} = 237$ kN. The load decreased while at the same time the deflection of the middle joint is increased suddenly due to the connection slipping. During the last load increment the load decreased from 237 kN to 217,9 kN suddenly. After the two noisy bolt slips the specimen was unloaded. The measured maximal load was $P_{cen,max,1} = 231.7$ kN. The maximum deflection before the unloading was $\Delta = 11,8$ mm. Black circles on the following diagrams sign the connection slipping. The specimen has not got considerable residual deflection after unloading, just 4 mm due to the slipping. The whole load cycle and measuring of this experiment took approximately 3 and half hours.

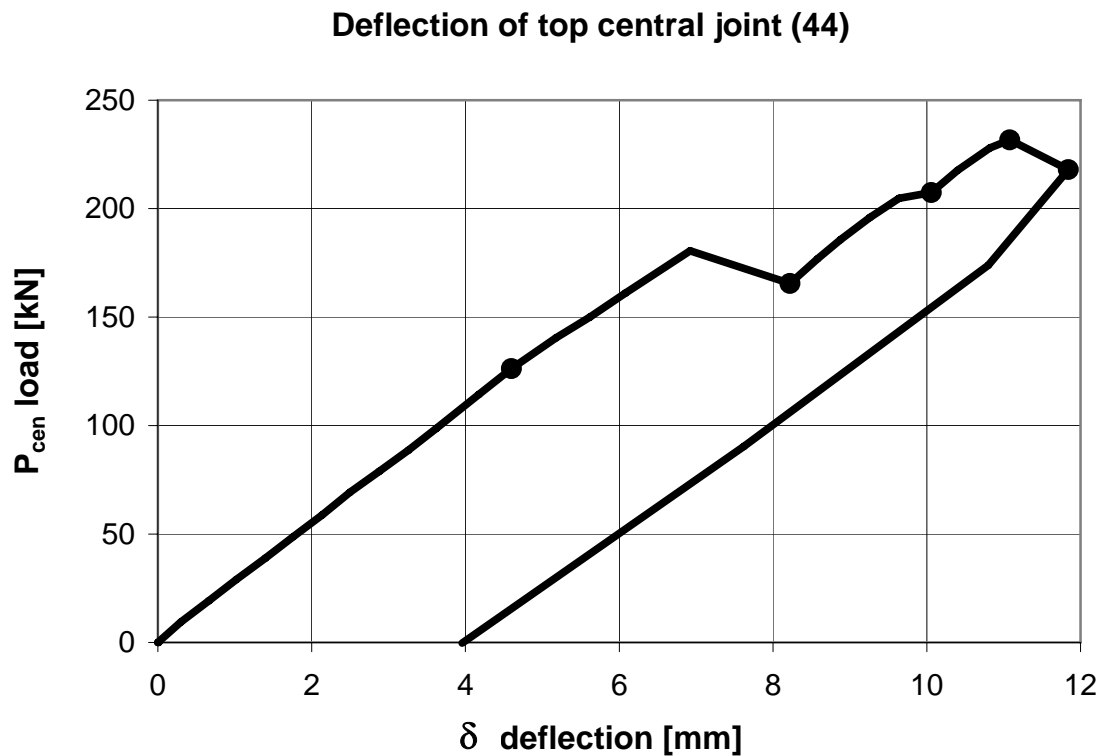


Figure 2.34 The load-deflection curve of the top central joint at load case 2

The connections of the bars into the welded joint plates are theoretically centric and pinned. In the reality neither of them is true. Evaluating the results measured by the strain gauges at a compressed diagonal (Figure 2.35), it can be seen that the bars are under not just normal force but interaction of the bending moments and axial forces. The diagram shows the relation between the measured external force and the normal stresses in the bars. The strain gauges measure strains at the end of the bar changing the electrical resistance inside the gauges. The normal stresses in the bar equal to the strains multiplying with the Young's modulus, $\sigma = E \times \epsilon$. I found that four-four gauges show similar behaviour, and the normal force, bending moments components can be calculate at the end of the bar.

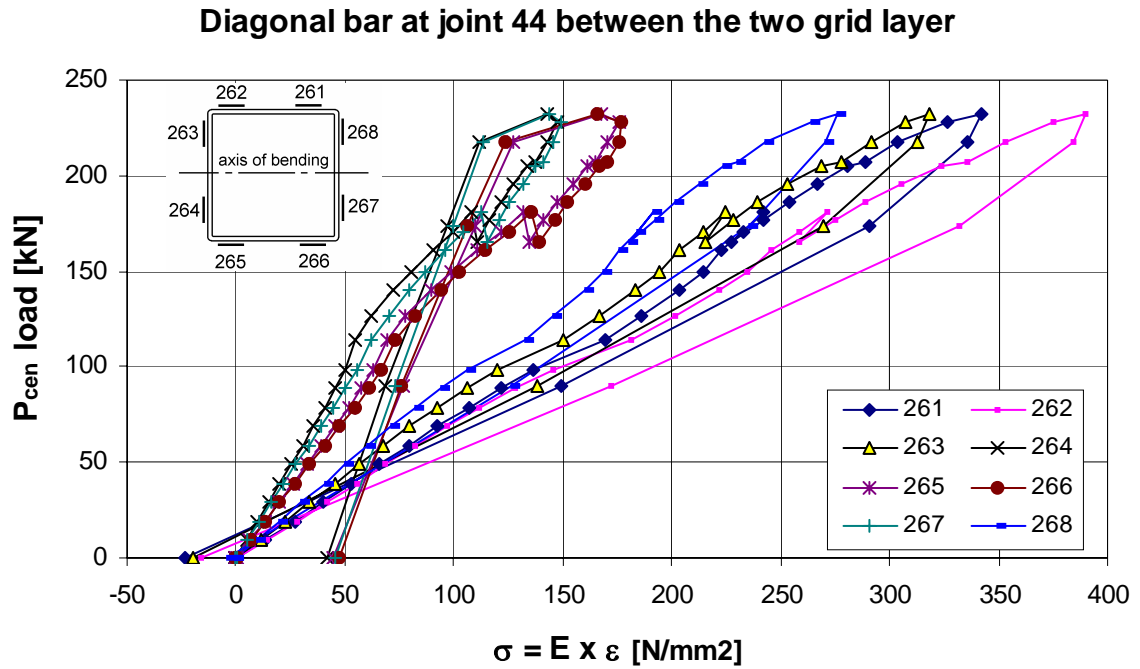


Figure 2.35: Bending moment effect in the compressed diagonal

2.4.3. Load case 3: Failure load of the concentrically loaded roof

During the second experiment the truss reached approximately 237 kN joint load capacity. Connection slipping accompanied the experiment until the maximum load. The third experiment was done to determinate the failure behaviour and the value of the concentrated failure joint load. The possible failure behaviour could be the failure of bars, bolts or welding at the joints. The space-truss behaved in linear elastic way until the load $P_{cen} = 210,15$ kN without any new connection slipping. At the last load step ($P_{cen,max,2} \approx 230$ kN) the space-truss suddenly collapsed (see Figure 2.36). The load was already on the joint and measuring of the gauges and transducers was under work when the collapse has occurred. Because the signs of the load cell were measured at the end of the measurement, measured value of collapse load is not known just an approximate value, which was read from the hydraulic pump. The collapse was due to the local buckling of two opposite diagonals at the loaded top centre joint. The buckling of the hollow squared sections shaped at the end of the diagonals next to the bolted joint (see Figure 2.37).

During the collapse the joint plate suddenly rotated by approximately 6.5° around a horizontal axis, which is perpendicular to the plane of the buckled diagonals. The load

decreased from ~230 kN to 148 kN and the deflection decreased also to 6 mm from 8 mm (measuring just the deflection of the third load case). Figure 2.36 shows the total load-deflection curve of the loaded top central joint in load cases 2 and 3. The dashed line shows the result until serviceability limit state (load case 2) and the continuous line is the failure experiment (load case 3). The behaviour of this examined truss shows a snap back kind of ductility behaviour, which was detected due to the sensitive hydraulic jack, as loading tool. After the collapse I tried to reload the truss again in the post-buckling range, but just the deflection of the truss and the rotation of the loaded joint plate increased. The load bearing capacity decreased slowly (see Figure 2.36).

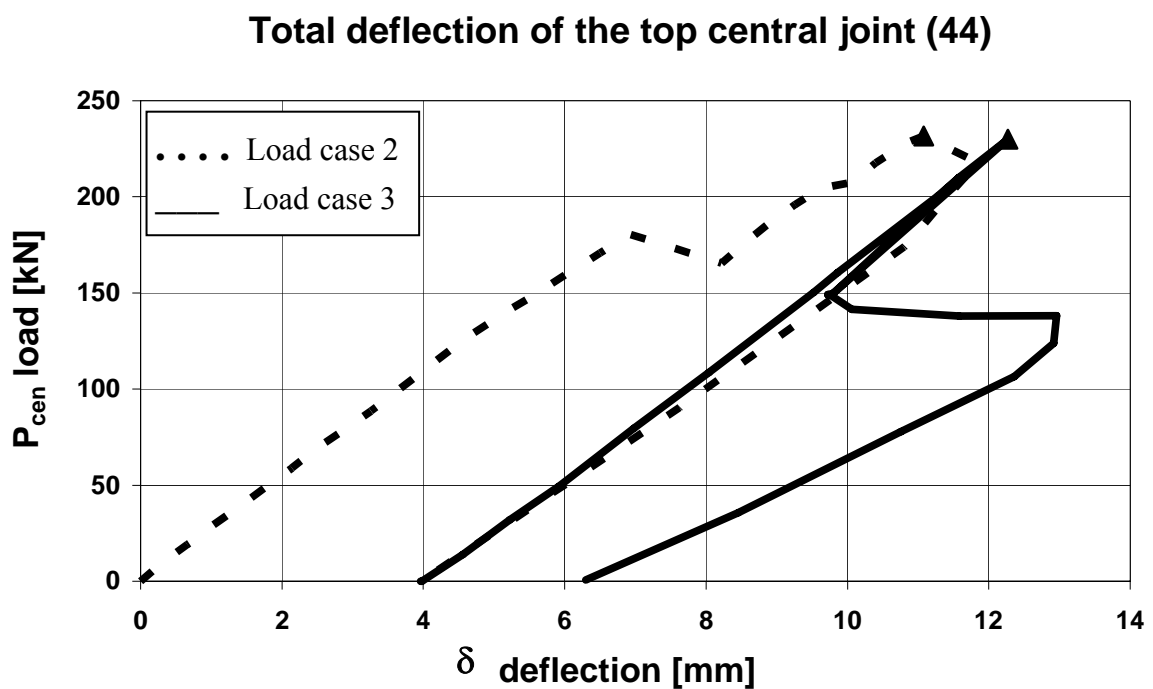


Figure 2.36 The total load deflection curve of the loaded top central joint (44)

The final rotation of the loaded joint plate before unloading was approximately 11.3°. The experiment at this moment is going to be dangerous because the steel ball, which helps to apply concentrated load on the joint, was going to be in dangerous position. The unloading behaviour of the specimen was again linear elastic. The maximum load of the experiment was higher by 19 % than the given load carrying capacity of $F_{d,[TOP-SYSTEM]} = 193,6$ kN. The total remaining deflection at the top central joint after the experiments is 6.3 mm.

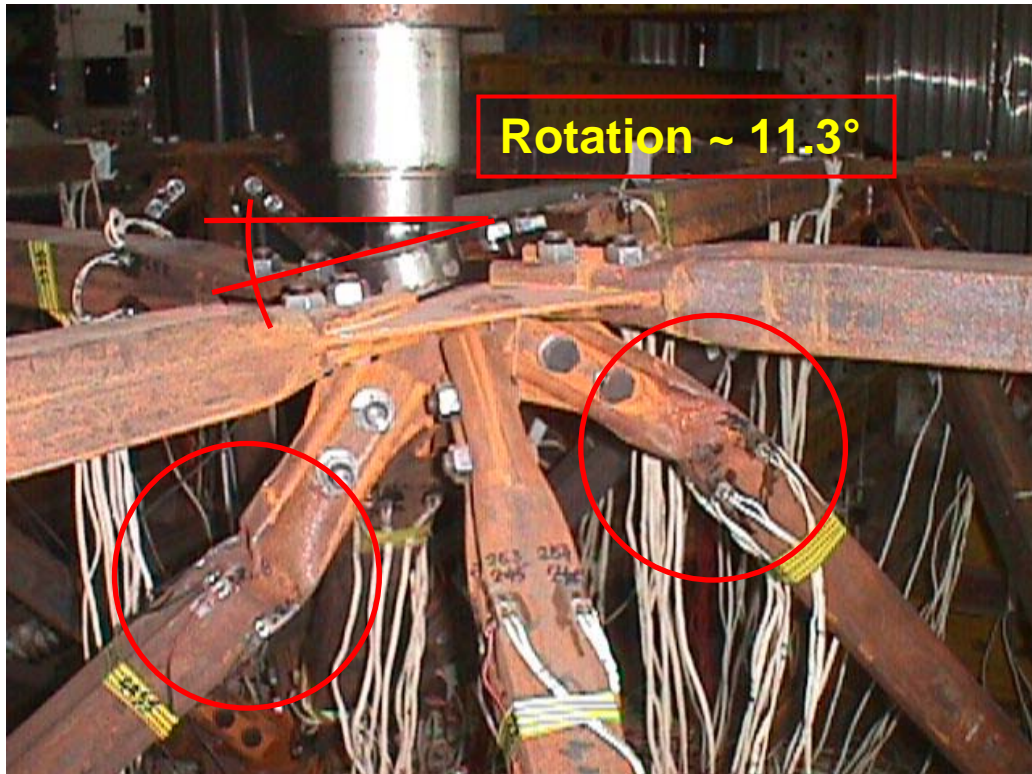


Figure 2.37 The buckled opposite diagonals and the rotation of the joint plate at the top central joint (44)

Evaluating the measured values of strain gauges semi-rigid behaviour can be shown at the bolted connections of the horizontal bars and the diagonals. This behaviour can be demonstrated, if we separate the axial force, bending and torsion moment components of the internal forces. The bending moment-external load curves will describe the semi-rigid behaviour. The following figures show the bending moment components around the two main axes (M_y and M_z) in the bars connected to joint 44 during the third experiment. The bending moment around the horizontal axis, M_y , described by the continuous lines, the bending moment around the vertical axis, M_z , described by the dashed lines. Three different behaviours are shown on the following diagrams.

Figure 2.38 shows the bending moment-external load diagrams of the two opposite buckled diagonals. When the plate buckling occurred, the strain gauges reached the measuring limit and have broken; therefore the diagrams show just the loading path until buckling. On the diagrams it could be seen that bending moment components are developing from the beginning of the loading procedure interacting with axial force.

Figure 2.39 shows the bending moment-external load diagrams of the other two non-buckled diagonals connecting to the loaded joint. The behaviour of these two diagonals is

the same as the buckled diagonals until the maximum load, so there are bending moments from the beginning. After the collapse the bending moments suddenly increased, then due to the unloading, the moment components decreasing. Due to the rotation of the joint plate the signs of the M_y components are opposite. The absolute values of the moment increments are same.

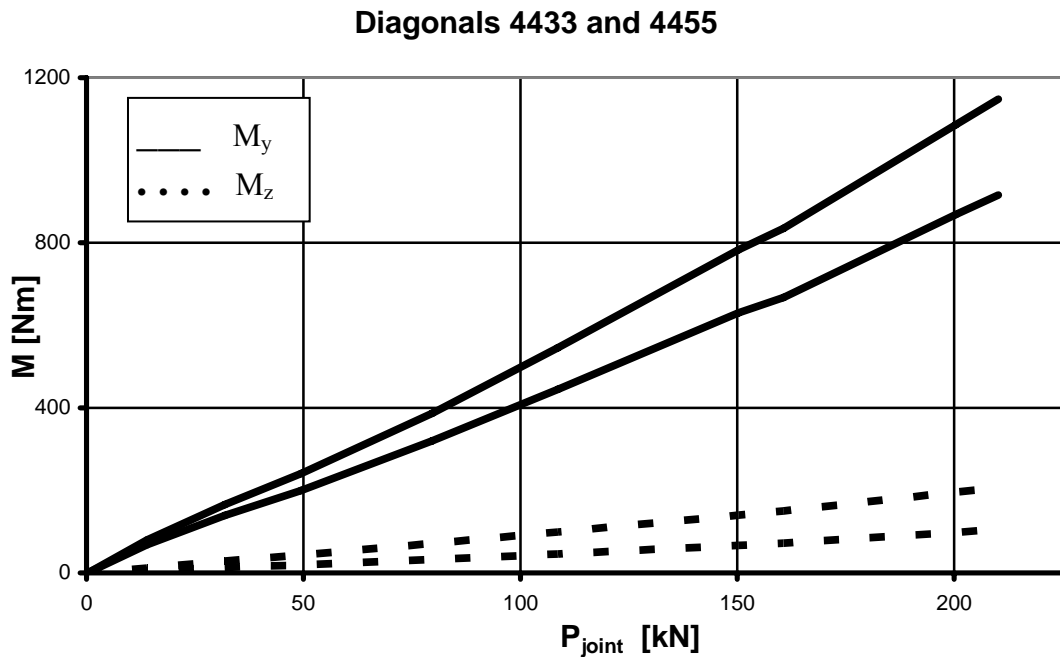


Figure 2.38 Bending moments-external joint load diagrams of the buckled diagonals

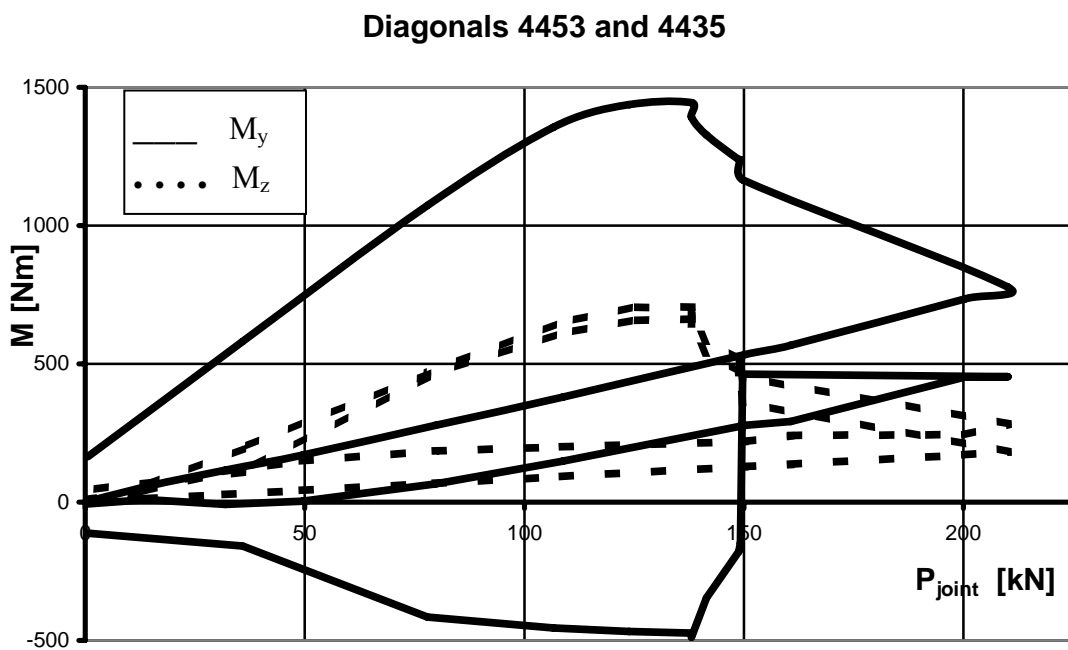


Figure 2.39 Bending moment-external load diagrams of the two non-buckled diagonals

Finally on Figure 2.40 are the bending moment-external load diagrams of two horizontal bars at joint 44 in the upper bar layer. The horizontal bars have mainly normal forces until the collapse, but in the post-buckling range there are significant bending moments, too.

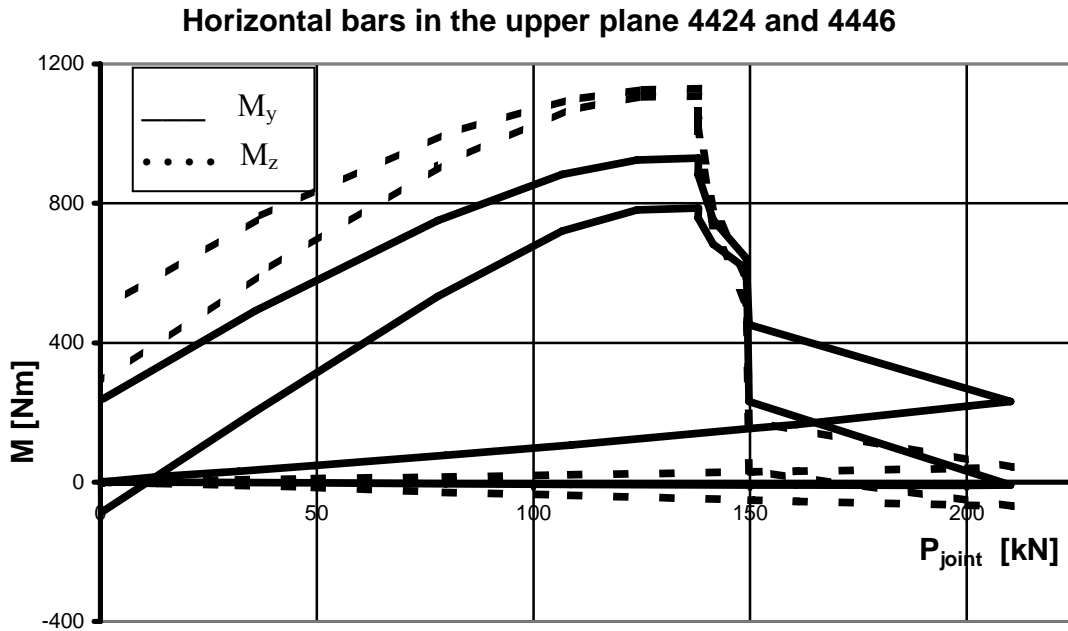


Figure 2.40 Bending moment-external load diagrams of two horizontal bars

The theoretical connection conditions in space trusses are pinned at the end of the bars. From the results of strain gauges it's shown that in real connections there are normal forces and bending moments together, so the real connections are semi rigid and not pinned connections.

2.5. Individual experiments on the bars

Experiments were done on 16 bars of the specimen after disassembly of the truss for better understanding of the behaviour of the bars in the roof-system. A special supporting joint plate system was applied, which models the supporting and connecting setup of the diagonals in the original space-truss. Compression experiments were done and hydraulic jack applied the load again. During the disassembly of the truss we were careful with the strain gauges, and tried to save them for further use. All of the examined bars have remained strain gauges and most of them still have worked, so these gauges were used during these experiments. The individually compressed bars, which were mainly diagonals,

had the same behaviour during the compression experiments as the bars in the full-scale truss section. The high-strength bolts were pre-stressed by the same moment 250 Nm as in the space-truss. The test set-up of individual experiments is seen on Figure 2.41.

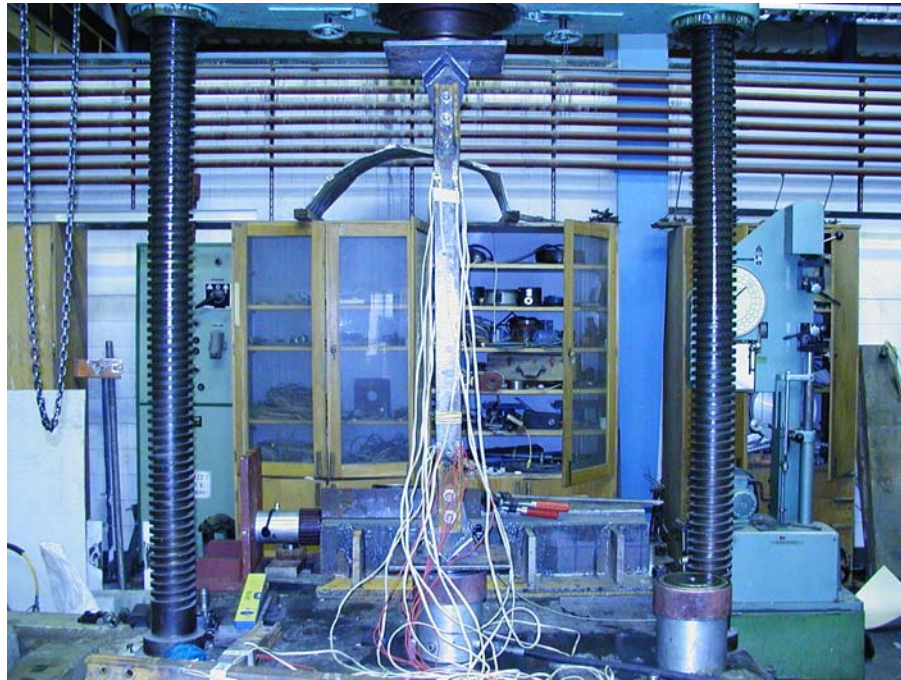


Figure 2.41 The test set-up of compression experiments

The collapse of the bars was local plate buckling at one end of the bars (14 bars) and at both ends (2 bars) next to the bolted connection, where the cross section is the original hollow squared section. The buckling shape was the same as the buckled diagonals in the full-scale test (see Figure 2.42 and Figure 2.37).



Figure 2.42: Local buckling shape of compressed bars

The average load bearing capacity of the 16 bars was $P_{\text{max. average}} = 112.6 \text{ kN}$. The sound effect(s) due to the bolted connection(s) slipping has occurred during the experiments. A typical load-deformation curve of bars is shown on Figure 2.43. The results show that the supporting plates modelled well the real supporting of the diagonals.

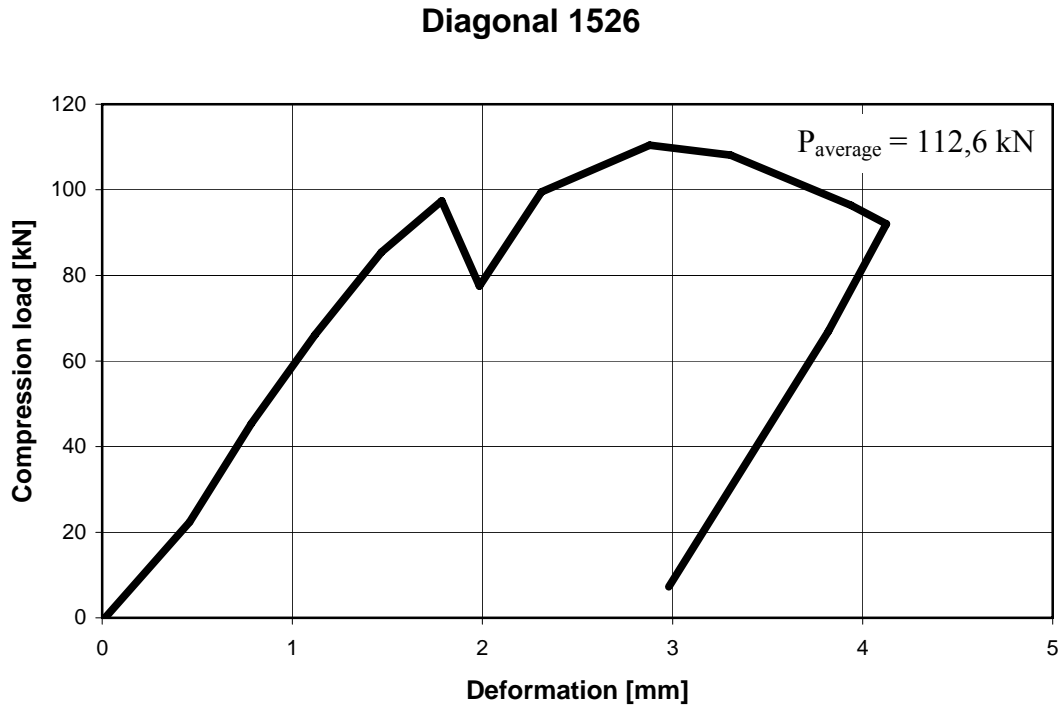


Figure 2.43 A typical load-deformation curve of bars

2.6. Conclusions

In this chapter I performed the full-scale experiments and numerical examinations of a steel space-truss roof segment. Obtaining the best numerical results, I had to model the special formation process of the bars, and I verified this model by three dimension (3D) laser beam scanner. On the verified bar model numerical experiments were done applying different load cases to investigate the behaviour of the hollow sectioned truss bars. The results of the full-scale experiments were modelled by finite element method. I demonstrated by both of the experiments and the numerical models that secondary bending moments are arisen at the joints of trusses, due to the imperfect geometry and the bolted connections, while the general model assumption to the truss joints is pinned. The semi-rigid type of joint can be considered in the FEM model during the numerical analysis.

New results of this chapter: Simulations of Producing and Design Structures

a) simulation of the formation procedure of the bars

On the basis of the producing process, I investigated a numerical model of the formation procedure of the bars. I had to model the formation process to obtain the real model of flattened bar ends. The formation takes effect just at the end of the bars. Therefore I decided to model only a part of the bar, near the flattened end instead of the whole member. Furthermore it is decided to model only the quarter of the hollow cross section and the half of the pressing tool due to the symmetry of the members and the formation process. The loading was displacement controlled.

I applied a new method for the verification of the result of the numerical analysis, a 3D laser scanner. I verified the numerical model with good coincidence.

b) numerical analysis of compressed bars

I created the numerical model of the whole bar applying the resulted shape of the quarter bar model of the "flattening" process. I performed several loading on this model to find out the real behaviour of the built up truss members. The applied load cases were: concentrated compression force, pure bending moment in both direction, pure torsional moment, normal force with two bending moments (large eccentricity), normal force with small eccentricity.

The small eccentricity was the tenth of the width of the bar. I get the best solution of the truss bars with the last loading model, the small eccentricity.

I verified the numerical results of the whole bar model with the comparison of my experiments on individual bars.

c) numerical analysis of the steel space-truss

I created the numerical model of the investigated steel space-truss. The model contains special connections at the joints, which take into account the semi-rigid effect of the secondary bending moments. This model is applicable to present the three full-scale experiments.

- eccentric concentrated force on the top side joint in the elastic range
- concentrated force on the top mid joint in the elastic range
- concentrated force on the top mid joint until collapse

Applying this model I can calculate other special load cases on this space truss without real full-scale experiments.

REFERENCES II.

- [13] Fülöp A., Iványi M. *Experimental Examination of a Space-truss Roof System (abstract)*. In: 13th Inter-Institute Seminar for Young Researchers from the Technical Universities of Budapest, Cracow and Vienna, Vienna, Austria, October 26-28, 2001, pp. 11.
- [14] Fülöp A., Iványi M. *Acél térrácsos tetőszerkezet kísérleti vizsgálata*. Tassi Géza, Hegedüs István, Kovács Tamás, szerkesztők: A Budapesti Műszaki és Gazdaságtudományi Egyetem Építőmérnöki Kar Hidak és Szerkezetek Tanszéke Tudományos Közleményei, Halász Ottó születésének 75. évfordulója alkalmából, Műegyetemi Kiadó, Budapest, 2002, p. 37-42.
- [15] Fülöp A. *Effect of semi-Rigid Joints of Space-Truss Steel Structures*. In: Peter Schiebl, Norbert Gebbeken, Manfred Keuser, Konrad Zilch, editors, Proceedings of the 4th Ph.D.Symposium in Civil Engineering, Munich, Germany, September 19-21, 2002. Springer-VDI-Verlag GmbH & Co.KG, Düsseldorf, 2002, Volume 1, pp. 169-177.
- [16] Fülöp A., Iványi M. *Full-Scale tests of a Space-Truss Roof System*. In: Iványi Miklós, editor, Proceedings of the Stability and Ductility of Steel Structures, Professor Ottó Halász Memorial Session, September 26-28. 2002, Budapest, Akadémiai Kiadó, Budapest, 2002, p. 387-393.
- [17] Fülöp A., Iványi M. *Full-scale tests of a space truss roof system*. In: Jármái Károly and Farkas József, editors, Metal Structures: Design, fabrication, Economy, Proceedings of the International Conference on Metal Structures – ICMS-03, Miskolc, Hungary, April 3-5, 2003, Millpress Rotterdam Netherlands 2003, pp. 93 – 97.
- [18] Fülöp A., Iványi M. *Experimentally Analyzed Stability and Ductility Behaviour of a Space-Truss Roof System*. International Journal of Thin-Walled Structures, Elsevier Science Ltd, February 2004, Vol 42, pp. 309-320.
- [19] Fülöp A., Iványi M. *Buckling Modes of Flattened Edges Rectangular Hollow Members*. In: B.H.V. Topping, editor, Proceedings of The Ninth International Conference on Civil and Structural Engineering Computing, 2-3 September 2003, Egmond-aan-Zee, The Netherlands, Civil-Comp Press, Stirling, Scotland, 2003, pp. 105-106 + CD-ROM: Paper 42, 10 pages.
- [20] Hibbitt, Karlsson & Sorensen, Inc. ABAQUS/ Standard User's Manual Version 6.3
- [21] Fülöp A., Iványi M. *Coupled Buckling Modes of Rectangular Hollow Members*. In Proceedings of the Fourth International Conference on Coupled Instabilities in Metal Structures, CISM 2004, Rome, Italy, 27-29 September 2004, pp. 247-256.
- [22] Fülöp Attila, Iványi Miklós *Acél térrács kísérleti és numerikus vizsgálata*. MAGÉSZ – Acélszerkezetek különszám, 2004, pp. 37-40.

- [23] Iványi M, Fülöp A. *Buckling Behaviour of Rectangular Closed Cross Sectional Members*. In: Dan Dubina and Daniel Grecea, editors, Recent Advances and New Trends in Structural Design, International Colloquium Dedicated to the 70th Anniversary of Professor Victor Gioncu, Editura Orizonturi Universitare, Timisoara, 2004, pp. 155-164.
- [24] Fülöp A., Iványi M. *Numerical Analysis of the Buckling Behaviour of Rectangular Hollow Members*. In: B.H.V. Topping, C.A. Mota Soares, editors, Proceedings of The Seventh International Conference on Computational Structures Technology, 7-9 September 2004, Lisbon, Portugal, Civil-Comp Press, Stirling, Scotland, 2004, pp. 347-348 + CD-ROM: Paper 156, 10 pages.
- [25] Fülöp A., Iványi M. *Buckling Analysis of Space-truss Roof System. Experimental and Numerical Investigations*. In: B. Hoffmeister, and O. Hechler, editors, Proceedings of the Fourth European Conference on Steel and Composite Structures, Research-Eurocodes-Practice, EUROSTEEL 2005, Maastricht, The Netherlands, June 8-10, 2005, Druck und Verlagshaus Mainz GmbH, Aachen, 2005, Volume A, pp. 1.2-155 – 162.

3. Refurbishment of ancient masonry structures

3.1. Introduction

The refurbishment of existing buildings is today an emerging activity, which recalls more and more interest of the building industry. In recent years numerous problems arise about basic principles and actual technique for strengthening monumental buildings, having become apparent that the great majority of the materials used in the past have only a very short life with respect to the life of the structure. The old masonry buildings are very often damaged by the age and by the ravages of time and, therefore, they require structural consolidation and functional rehabilitation. But also more recent buildings made of reinforced concrete sometimes need refurbishment operations due to their bad state of preservation.

The development of these activities acknowledges steel as a suitable material both from structural and architectural point of view. In fact, refurbishment requires constructional systems which guarantee flexibility of execution and simplicity of erection. For this purpose, the constructional steel offers "prefabricated" types of technology, which allow the designers to find "ad hoc" solutions and to achieve optimum results tailored to specific requirements.

From the structural point of view, the analysis of several practical examples collected from all over the world shows that steel construction is widely and successfully used at all levels of consolidation of already existing structures. These levels are differentiated in order of importance according to the main constructional phases, which are commonly defined in order of importance as safeguard, repairing, reinforcing, restructuring.

It is interesting to observe that steelworks can be conveniently used for the consolidation of all kind of structures, both old and new, made of all common constructional materials, i.e. masonry, timber, reinforced concrete and also steel, itself. In addition, the use of steel is very effective in strengthening structures against earthquakes.

When the building to be consolidated is a historical monument, its restoration is the most delicate operation for the designer and the use of steel gives him further advantages. In fact, in strict agreement with the basic criteria of the modern theory of restoration, the existing building must be conserved and integrated by new works necessary to ensure both adequate safety level and suitable functionality.

As a consequence it is now believed by most researchers that the potential reversibility of the intervention has a key role in the evaluation of the appropriateness of the

strengthening technique, reversibility being defined as the possibility of restoring the situation preceding intervention. Such new works must have an unmistakable, modern and reversible feature, by means of methods and materials which can be removed without damaging the existing structure. Steel technology expresses its advantages of suitable material in terms of strength and lightness. A logical application of these principles undoubtedly shows that steel has the necessary prerequisites of being a new material with "reversible" characteristics, particularly suitable to take its place alongside the materials of the past, in order to form together integrated structural systems. These prerequisites are being particularly appreciated when the building to restore has architectural and historical importance.

The masonry buildings represent ones of the best known and the most widespread constructions to be used for. These kinds of structures, carried out in all over the world, have been built since very ancient times. Until the 18th century or so, the masonry structures had been erected as a result of almost the only one solution to create a new building. Although since that time the role of masonry material for representation as main load-bearing structure has been gradually decreased and changed by more modern materials (e.g. steel or reinforced concrete), exact knowledge of mechanical performance and implementation procedures of these constructions have to be paid with particular attention by the technological experts and the building industry of today, with absolute certainty, of future, too. Amongst the innumerable lots of masonry structures from all around the world, there are a large number of monuments, churches and old historical buildings, made of that.

For the reference, a mention must be made that in Italy the stone masonry church buildings were especially widespread and popular to be constructed, corresponding to different historical eras and their trends of style. These latter masonry churches and their examination in case of required restoration works were mostly considered at the structural model for calculations. Furthermore, time after time these old structures have often got several types of structural failures, such as spread cracking or partial collapses of walls, damages of masonry crossings and corners, disconnections of walls or crossings. In general, all of these damages can be justified firstly of all by the typical features of old dwelling or church buildings, including highly slender masonry uprights, lack of horizontal diaphragms, thrust of arches and vaults, lack of adequate connection in masonry crossings, ageing of structural material, and so on. On the other hand, it is very often necessary to improve the structural behaviour of masonry buildings, as respect to certain new load cases

(due to, for example, new type of functional use or recent environmental effects). As a consequence of the afore-mentioned facts, refurbishment of these old masonry constructions is strongly needed for the preservation in a lot of cases. This strengthening and upgrading activity, required in this way, generally is to be carried out due to public, historical, architectural, economic and, of course, structural interests. Moreover, in such refurbishment cases, the development of these activities acknowledges steel as a suitable material which, with its prefabricated types of technology, provides flexibility of execution and simplicity of erection - at the same time.

The possibility of increasing the strength (or in general, the safety against the collapse) of elements by a lateral confinement constituted by pre-stressed bars and confining plates is of particular interest.

From a qualitative point of view, it is evident that a confinement will increase the safety of the structure, and the basic mechanisms which will allow such an increment are qualitatively clear, as well. Nevertheless many questions remain without an answer if a precise evaluation of the safety of the strengthened structure is required, as a function of appropriate parameters of the original structure and of the strengthening intervention.

An interesting application of this technique has been applied at the case of a medieval masonry tower the Fraccaro Tower, Pavia, Italy (Figure 3.1).



Figure 3.1 The Fraccaro Tower of Pavia¹

¹ http://www.lombardiabeniculturali.it/img_db/bca/1A050/1/1/579_pv101001.jpg

3.2. Numerical simulation of the lateral confinement

3.2.1. The collapse of the Civic Tower of Pavia

In the medieval age it was common for Italian families of wealth and influences to build tall rectangular towers, primarily as status symbols, but perhaps also with a defence purpose, either against external enemies or local factions involved in power struggles.

Construction of the Civic Tower of Pavia (Figure 3.2) was started in the early middle ages as the bell tower of the medieval cathedral, but the recorded history of the tower starts in the 11th century, when the lower part of the tower was built. The upper part, involving a Renaissance bell tower, was designed and constructed in the last part of the 16th century.

This tower was different from the other local towers, both because of its history and its geometry: it was much wider and, consequently, apparently squatter than other towers, with stairway spiralling up around the tower within the thickness of the walls, which were of uniform thickness; an unusual detail. A consequence of the temporal discontinuity of construction was also the in-homogeneity of the material, with Roman and medieval bricks, stones, river gravel, and mortar of different quality being used over the years. A recent survey performed by town officials had not given any concern; on the contrary, the tower was considered in excellent shape, and project for its opening to the public had been performed.



Figure 3.2 The Civic Tower of Pavia²



Figure 3.3 The Civic Tower after collapse [38]

² http://www.lombardiabeniculturali.it/img_db/bca/1A050/1/l/606_pv102001.jpg

Despite the apparent excellent condition, the Civic Tower collapsed without warning on March 17th, 1989 at 9:00 a.m. (Figure 3.3), killing four people and damaging surrounding buildings and the adjacent 15th century cathedral (Duomo).

The weather conditions before and at the time of the collapse were normal and no works of any importance had been carried out on nearby structures or the surroundings. The only recent exceptional event had been a cyclone that had swept the city about seven months before when the wind reached a maximum speed of about 180 km/h.

The medieval walls, built according to the techniques normal at that time for building towers, were characterised by an external brick cladding ranging from 120 mm to 400 mm with an average of 150 mm, with the intermediate portion of the walls consisting of irregular courses of bits of brick and stones alternated with mortar, constituting a sort of conglomerate, as mentioned above (Figure 3.4). The walls of the second building phase were characterised by a much more irregular filling and by thinner external facings. The ratio between the thickness of the external leaf of the wall and the internal one was approximately 1/16.

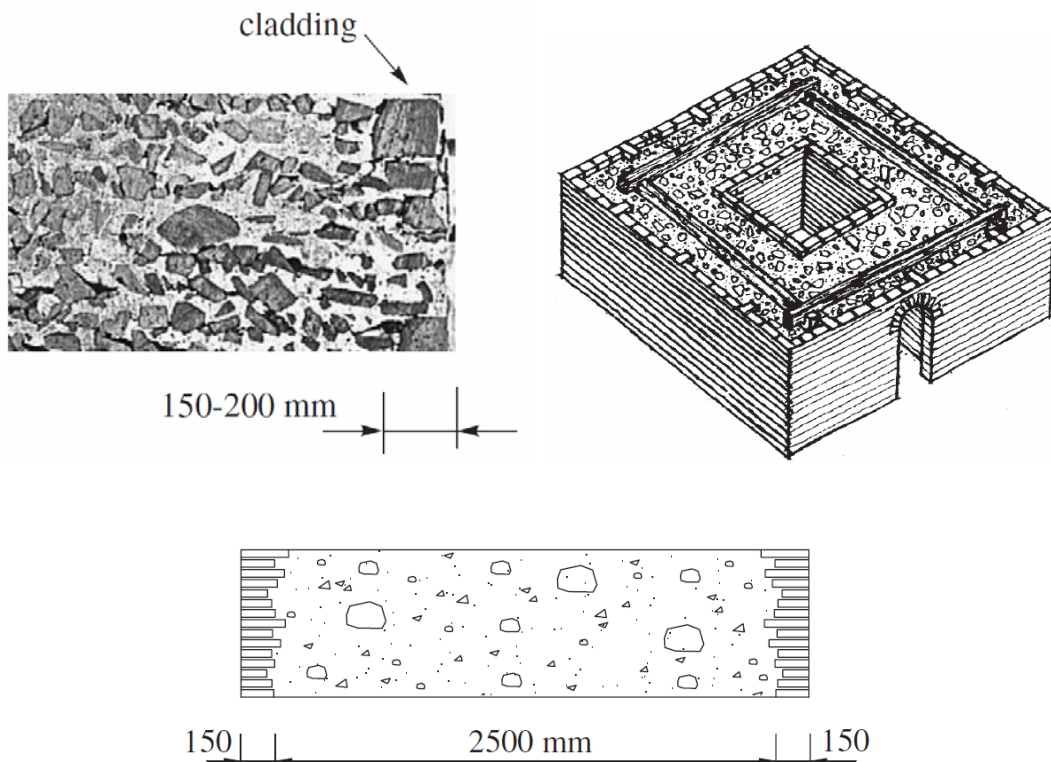


Figure 3.4. Typical cross section through wall thickness showing "sacco" construction [37]

After the collapse approximately 100 large blocks of masonry were extracted from the 7000 cubic meters of debris, among them two large blocks' 2.8 m wide which were tested to destruction.

Mechanical tests on specimen obtained from remaining parts of the tower are of particular interest for what concerns the discussion of the failure mechanism. Compression tests have been performed on wallets with dimensions of the order of 290 mm x 650 mm x 700 mm, cut from the inner conglomerate or from parts constituted by bricks and mortar; and on wall obtained from two major remaining blocks, with dimensions of the order of 700 mm x 2700 mm x 2500 mm, which represent intact portions of the entire width of the original walls.

3.2.2. Experimental tests

The possibility of increasing the strength (or in general, the safety against the collapse) of elements by a lateral confinement constituted by pre-stressed bars and confining plates is of particular interest. From a qualitative point of view, it is evident that a confinement will increase the safety of the structure, and the basic mechanisms which will allow such an increment are qualitatively clear, as well.

G.Ballio and G.M.Calvi performed a research in 1992 in Pavia. The main objective of the research included the determination of the increment of strength, deformability and energy absorption capacity obtained as a consequence of a lateral confinement of a masonry wall, as a function of appropriate parameters, such as a ratio between bar and plate area, a ratio between distance of two plates and wall thickness, and expected failure modes.

To pursue this objective twelve wallets, obtained from medieval masonry walls, have been tested varying the parameters mentioned above in order to obtain three possible failure mechanisms:

- yielding of the horizontal bars;
- punching of masonry underneath the confinement plates;
- shear-tensile failure of masonry in the less confined zones between plates.

The large scatter of material properties, together with the limited number of available specimens, would have not assured a dependable interpretation of the results through a correlation of different tests on different specimens. Each specimen has therefore been

loaded at maximum load, strengthened, and loaded to failure, then considering percental increments rather than absolute values of the properties of interest.

The masonry walls to be strengthened had been taken from the debris of a medieval tower failed in 1989. The basic material is rather a conglomerate made with pieces of clay bricks and river stones embedded in a lime mortar matrix, then standard brickwork. Such material is common in ancient structures where thick walls present regular brickwork only in the outer skin.

The ultimate strength was in the range of 2 to 4 MPa, with Young modulus varying between 700 and 4600 MPa and the ultimate deformation of 0.3% to 0.5%. A significant cracking process starts at horizontal deformations of 0.02% to 0.8%, while the ultimate deformation is between 2.5% and 5%.

The steel used for the reinforcing bars had a yield stress of about 600 MPa and a uniform elongation capacity (i.e. at maximum force) between 3% and 4%.

Three fundamental failure modes have been considered, as showed in Figure 3.5. For the purpose of some preliminary estimation of the failure mode to be expected, a bi-dimensional behaviour was assumed, imposing a perfect confinement in the third direction. These conditions could correspond to those of a wall with width significantly larger than thickness and have been reproduced in the tests applying much stiffer bars and plates covering the whole side in one of the horizontal directions (Figure 3.6.).

The relative probability of bar yielding versus the punching of masonry depends on the ratio between the bar section and the plate surface, as well as on material properties.

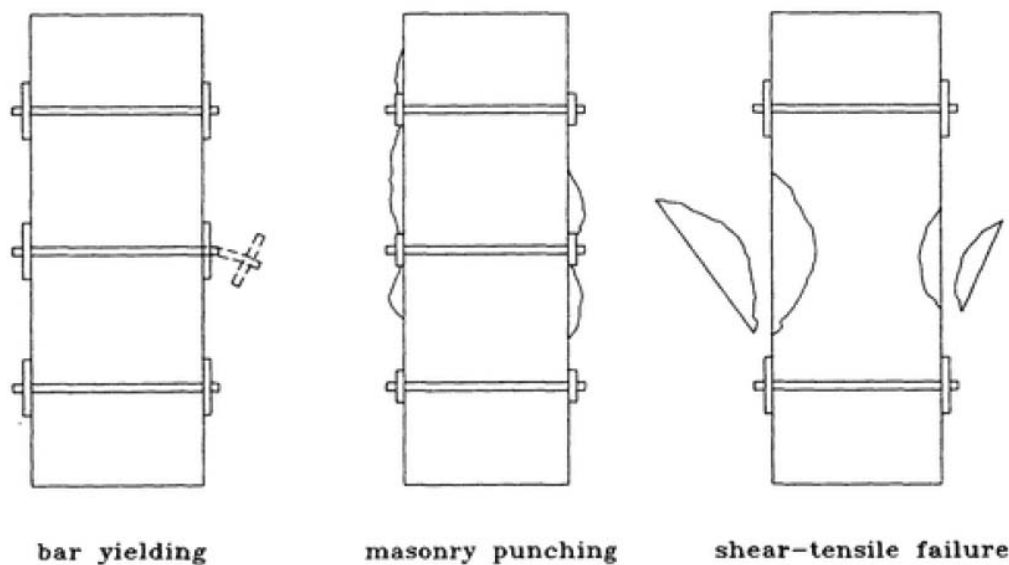


Figure 3.5 Possible failure modes. From the left hand side: yielding of bars; punching of masonry beneath the confining plates; shear-tensile failure in the unconfined region [36]

Assuming a yield strength of steel bars (f_{ys}) of 600 MPa and a punching strength of masonry of 6 MPa (f_{pm} ; it has to be obviously higher than compression strength), an equal probability of failure is obtained for a ratio of 100 between area of plate (A_p) and area of bar (A_b). For this reason squared plates with side of 40 and 80 mm have been used in conjunction to 6 mm diameter bars, obtaining $A_p/A_b=57$ and 226.

The approximate dimensions of the wallets were 290 mm x 650 mm x 700 mm, with a vertical load applied on the 650 x 290 sides, and the previously mentioned “perfect” confinement on the 700 x 290 sides.

On the 650 x 700 sides 4 or 9 plates were applied, tied with 4 or 6 mm bars located through holes very carefully drilled. A slight tensile stress (70 to 300 MPa, depending on number and diameter of bars) was applied to the bars before testing the strengthened specimens, obtaining an average compression stress in the masonry of approximately 0.05 MPa. As already mentioned this was not considered a fundamental parameter.

All bars were instrumented with strain gauges, displacement transducers were applied to measure vertical and two horizontal deformations (Figure 3.6).

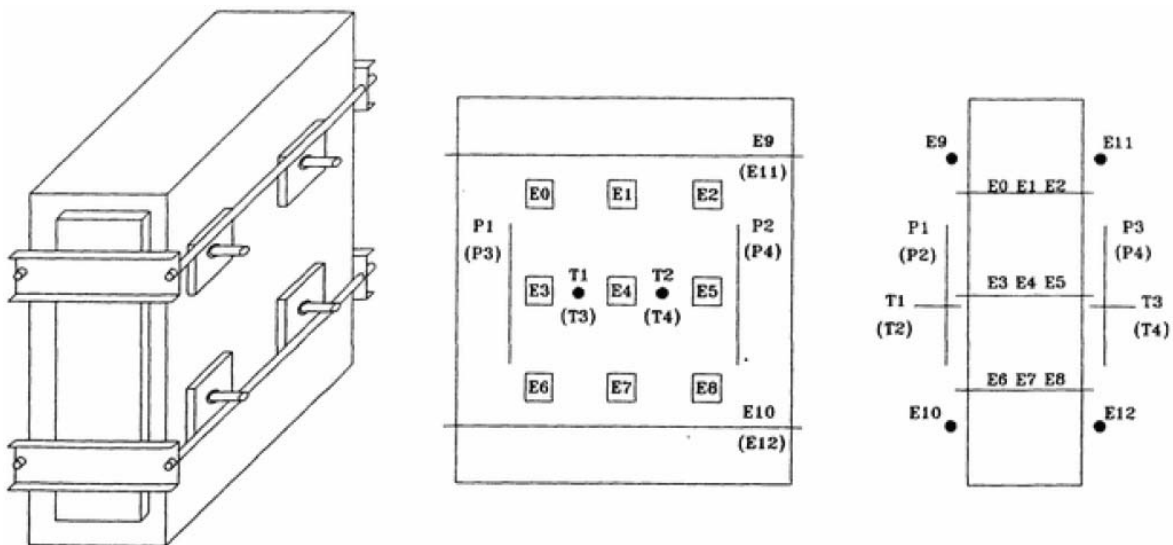


Figure 3.6 Test set-up (P: linear potentiometers, T:LVDT, E:strain gauges) [36]

Each specimen had been first loaded to its maximum capacity, then unloaded to 70% of maximum load, confined by tying the plates up and pre-stressing the horizontal bars, and finally loaded to complete collapse. Clearly, all the specimens were significantly damaged before being strengthened.

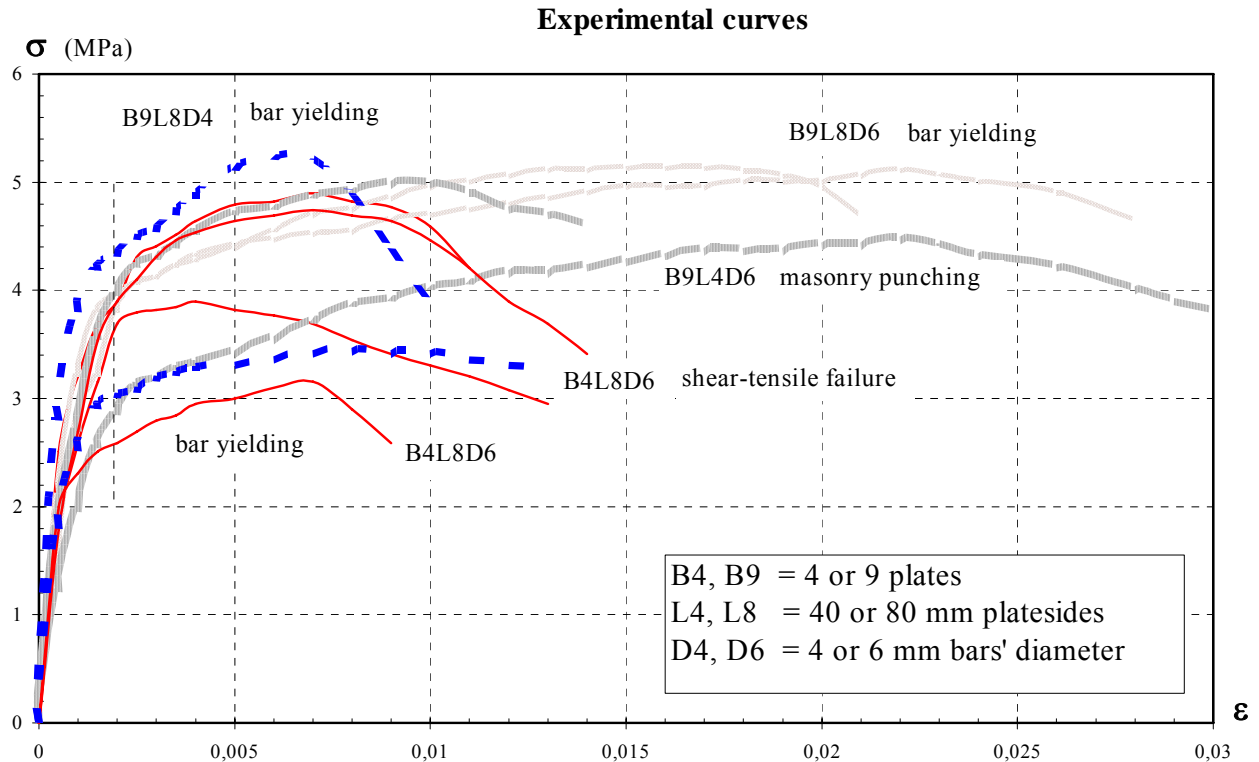
All bars had originally a diameter of 6.5 mm, and only in the region of application of the strain gauge were milled to 6 or 4 mm. As a consequence, the confining force capacities were significantly different in the two cases (of about 50%), but the corresponding total elongation of the bar was approximately the same.

3.2.3. Experimental results

The experiments were performed by G.Ballio and G.M.Calvi in the frame of their research in 1992 in Pavia, Italy. I performed the numerical examinations on the basis of the experiments.

The failure modes experimentally obtained corresponded substantially to the expected modes:

- in three wallets strengthened with four bars, a shear-tensile failure took place in the central (less confined) region. Only in one case, one bar failed (Figure 3.7, B4L8D6 cases). It has to be noted that the shear-tensile failure is strongly affected by the heterogeneity of the masonry conglomerate, it is therefore logical to expect various response in term of post-peak branch as well as in terms of strength, deformation and energy absorption capacity;
- the specimens strengthened with nine 80x80 mm plates and 6 mm bars showed a fracture of one or two bars followed by a rapid strength deterioration (Figure 3.7, B9L8D6 cases);
- punching of masonry has been detected in the case with 40x40 mm plates and 6 mm bars. The strength deterioration progressed gradually to a final shear-tensile collapse of the no more confined masonry (Figure 3.7, B9L4D6 cases);
- eventually, in the case of nine plates and 4 mm bars, an apparently contemporary failure of four bars took place, with an immediate total collapse of the wallet (Figure 3.7, B9L8D4 cases).



The unconfined specimens showed a very uniform strength (average 3.66 MPa). This was probably because all of them had been obtained from the same block of material, therefore being characterised by a random distribution of pieces of bricks and stones but by the same mortar matrix as well.

The strength increments varied from 4% to 43%, with an average of 22.7%. The greater variability was encountered, as expected, in the case of four plates (i.e. shear-tensile failure), with increments between 4 % and 25%.

The recorded Young modulus (E_s , taken on the straight line to the point at 70% of the unconfined strength) was also quite uniform 2854 MPa. No initial hardening due to compaction of voids and closing of micro cracks has been detected.

The ultimate deformation capacity of the unconfined specimens was equal to 0.24%, with an equivalent “ductility” (μ_u , defined according to Figure 3.8) of 1.76.

The ductility calculated for the strengthened specimens (μ_c) was never lower than 7.18 with an average of 9.92. The ultimate deformation was, therefore equal to at least five times the original ultimate deformation, no matter how the walls had been strengthened.

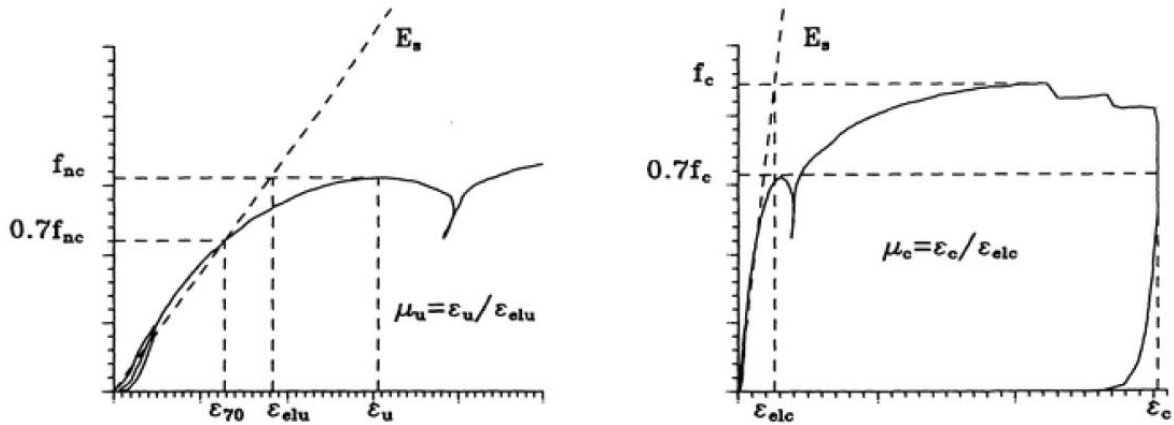


Figure 3.8 Typical stress-strain curve obtained from the tests (the definition used for stiffness, equivalent elastic limit and ductility are shown) [36]

The energy absorption capacity of the strengthened wallets is, on the average, 5.5 times larger than in the unconfined conditions, as expected from the figures given on strength and deformation capacity. These results clearly indicate that the strain energy of the bars has little to do with the increment of the total energy absorption capacity. Actually, if a detailed evaluation of the energy, absorbed by the bars, is performed, values from 30 to 300 times smaller than the increment in energy absorption capacity are found.

Strengthening through confinement is, therefore very convenient from an energy point of view since a negligible amount of energy effectively added allows the exploitation of resources hidden in the original structure. For the same reason, it appears that the increment in the energy absorption capacity is relatively insensitive to modes of failure and confinement details.

The increment of energy absorption capacity is probably related to the phenomena of friction and aggregate interlock.

The summary is in Table 3.1. Each column corresponds to a tested wall, with the indication of (from the top) the number of plates (n_p), the side of the plates (l_p), the bar diameter (f_b), the percental increment of strength (D_f/f_u), the equivalent ductility of the unconfined (μ_u) and confined specimens (μ_c), the ratio between absorbed energy of the confined and unconfined specimens (E_c/E_u), and the ratio between increment of absorbed energy and strain energy effectively absorbed by the bars ($\Delta E/E_s$).

Table 3.1. The summary of the experimental results

n_p		4	4	4	4	9	9	9	9	9	9
l_p	[mm]	80	80	80	80	80	80	40	40	80	80
f_b	[mm]	6	6	6	6	6	6	6	6	4	4
Df/f_u	[%]	25	23	18	4	27	33	17	43	25	12
μ_u		1.83	1.48	1.71	1.46	1.76	1.87	1.89	1.67	1.71	2.25
μ_c		7.9	9.1	8.2	9.3	9.6	17.6	7.2	11.6	8.2	10.3
E_c/E_u		3.7	5.8	4.2	4.5	5.3	9.9	3.4	8.6	4.8	4.7
$\Delta E/E_s$		167	145	205	29	53	73	106	337	98	131

3.2.4. Computer modelling of the experimental test series

The ABAQUS computer program

The computer modelling of the above mentioned experimental test series was performed by ABAQUS FEM calculus program, which was produced by an American firm *Hibbit, Karlsson & Sorrensen Inc.* This program could be widely applied solving any technical problems.

ABAQUS has varied, predefined, all sorts of elements for applying differently (e.g.: three-dimensional continuum elements, two- and three-dimensional disk and shell elements, bars, contact elements as well as their axisymmetrical types). Beyond that special elements are found like mass node, concentrated inertia, spring elements, sound and heat-transfer elements, etc. Also, it is possible to define other special elements.

ABAQUS has many different material models ranging from the simplest ones to the most complex ones. The program offers a wide range of material models to users, from linear elastic-perfectly plastic, over second- or third-degree plastic, or viscoplastic, till concrete material model.

Furthermore ABAQUS has several types of calculating methods (buckling, static, dynamic analysis, etc.), and a wide range of loads, which can be found in applied mechanics and can be described by finite element method.

Development of models

Allowing for the symmetry of both geometry of the model and loading action, only the one eighth of the entire masonry has been considered for the computer analysis (Figure 3.9).

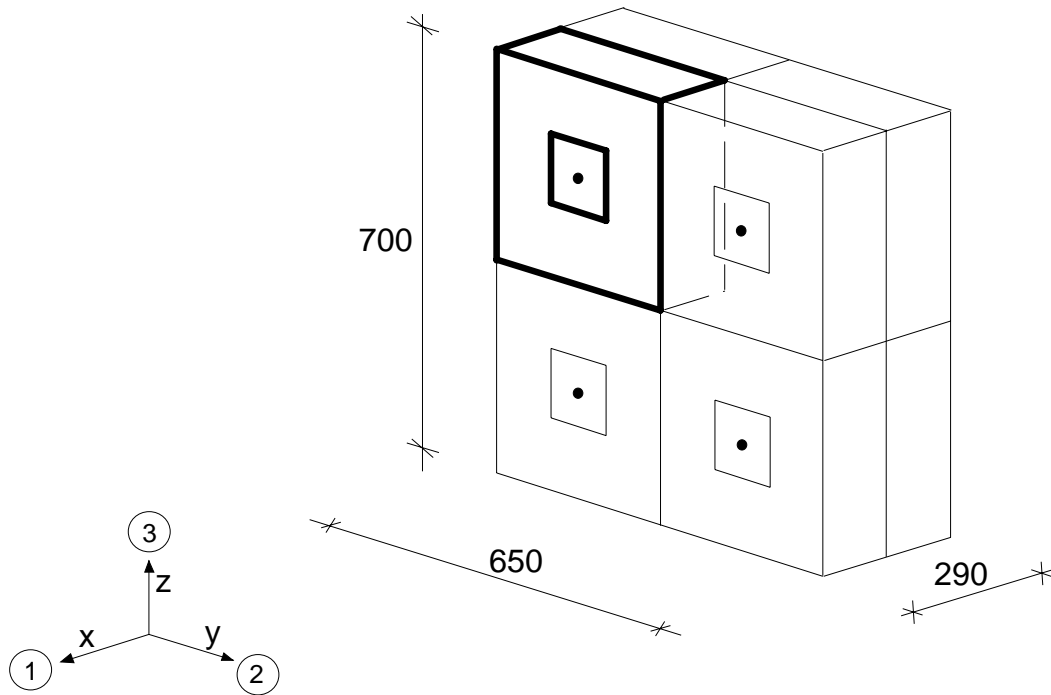


Figure 3.9 The position of eighth model

The dimension of the one eighth model is 350 mm x 325 mm x 144 mm at both of four and nine reinforcing bars. The problem during modelling arises from giving material behaviour of a masonry test wall. Between the experimental results there was not such an σ - ϵ or F - Δl curve, which prescribes the behaviour of unconfined wall under the load process. This curve could be important because the experimental masonry was a conglomerate rather than regular brickwork. During this work, the CONCRETE material model for masonry was applied, which was defined in ABAQUS. This model is used for description of the concrete materials, but it could be used for masonry structures in the consequence of similarly low tensile stress.

Before the CONCRETE command the elastic behaviour of the material must be given by Young's elastic modulus (E) and Poisson coefficient (ν). Under the CONCRETE command, the uniaxial compression curve is given by compression stress - plastic strain

values. The behaviour of material after the first fracture and against the tension could be described by parameters of FAILURE RATIOS and TENSION STIFFENING keywords.

The CONCRETE model is a smeared crack model. It does not track individual "macro" cracks. Rather "concentrated" cracks are calculated at each independent integration point of the finite element model.

For lack of experimental results and equivalent parameters, the experimental behaviour was modelled changing the parameters mentioned before.

Several finite element meshes were made for each case, while the actually best ones found. The finite element components of the finite element models were the followings: 20-node three-dimensional brick elements for masonry (C3D20 and C3D20R - with reduced integration nodes), 4-node shell elements for steel plates (S4R5), 2-node three-dimensional bar elements for steel bars (B31) and INTER4 contact elements between the steel plates and masonry (Figure 3.10).

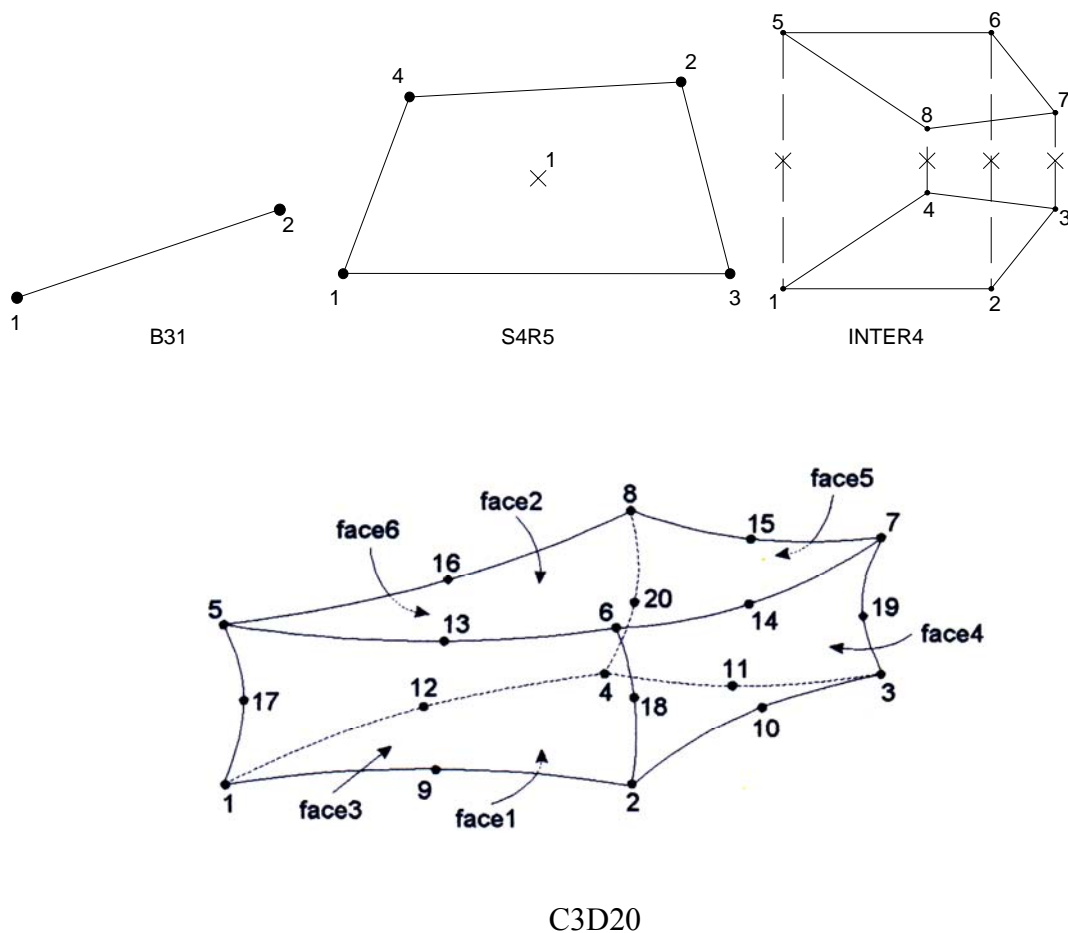


Figure 3.10 Finite elements[30]

The base nodes are z-symmetrical, the two sideplates are y-symmetrical, and the backside is x-symmetrical because of the symmetry relations mentioned above. Because the vertical displacements of the top nodes are the same, the top edge of the front side is supported against x displacement (Figure 3.11).

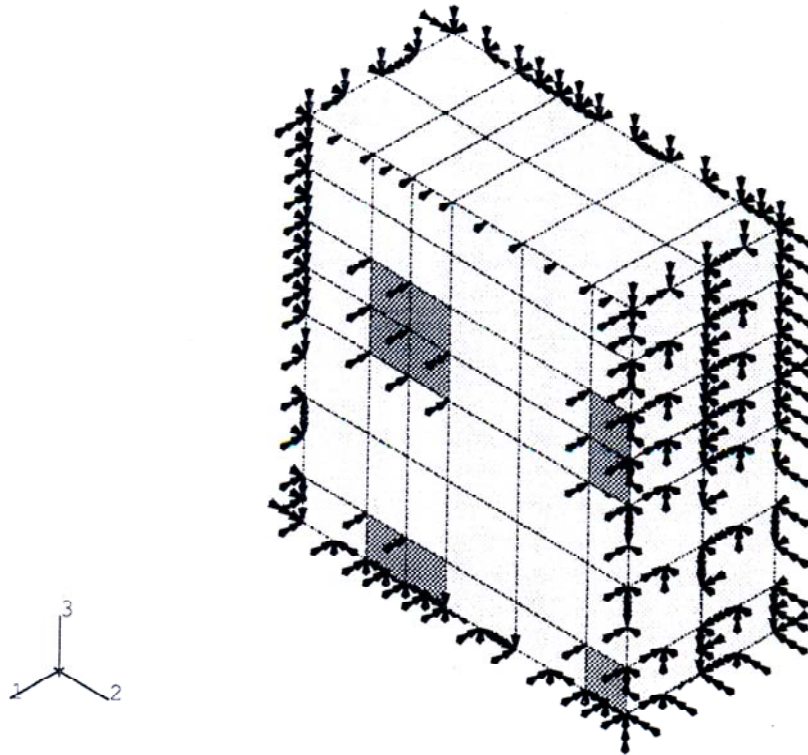


Figure 3.11 Supports

A vertically distributed 10 N/mm² load (pressure) was applied on the top face of top brick elements instead of concentrated loads.

Steel plates could be taken into account as quasi stiff ones. Therefore, high stiffness (E=1.000.000 MPa) and perfectly elastic behaviour were described.

Steel bars initially had linear elastic-perfectly plastic material behaviour (E=210.000 MPa, $\nu=0,3$, $\sigma = 600$ MPa), but at yield stress, the computer signed numerical singularity at bars' nodes. Another material model was applied at steel bars is the DEFORMATION PLASTICITY, which is defined in ABAQUS. This model is applying the *Ramberg-Osgood* plasticity model. In one dimension, the model is (Figure 3.12):

$$E\varepsilon = \sigma + \alpha \left(\frac{|\sigma|}{\sigma^0} \right)^{n-1} \cdot \sigma \quad ,$$

where

σ is the stress

ε is the strain

E is Young's modulus (defined as the slope of the stress-strain curve at zero stress)

α is the "yield" offset

σ^0 is the yield stress, in the sense that, when $\sigma = \sigma^0$, $\varepsilon = (1 + \alpha)\sigma^0/E$; and

n is the hardening exponent for the "plastic" (non-linear) term: $n > 1$

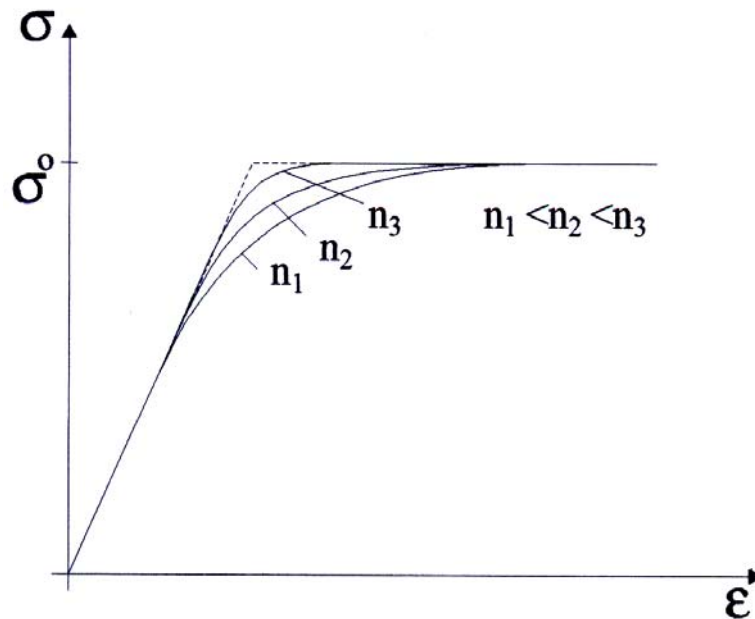


Figure 3.12 Plasticity model [30]

The transverse shear stiffness of bars ($K=G \cdot A$) must be given to this plasticity model. The chosen calculating method was the static analysis with Riks method. The loading during a Riks step is always proportional. The current load magnitude, P_{total} is defined by $P_{\text{total}} = P_0 + \lambda(P_{\text{ref}} - P_0)$, where P_0 is the "dead load", P_{ref} is the reference load vector, and λ is the "load proportionality factor". The current value of λ is found as part of the solution at each increment, and the current load could be calculated from λ as well as the ultimate load could be calculated from λ_{max} . ABAQUS uses Newton's method to solve the non-linear equilibrium equations. Increasing the load ABAQUS calculates the convergence of external and internal forces and displacement correction in equilibrium. If the solution of the actual iteration is not converged, ABAQUS forms the new tangent stiffness for the structure based on the updated configuration, and performs another iteration to try to bring the internal and external forces into balance.

Results in case of four bars reinforcing

Corresponding to the above mentioned parameters, a finite element mesh was done (Figure 3.13) for B4L8D6 case, where the steel plates' edge length is 80 mm, bars' diameter are 6 mm. Two experimental results (a and g curves) from four were quasi the same. The third one (b curve) showed a bit unfavourable behaviour, while in the fourth case (h curve), the effect of the reinforcement was significantly smaller because one bar was fractured. In the first three cases, shear - tensile failure took place in the less confined region of masonry. The results of computer calculation and experimental curves are in Figures 3.14, 3.15 and 3.16.

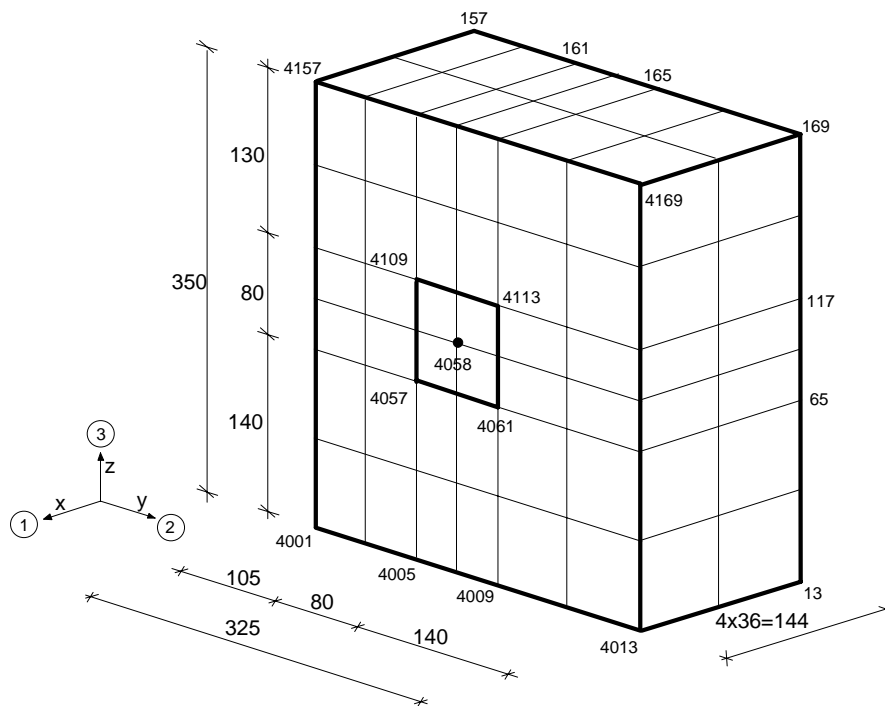


Figure 3.13 wallIn3 model in case of four bars reinforcing

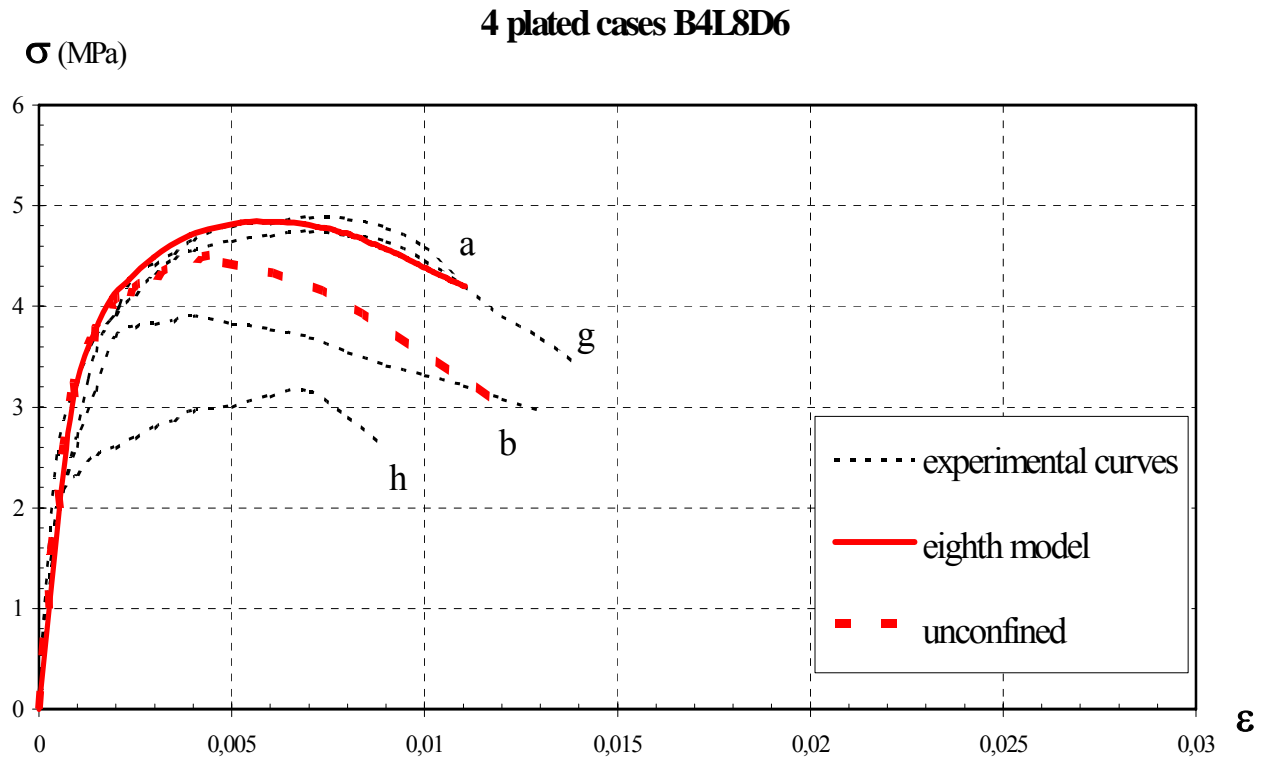


Figure 3.14 Computer and experimental results of B4L8D6

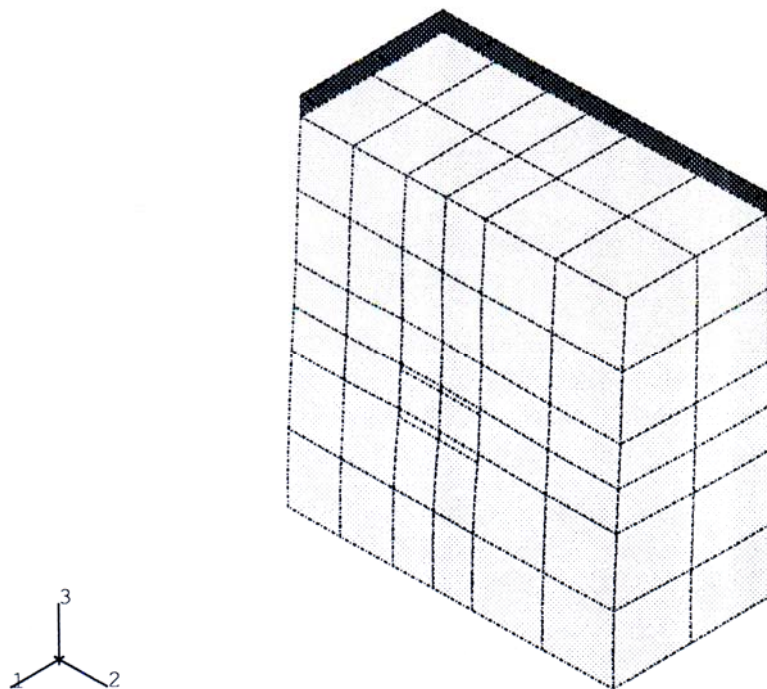


Figure 3.15 Deformed mesh

The material model of steel bars is DEFORMATION PLASTICITY ($E=210.000$ MPa, $\nu=0,3$, $\sigma_0= 600$ MPa, $n=80$, $\alpha=0,7$).

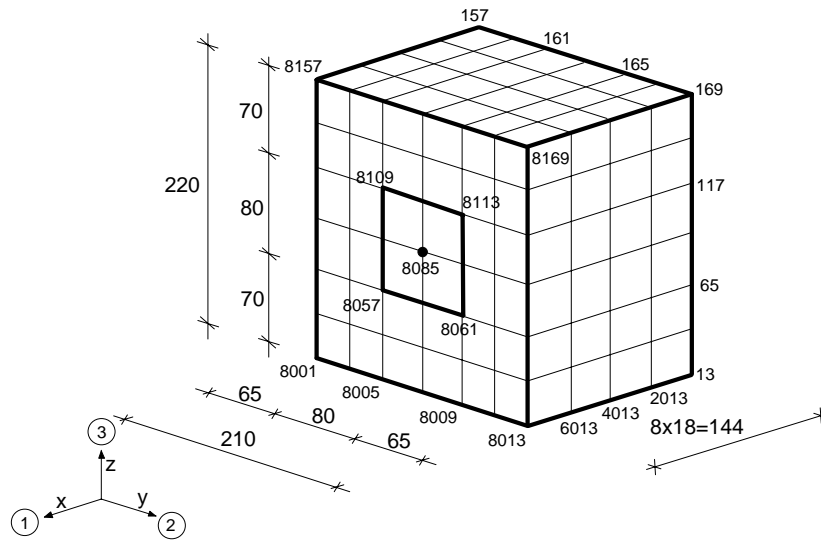


Figure 3.18 *wall2n2m* model with reduced edges in case of nine bars reinforcing

Graphical results of both models are in Figure 3.19 together with the results of unreinforced models. Further graphical results are in Figure 3.20 and 3.21.

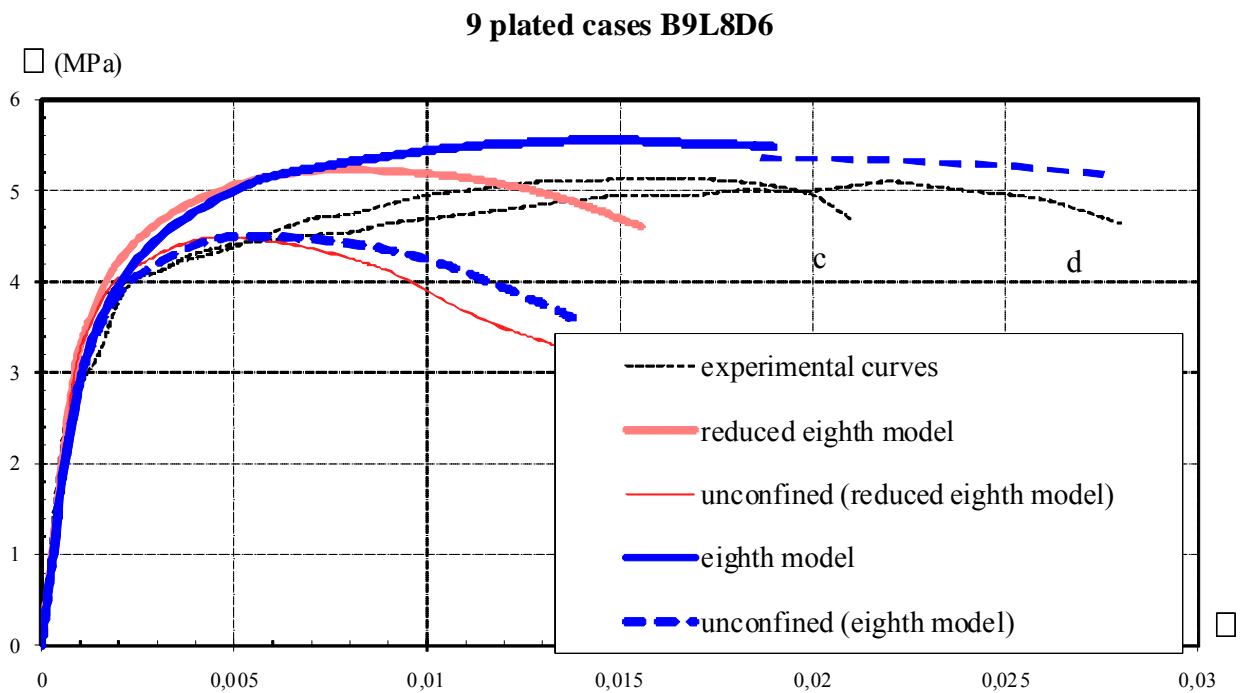


Figure 3.19 Computer and experimental results of B9L8D6

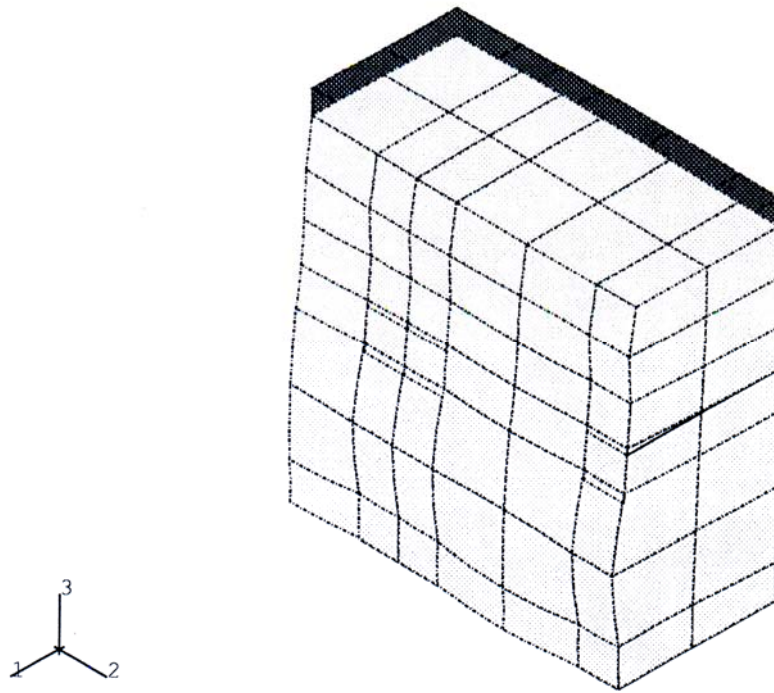


Figure 3.20 Deformed mesh

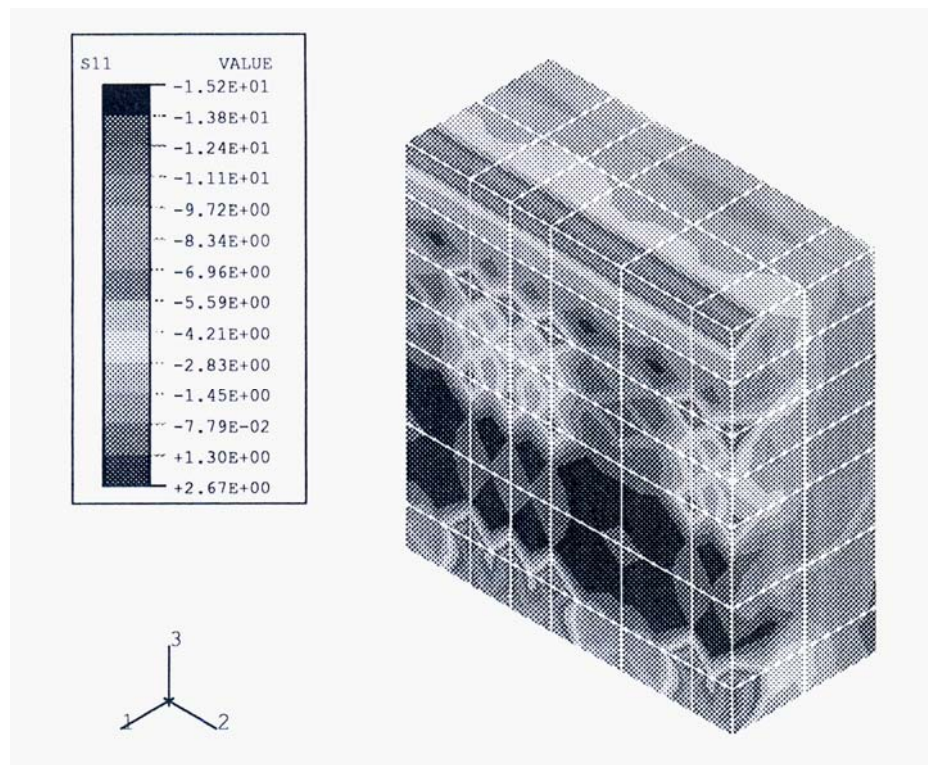


Figure 3.21 σ_{11} stresses' distributions of masonry

The next case is again nine plated model with reduced plate side to 40 mm. The *wall4n* mesh is in Figure 3.22 for B9L4D6 case (40 mm steel plate side, 6 mm bar diameter).

The two experimental results of this case are significantly different. The failure was the punching of masonry. The material model of steel bars was linear elastic-perfectly plastic. Experimental and computed results are in Figure 3.23.

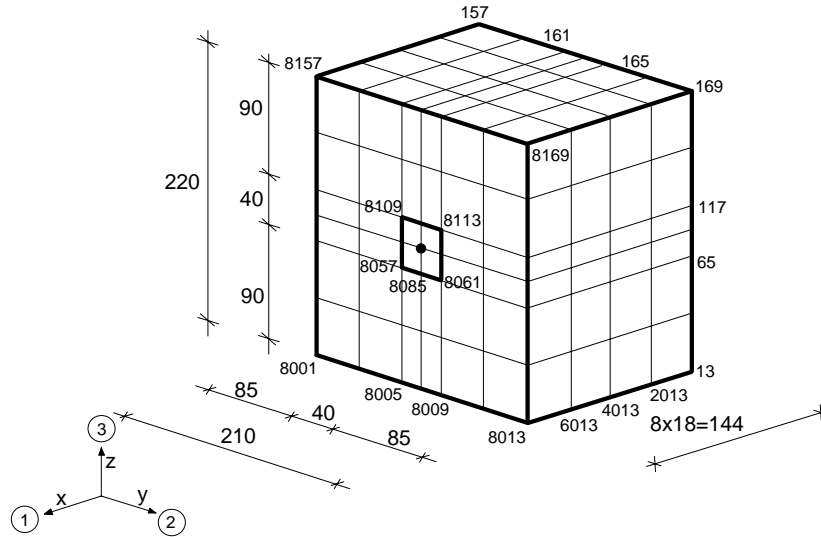


Figure 3.22 *wall4n* model

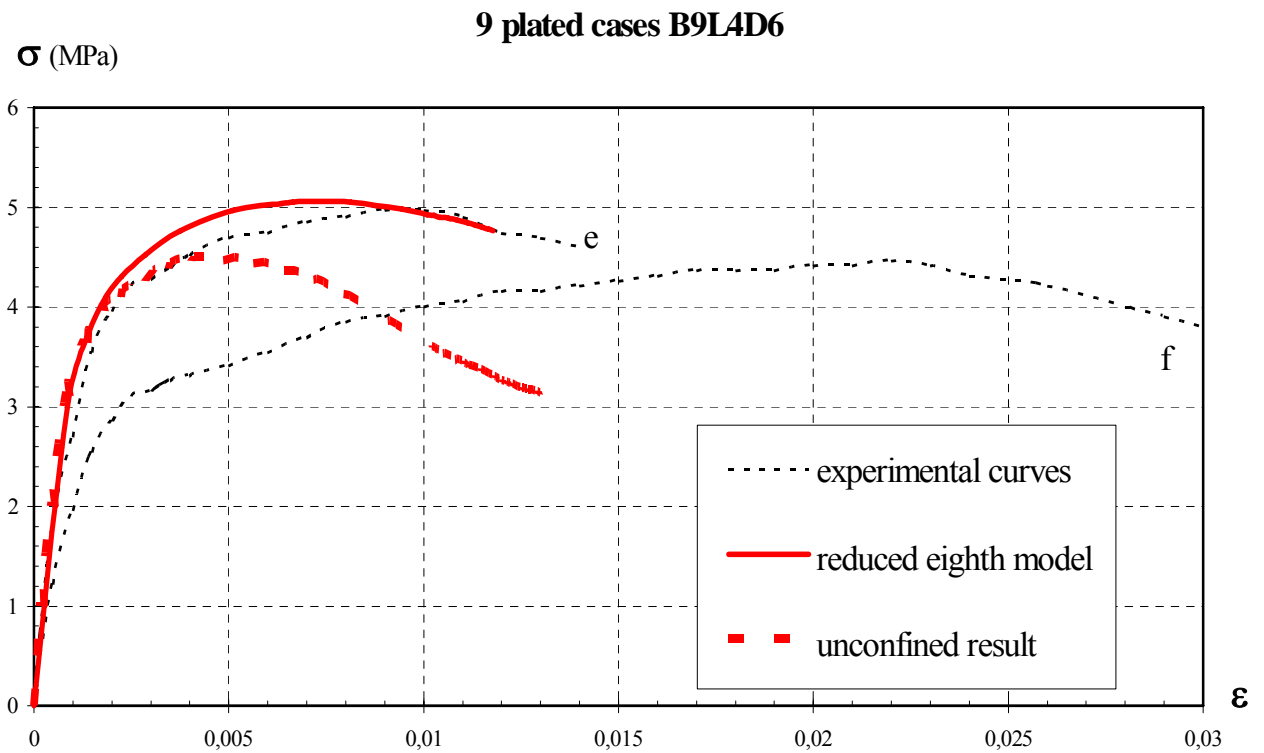


Figure 3.23 Computer and experimental results of B9L4D6

Summary of computed results

The summary can be found in Table 3.2. Each column corresponds to a tested wall, with the indication of (from the top) the number of plates (n_p), the side length of the plates (l_p), the bar diameter (f_b), the experimental equivalent ductility of the confined specimens ($\mu_{c,exp}$), the experimental percental increment of strength (Df/f_u (exp.)), the equivalent ductility of the confined specimens ($\mu_{c,FEM}$), and the computed percental increment of strength (Df/f_u (FEM)).

Table 3.2 The summary of the computed and experimental results

n_p		4	9	9
l_p	[mm]	80	80	40
f_b	[mm]	6	6	6
$\mu_{c,exp}$		7.9, 9.1, 8.2	9.6, 17.6	7.2
Df/f_u (exp.)	[%]	25, 33, 18	27, 33	17
$\mu_{c,comp}$		8.4	11.08, 11.8, (16.15)	8.09
Df/f_u (comp.)	[%]	7.78	23.88, 16.47	13

The equivalent "ductility" μ_c was defined according to Figure 3.24, $\mu_c = \varepsilon_c / \varepsilon_{elc}$ where ε_c is the ultimate plastic strain of confined masonry and ε_{elc} is the elastic strain of confined masonry.

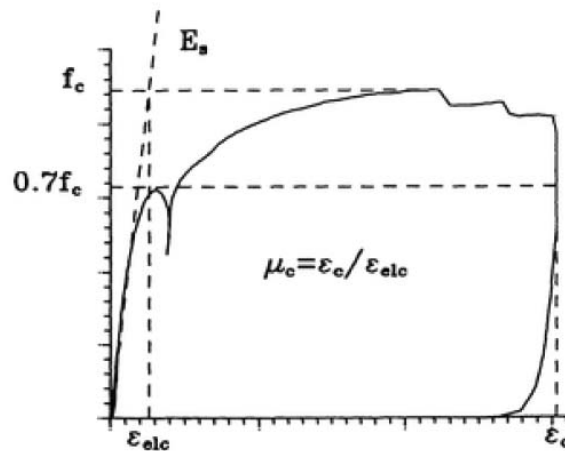


Figure 3.24 Equivalent ductility [36]

3.3. Parametrical analysis series applying lateral confinement

3.3.1. Introduction

Parametrical analysis series were performed applying the lateral confinement reinforcing procedure. The goal of this work was to get designing directives to determinate the effect of reinforcing by computer simulation without experiments.

Italy is frequently attacked by earthquakes. At the same time there are lots of historic buildings in Italy, which have survived many earthquakes till nowadays, but during the centuries they are getting worse.

During an earthquake significant energy quantity is released, which effect buildings by horizontal acceleration and force of inertia. The earthquake resistance of buildings could be increased by reinforcing with steel bars and steel plates absorbing the earthquake energy.

3.3.2. Parametrical test set-up

The computations were done by ABAQUS FEM program. The finite element models were made on the basis of the above mentioned models. The applied models are in Figures 3.25 – 3.30.

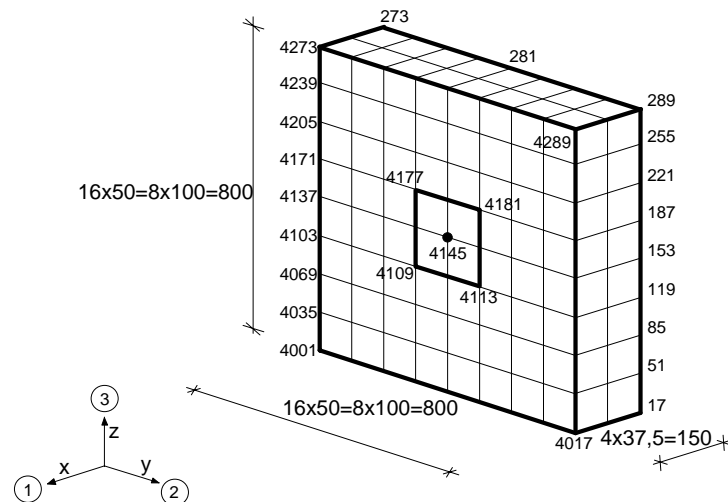


Figure 3.25 *new200n* model

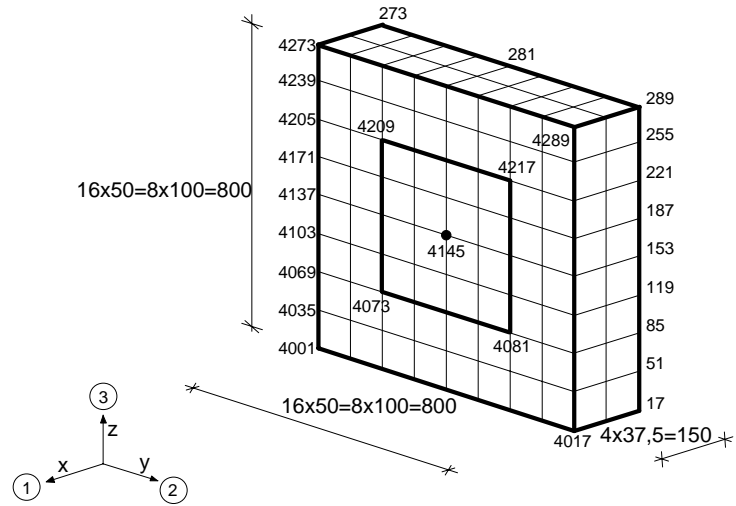


Figure 3.26 new400n model

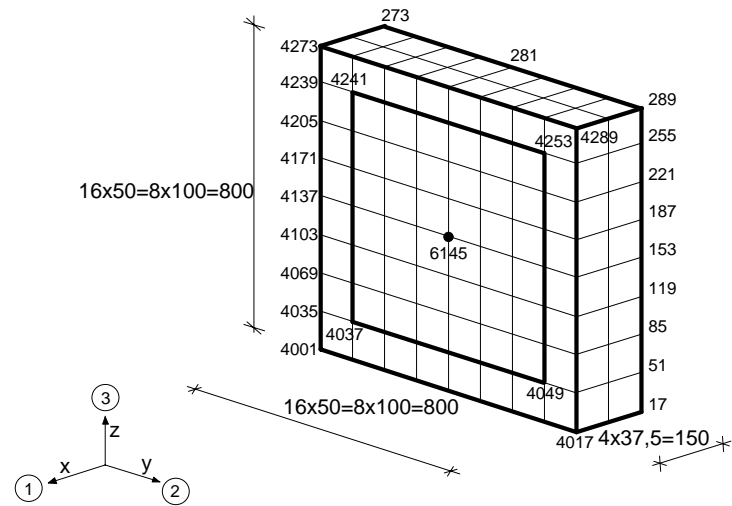


Figure 3.27 new600n model

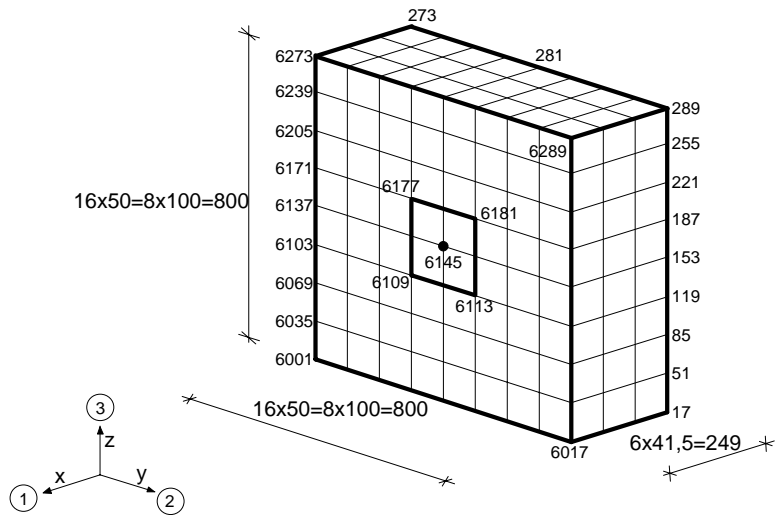


Figure 3.28 new205n model

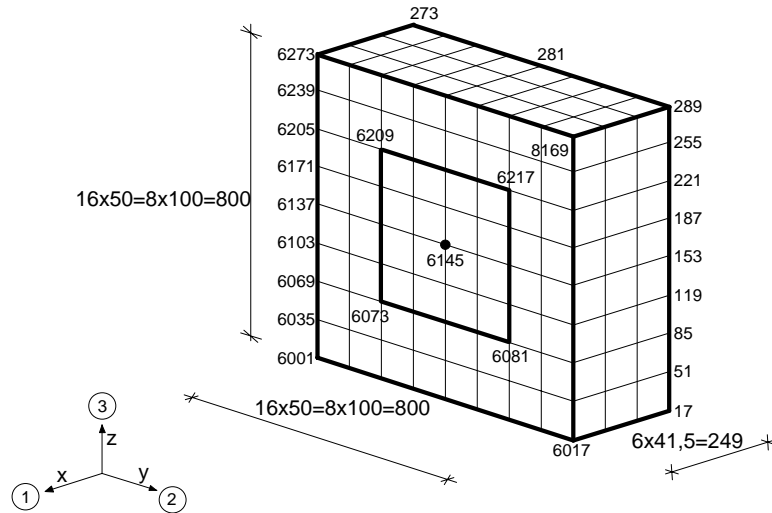


Figure 3.29 *new405n* model

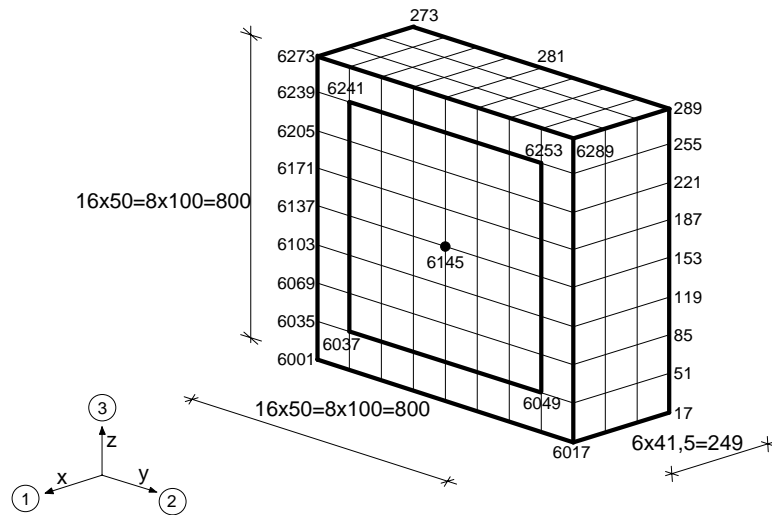


Figure 3.30 *new605n* model

The computed models have $800 \times 800 \text{ mm}^2$ front surface and 300 or 500 mm wall thickness. Three squared steel plate were applied for reinforcing separately with 200, 400 and 600 mm plate side. The steel bars' diameter was 25 mm. Beyond that the unreinforced models were computed with 300 and 500 mm wall thickness.

According to the symmetry relations the base nodes are z-symmetrical, the two sideplates are y-symmetrical, and the backside is x-symmetrical. Because the vertical displacements of the top nodes are the same, and the top and lower edges of the front side is supported against x displacement (Figure 3.31).

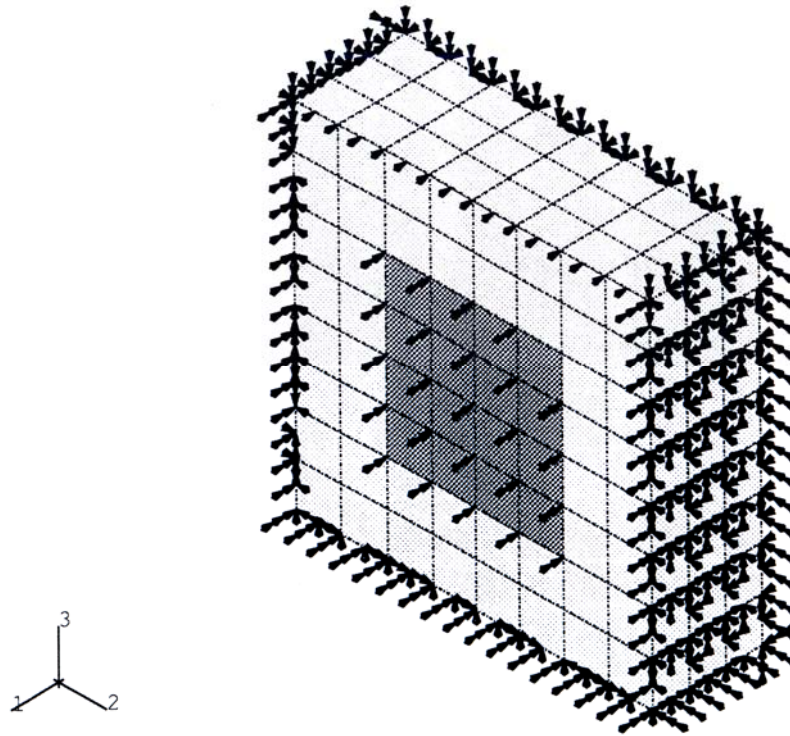


Figure 3.31 Supports

The quasi infinite wall was modelled applying these supports. The load was 10 N/mm^2 vertically distributed load (pressure) on the top surface. The applied FEM elements were: 20-node three-dimensional brick elements for masonry (C3D20), 4-node shell elements for steel plates (S4R5), 2-node three-dimensional bar elements for steel bars (B31) and INTER4 contact elements between the steel plates and masonry.

The CONCRETE material model, which was defined above, was applied for masonry. Steel plates had perfectly elastic behaviour and high stiffness ($E_s = 1.000.000 \text{ MPa}$). At the steel bars linear elastic – perfectly plastic material behaviour was applied.

3.3.3. Computed results

The computed results both of reinforced and unreinforced models are on the following.

The results of the case of 300 mm wall thickness are in Figure 3.32. The lowest curve shows the unreinforced case. The other curves are the results of reinforced models with different plate sides. As it was expected, when the plate side is increasing, the ultimate stress and the energy absorption capacity with relation to strain are increasing, too. Numerical results are in Table 3.3, where: d_{plate} – side length of the plates; σ_{max} – the

ultimate stress; ε_m – the strain at σ_{max} stress; dF/F_0 - percental increment of strength; A_{plate} – the confining plate's area; A_{wall} – the front surface of the wall; A_{plate}/A_{wall} – covering ratio; D_{plate} – distance between the plates' side; T_{wall} - wall thickness.

Table 3.3 The results of walls with 300 mm thickness

model	d_{plate} (mm)	σ_{max} (MPa)	ε_m ($\times 10^{-3}$)	dF/F_0 (%)	A_{plate}/A_{wall}	D_{plate}/T_{wall}
new 200nx	-	4.49	4.93	-	-	-
new 200n	200	4.73	7.35	5.35	0.0625	2
new 400n	400	5.17	9.65	15.14	0.25	1.333
new 600n	600	5.57	14.00	24.05	0.5625	0.667

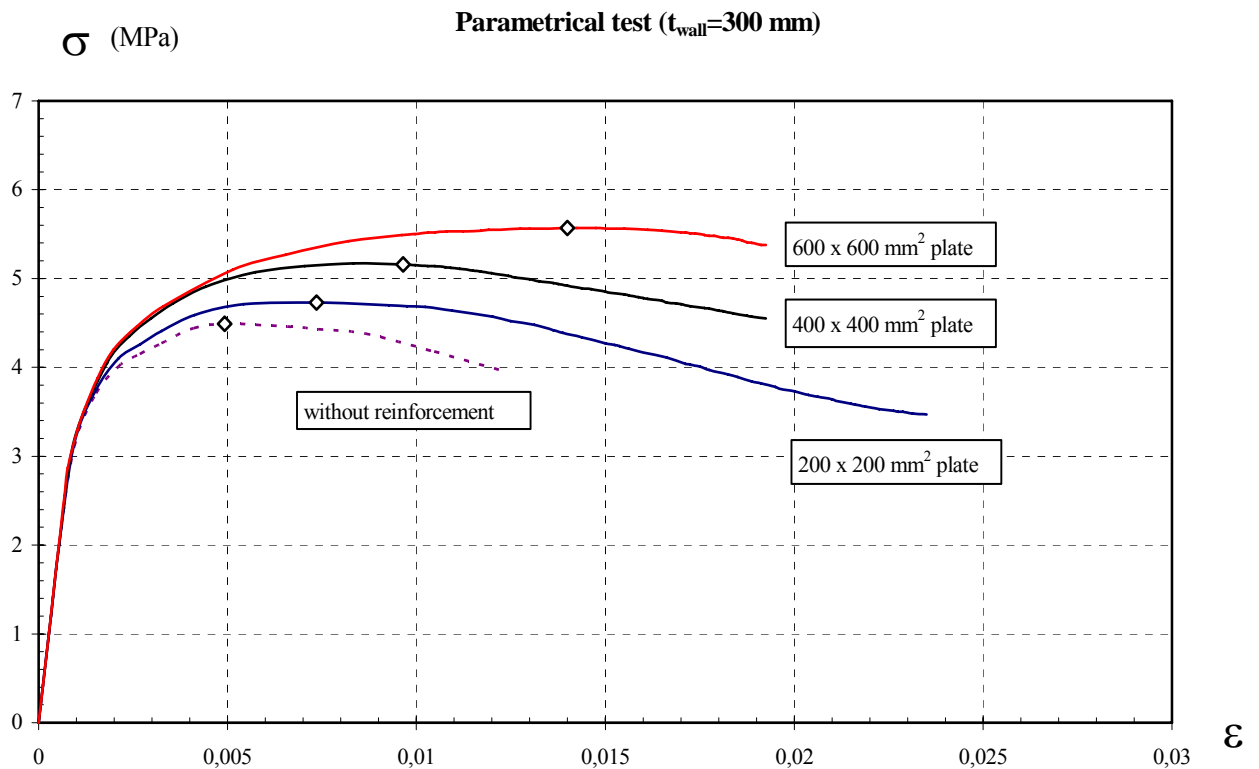


Figure 3.32 The results in case of 300 mm wall thickness

The previous parameters could be applied in case of 500 mm wall thickness, too. The summarised graphical results are in Figure 3.33. There are bigger differences between the computed results than at the previous cases with 300 mm wall thickness. Numerical results are in Table 3.4, where: d_{plate} – side length of the plates; σ_{max} – the ultimate stress; ε_m – the

strain at σ_{\max} stress; dF/F_0 - percental increment of strength; A_{plate} – the confining plate's area; A_{wall} – the front surface of the wall; $A_{\text{plate}}/A_{\text{wall}}$ – covering ratio; D_{plate} – distance between the plates' side; T_{wall} - wall thickness.

Table 3.4 The results of walls with 500 mm thickness

model	d_{plate} (mm)	σ_{\max} (MPa)	ε_m ($\times 10^{-3}$)	dF/F_0 (%)	$A_{\text{plate}}/A_{\text{wall}}$	$D_{\text{plate}}/T_{\text{wall}}$
new 605nx	-	4.48	4.43	-	-	-
new 205n	200	4.96	6.88	10.71	0.0625	1.2
new 405n	400	5.57	8.43	24.33	0.25	0.8
new 605n	600	6.14	12.41	37.05	0.5625	0.4

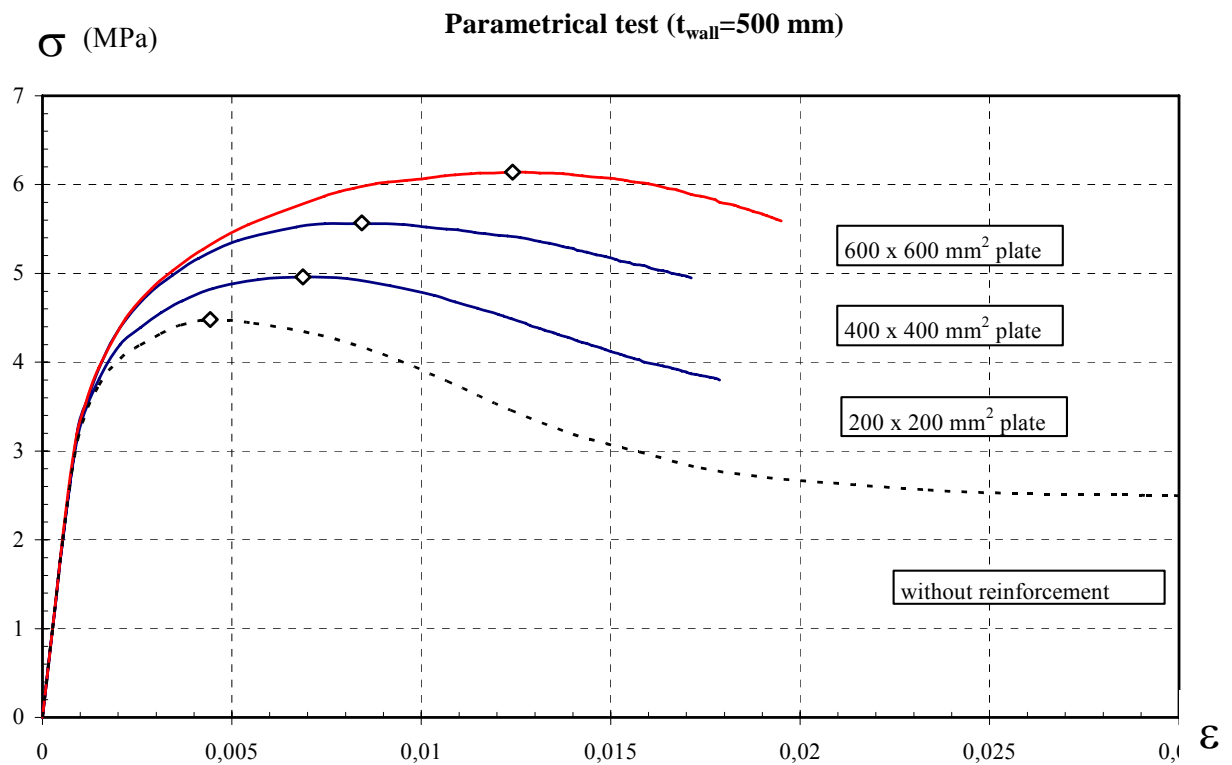


Figure 3.33 The results in case of 500 mm wall thickness

The summarised graphical results of Table 3.3 and Table 3.4 are in Figure 3.34. On the basis of Figure 3.34 and the Tables it could be determinate, when the same reinforcing plate is applied at both of walls, the effectiveness of the reinforcement, which is shown by the increment of strength, is bigger at the thicker wall.

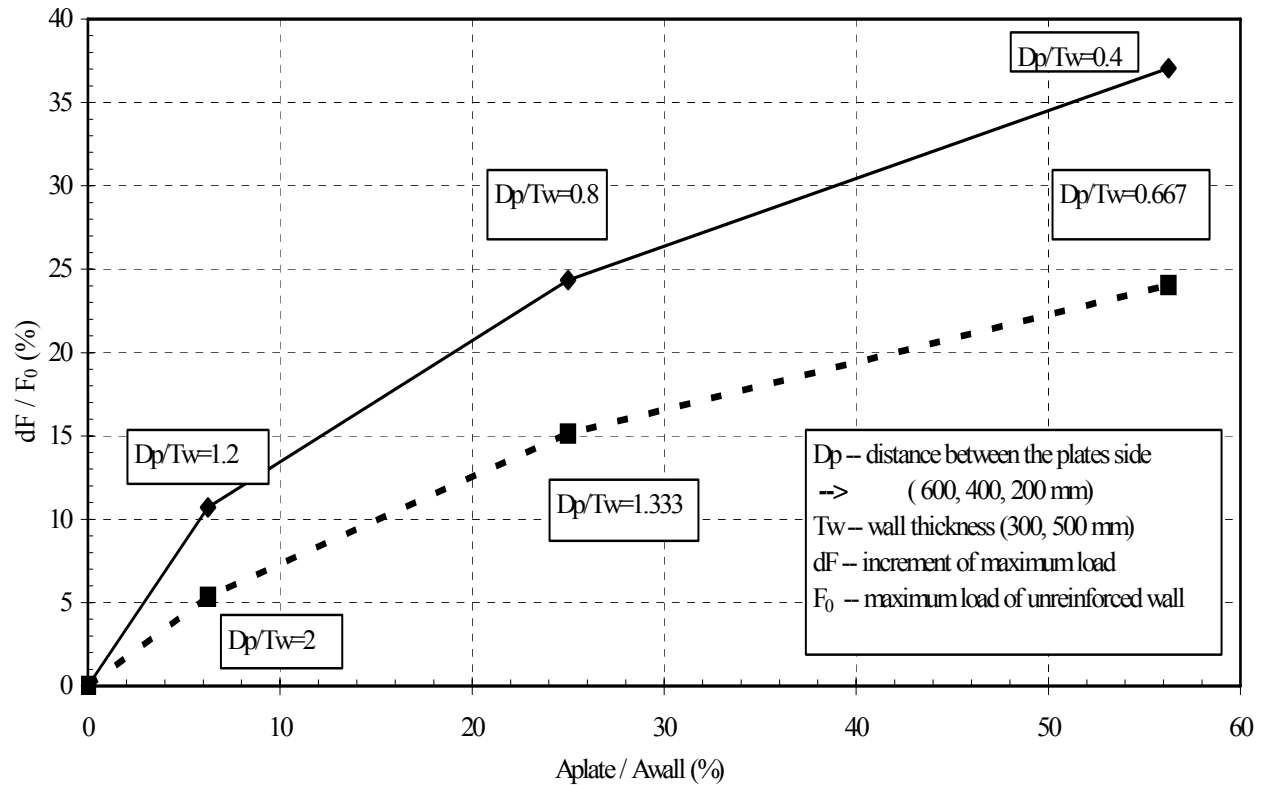


Figure 3.34 Comparison of two walls with different wall thickness

In case of nearly the same value of D_{plate}/T_{wall} ratios the possible increments of strength are nearly the same at both of walls. This fact demonstrates one of the findings of *G. Ballio* and *G.M. Calvi*, that the ratio between the plate distance and wall thickness is a fundamental parameter during the design process of reinforcing. *Ballio* and *Calvi* recommended this ratio being between 0.5 and 1. In that case the shear – tensile failure mode could be avoided.

	$T_{wall}= 300$ mm	$T_{wall}= 500$ mm
D_{plate}/ T_{wall}	0.667	0.8
dF/F_0 (%)	24.05	24.33
D_{plate}/ T_{wall}	1.333	1.2
dF/F_0 (%)	15.14	10.71

Some graphical results of *new400n* model from ABAQUS are in Figures 3.35 – 3.38. The confining effect of reinforcing steel plate could be seen well.

Other computer tests are required to determinate the designing directives mentioned at the beginning of this chapter. In the framework of these tests new models must be examined with different set-ups (e.g.: two, four and nine plates, new bars' diameter and plates' side length, etc.).

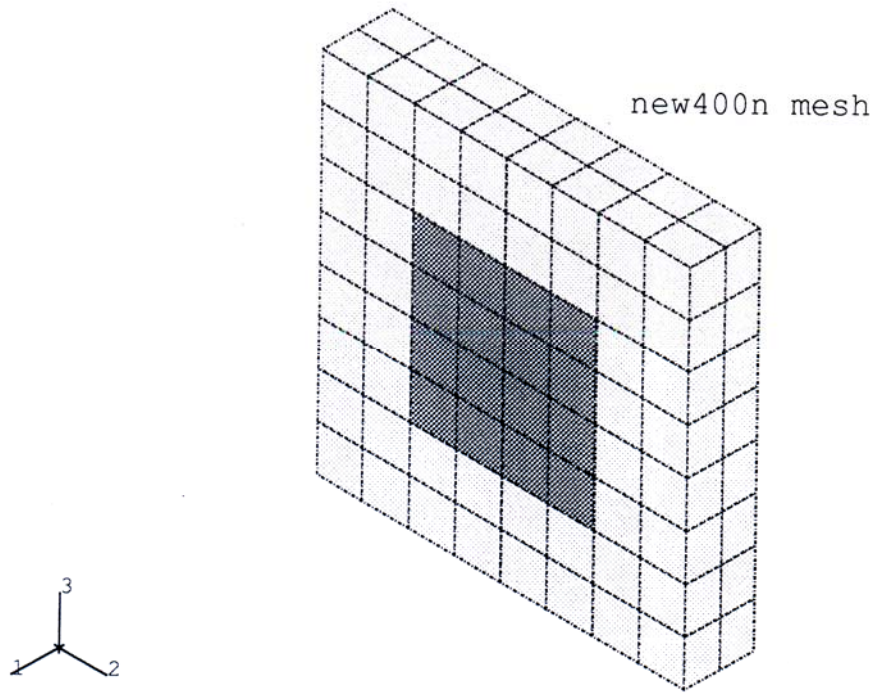


Figure 3.35 Finite element mesh

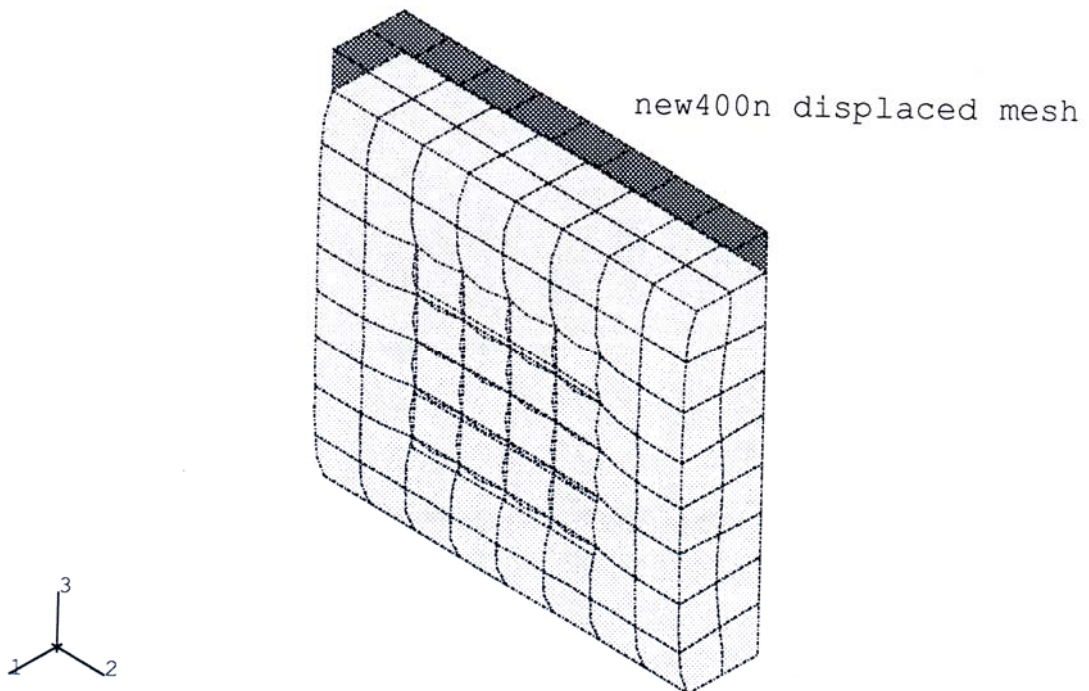


Figure 3.36 Deformed mesh

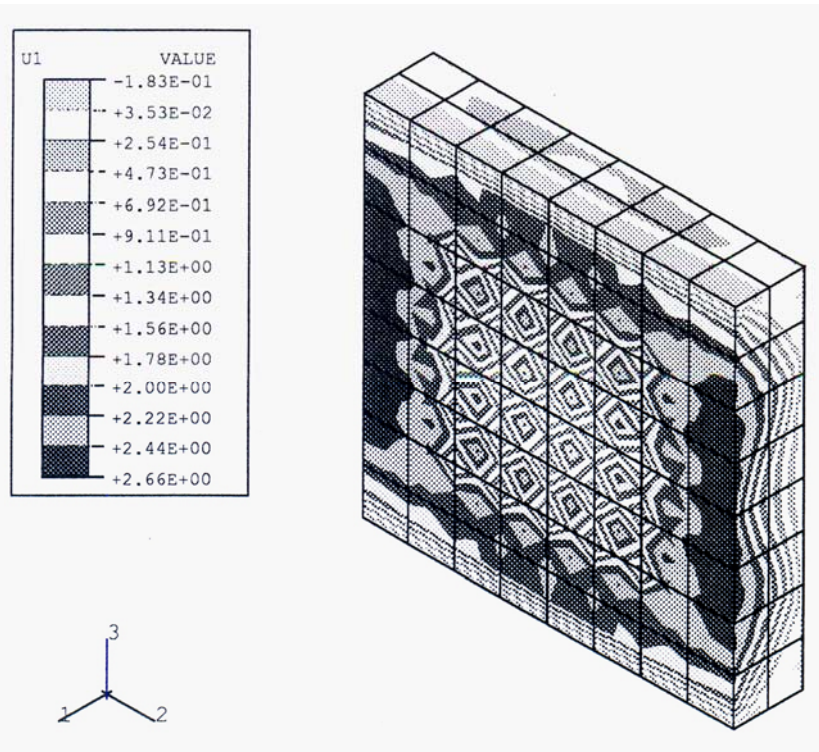


Figure 3.37 u_1 displacement distribution of masonry

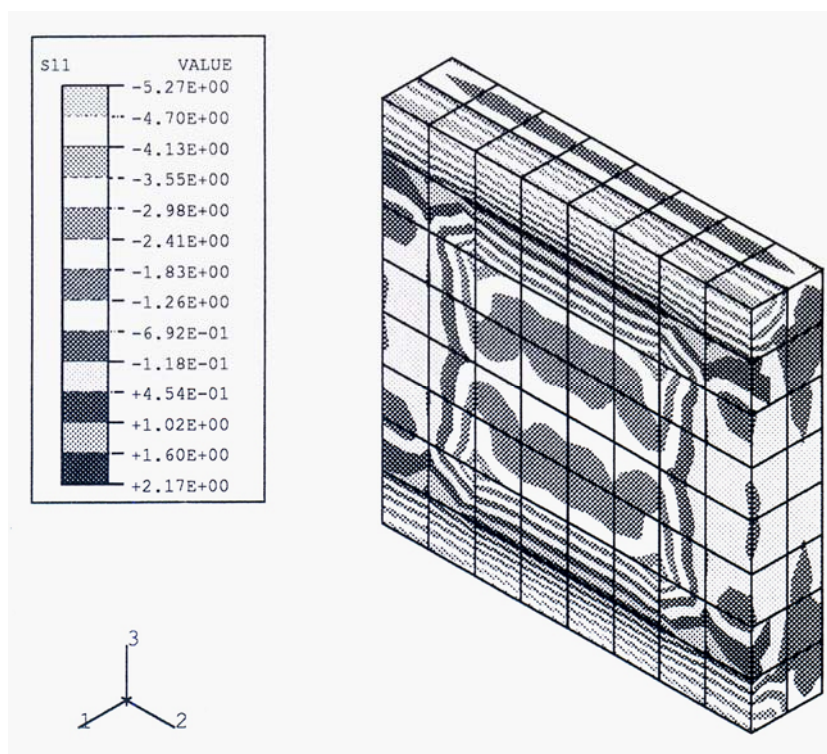


Figure 3.38 σ_{11} stresses' distribution of masonry

3.3.4. Some conclusions about the reinforcing by lateral confinement

The experimental results suggest that a shear-tensile failure is not likely to take place if the distance between plates edge is smaller than the thickness of the wall. This result may be significantly influenced by scale effects and texture of the outer skin of the wall; it has therefore to be applied with caution. For large scale structure and good masonry brickwork skin it is felt that it may result in very conservative solutions.

It has to be recommended to avoid the shear-tensile failure mode, because of the unreliable prediction of the improved behaviour after strengthening.

The punching of masonry failure mode partially compensates a less dependable behaviour up to the maximum stress with slower strength deterioration.

It can be concluded that it is important to limit the distance between plates' edge, while the ratio between plates' and bars' area can be maintained around the separator value ($A_p/A_b \approx 100$).

The experimental investigation has shown that for the given materials increments of 20% in strength and of 500% in deformation capacity can be assumed if proper details are used.

The most important effect of this strengthening technique is allowing stress redistribution without local collapse. At this method the properties of steel bars are fully exploited, either in terms of strength or in terms of energy absorption capacity.

New results of this chapter: Refurbishment of ancient masonry structures

a) numerical simulation of the lateral confinement

I investigated some numerical model for the lateral confinement reinforcing technique of ancient masonry walls. Allowing for the symmetry of both geometry of the model and loading action, only the eighth of the entire masonry has been considered for the computer analysis. The main geometrical and material parameters, such dimensions of masonry wall, numbers of reinforcing bars, material behaviour of the masonry, etc. came from the performed experiment series.

Corresponding to the above mentioned parameters, the calculated behaviour was that as was in the experiments.

b) parametrical analysis series applying lateral confinement

Parametrical analysis series were performed applying the lateral confinement reinforcing procedure. I get designing directives to determinate the effect of the reinforcing by computer simulation without experiments.

During the parametrical analysis series I applied different wall thicknesses, plate sizes and thicknesses, and gave design role for the effectiveness of lateral confinement.

In case of nearly the same value of D_{plate}/T_{wall} ratios the possible increments of strength are nearly the same at both of walls. This fact demonstrates that the ratio between the plate distance and wall thickness is a fundamental parameter during the design process of reinforcing

REFERENCES III.

- [26] Ballio, G., (1993), *Structural preservation of the Fraccaro tower in Pavia*, Structural Engineering International of IABSE, Vol. 3, N.1, p. 9-11.
- [27] Ballio, G., Calvi, G. M. and Duico, L. (1992), *Rinforzo di pareti murarie per mezzo di confinamento laterale*, Report No. 46 (in Italian), (Dipartimento di Meccanica Strutturale dell'Università di Pavia, Pavia)
- [28] Binda, L., Gatti, G., Mangano, G., Poggi, C. and Sacchi Landriani, G., (1992), *The collapse of the Civic Tower of Pavia: survey of the material and structure*, Masonry International, Vol. 6, N.1, p. 11-20.
- [29] Calvi, G.M. and Fanelli, M. (1990), *Investigations of the collapse of a medieval masonry tower*, The TMS Journal, Vol. 9, p. 51-59.
- [30] Hibbit, Karlsson & Sorensen, INC. (1995), *ABAQUS/Standard User's Manual and Theory Manual*, Version 5.5 and 5.6
- [31] Kotormán, I., (1996), *Comparison of different strengthening methods on masonry structures*, Refurbishment of structures, TEMPUS SJEP 09524-95 Workshop: Use of Steel in Refurbishment as a Friendly Activity, p. 69-78.
- [32] Macchi, G., (1993), *Monitoring Medieval Structures in Pavia*, Structural Engineering International of IABSE, Vol. 3, N.1, p. 6-9.
- [33] Mazzolani, F.M., (1996), *The use of steel in refurbishment*, Refurbishment of structures, TEMPUS SJEP 09524-95 Workshop: Use of Steel in Refurbishment as a Friendly Activity, p. 3-12.

- [34] Mazzolani, F.M., (1996), *Strengthening options in rehabilitation by means of steelworks*, Refurbishment of structures, TEMPUS SJEP 09524-95 Workshop: Use of Steel in Refurbishment as a Friendly Activity, p. 13-25.
- [35] Fülöp A. *Strengthening of masonry structures by lateral confinement* In: Iványi M., Hegedűs L., editors, Refurbishment of Structures, Report, TEMPUS S_JEP 09524-95 Use of Steel in Refurbishment, as an Environmentally Friendly Activity, Budapesti Műszaki Egyetem, Acélszerkezetek Tanszéke, 1997, pp. 83-96.
- [36] Ballio, G. and Calvi, G. M. (1993), *Strengthening of masonry structures by lateral confinement*, IABSE reports Vol. 70, p. 511-518. <http://dx.doi.org/10.5169/seals-53340>
- [37] Ferretti D. and Bažant Z.P. *Stability of ancient masonry towers: Moisture diffusion, carbonation and size effect*. International Journal of Cement and Concrete Research, Elsevier Science Ltd, 2006, Vol 36, p. 1379-1388.
- [38] Binda L., Tongini Folli R. and Roberti G.M. *Survey and investigation for the diagnosis of damaged masonry structures: The "Torrazzo" of Cremona* Proceedings of 12th International brick/block masonry conference, Madrid, Spain, 25-28 June 2000 pp. 10